UNIVERSIDADE FEDERAL DA BAHIA
Curso de Pós-graduação em Geofísica

TESE DE DOUTORADO

IMAGEAMENTO SÍSMICO: APLICAÇÃO EFICIENTE DA RTM CAUSAL, FLSRTM COM ALGORITMOS SVD ESTOCÁSTICOS E WEM BASEADO NA APROXIMAÇÃO DE JACOBI-ANGER

DANIEL REVELO APRAEZ

SALVADOR – BAHIA
OUTUBRO – 2024

Documento preparado com o sistema LaTeX.

Documento elaborado com os recursos gráficos e de informática do CPGG/UFBA

Imageamento sísmico: aplicação eficiente da RTM causal, FLSRTM com algoritmos SVD estocásticos e WEM baseado na aproximação de Jacobi-Anger

por
DANIEL REVELO APRAEZ
Físico (Universidad de Nariño, 2013)
Mestre em Geofísica (Universidade Federal da Bahia, 2015)

Orientador: Prof. Dr. Reynam da Cruz Pestana

TESE DE DOUTORADO
Submetida em satisfação parcial dos requisitos ao grau de
DOUTOR EM CIÊNCIAS
EM
GEOFÍSICA
ao
Conselho Acadêmico de Ensino
da
Universidade Federal da Bahia

Comissão Examinadora

Dr. Michelângelo Gomes da Silva (UFBA)

Edvaldo Suzarthe De Araujo
Dr. Edvaldo Suzarthe de Araújo (UFBA)

Dr. Jessé Costa (UFPA)

Documento assinado digitalmente
gov.br
JESSE CARVALHO COSTA
Data: 07/10/2024 07:24:05-0300
Verifique em https://validar.iti.gov.br

Jonathas da Silva Maciel
Dr. Jonatas Maciel (SENAI/CIMATEC)

Dr. Reynam da Cruz Pestana - Orientador (UFBA)

Aprovada em 03 de Outubro de 2024

A presente pesquisa foi desenvolvida no Centro de Pesquisa em Geofísica e Geologia da UFBA, com recursos próprios, da CAPES, e do CNPq.

A654 Apraez, Daniel Revelo
Imageamento sísmico: aplicação eficiente da RTM causal, FLSRTM com algoritmos SVD estocásticos e WEM baseado na aproximação de Jacobi-Anger / Daniel Revelo Apraez – Salvador, 2024.
140 f.: il

Orientador: Prof. Dr. Reynam da Cruz Pestana

Tese (Doutorado – Pós-graduação em Geofísica) – Universidade Federal da Bahia. Instituto de Geociências, 2024.

1. Geofísica. 2. Imageamento sísmico. 3. Campo de ondas acústico. I. Pestana, Reynam da Cruz. II. Universidade Federal da Bahia. III. Título.

CDU:550.34.01

Este trabalho é dedicado aos meus pais,
Gladys Apraez e David Revelo, pela
compreensão e apoio incondicional.

Resumo

Esta tese aborda o desenvolvimento de técnicas relacionadas à migração sísmica, com o objetivo de superar limitações e desafios presentes em metodologias tradicionais. Nos três capítulos que compõem este trabalho, são apresentadas soluções que aprimoram a eficiência computacional, a precisão na formação de imagens sísmicas e a capacidade de lidar com modelos complexos de subsuperfície. No capítulo 1, abordamos a separação do campo de ondas em componentes ascendentes e descendentes, uma etapa crucial no processamento de dados multicomponente, na propagação de campos de ondas e no imageamento sísmico. Propomos um método alternativo para calcular o campo de ondas analítico utilizando a equação parcial de primeira ordem no tempo e resolvendo a equação de onda uma única vez. Essa abordagem permite a separação dos campos de ondas de forma explícita a cada passo de tempo, sendo mais eficiente em termos computacionais e viabilizando a aplicação da condição de imagem causal na migração reversa no tempo (RTM). Resultados em modelos sintéticos mostram que o método proposto possibilita uma decomposição semelhante à obtida pelo método convencional, que requer duas propagações, com potencial aplicação em casos 3D. Além disso, o método é eficaz na remoção do ruído de baixa frequência presente nas imagens RTM que utilizam a condição de imagem por correlação cruzada. No capítulo 2, investigamos a migração reversa no tempo em mínimos quadrados no domínio da frequência (FLSRTM), que é capaz de produzir modelos de refletividade de alta resolução. No entanto, o armazenamento das funções de Green necessárias para o cálculo do gradiente e do campo espalhado via modelagem Born pode ser inviável devido ao tamanho dessas funções. Propomos um esquema FLSRTM utilizando funções de Green de baixo posto, obtidas por meio de algoritmos de decomposição de valores singulares randômico (rSVD) e comprimido (cSVD). Esses algoritmos permitem o armazenamento eficiente das funções de Green em memória, utilizando pouco espaço e reduzindo o tempo computacional. Avaliações realizadas em modelos sintéticos demonstram que o esquema proposto gera seções migradas idênticas com aquelas geradas pelo esquema FLSRTM usando as funções de Green originais, utilizando menos memória e tempo computacional. No capítulo 3, abordamos as limitações dos operadores convencionais de migração em profundidade por continuação descendente do campo de ondas, tais como a geração indesejada de ondas evanescentes, o imageamento em meios com fortes contrastes de velocidade e refletores com mergulhos acentuados, além da estabilidade do propagador unidirecional. Propomos um algoritmo de migração em profundidade baseado em uma equação de onda unidirecional que é, ao mesmo tempo, estável e eficiente. Para isso, utilizamos o projetor espectral para suprimir modos evanescentes do operador de Helmholtz e aplicamos o esquema iterativo de Schulz acoplado para calcular a raiz quadrada desse operador filtrado. Finalmente, introduzimos a expansão de Jacobi-Anger para aproximar o operador exponencial de matriz, permitindo a construção do propagador de forma estável. Testes de resposta ao impulso, assim como a aplicação em dados de campo, demonstram que nosso algoritmo é mais preciso e eficaz para imagens em meios com fortes variações laterais de velocidade, superando a qualidade das imagens obtidas por métodos tradicionais.

Abstract

This thesis addresses the development of techniques related to seismic migration, aiming overcome the limitations and challenges present in traditional methodologies. The three chapters of this work present solutions that enhance computational efficiency, accuracy in seismic imaging, and the ability to handle complex subsurface models. In chapter 1, we focus on the separation of the wavefield into upgoing and downgoing components, a crucial step in the processing of multicomponent data, wavefield propagation, and seismic imaging. We propose an alternative method for computing the analytical wavefield using the first-order partial equation in time, solving the wave equation only once. This approach allows for the explicit separation of wavefields at each time step, making it more computationally efficient and enabling the application of the causal imaging condition in reverse time migration (RTM). Results from synthetic models indicate that the proposed method achieves a decomposition similar to that obtained by the conventional method, which requires two propagations, with potential applications in 3D cases. Moreover, the method effectively removes low-frequency noise present in RTM images that use the cross-correlation imaging condition. In chapter 2, we investigate frequency-domain least-squares RTM (FLSRTM), which is capable of producing high-resolution reflectivity models. However, storing the Green's functions needed for gradient computation and the scattered wavefield via Born modeling may be unfeasible due to their size. We propose a FLSRTM scheme using low-rank Green's functions obtained through randomized (rSVD) and compressed (cSVD) singular value decomposition algorithms. These algorithms allow for efficient storage of Green's functions in memory, using less space and reducing computational time. Evaluations on synthetic models demonstrate that the proposed scheme generates migrated sections identical to those produced by the FLSRTM scheme using the original Green's functions while utilizing less memory and computational time. In chapter 3, we address the limitations of conventional depth migration operators based on downward continuation of the acoustic wavefield, such as the undesired generation of evanescent waves, imaging in media with strong velocity contrasts and steeply dipping reflectors, and the stability of the one-way propagator. We propose a depth migration algorithm based on an one-way wave equation that is both stable and efficient. To achieve this, we use a spectral projector to suppress evanescent modes from the Helmholtz operator and apply the coupled Schulz iterative scheme to compute the square root of this filtered operator. Finally, we introduce the Jacobi-Anger expansion to approximate the exponential matrix operator, enabling the stable construction of the propagator. Impulse response tests, as well as field data applications, demonstrate that our algorithm is more accurate and effective for imaging in media with strong lateral velocity variations, surpassing the quality of images obtained by conventional methods.

Índice

Índice de figuras

Memorial descritivo

O problema

RTM utilizando uma construção eficiente do campo de ondas analítico

A migração reversa no tempo (do inglês "*Reverse-Time Migration*" - RTM) (Whitmore, 1983; Baysal et al., 1983; McMechan, 1983) tem se tornado um dos métodos de imageamento sísmico mais empregados na indústria de exploração sísmica, isso devido a sua capacidade de gerar imagens da subsuperfície com estruturas arbitrariamente complexas e com mergulho acentuado na subsuperfície, permitindo obter resultados de alta resolução. Na RTM convencional, para dados não empilhados e organizados em família de fonte comum, a imagem é construída tomando a correlação cruzada dos campos de ondas da fonte e do receptor propagados no sentido direto e reverso no tempo, respectivamente. A seção migrada resultante é sempre contaminada por ruído de baixa frequência espacial e alta amplitude, além de falsos refletores, os quais resultam da correlação cruzada dos diferentes tipos de ondas (p. ex., refratadas, mergulhantes, e retroespalhadas) geradas devido aos fortes gradientes ou interfaces acentuadas no modelo de velocidade empregado na migração. Nos últimos anos, mais atenção tem sido dada para melhorar a condição de imagem e, portanto, reduzir os efeitos que contaminam o modelo de refletividade obtido pela técnica RTM. Fei et al. (2015) fizeram uma revisão comparativa dos métodos propostos na literatura para o caso acústico, e os agruparam em três categorias: antes, depois ou durante a aplicação da condição de imagem.

Fletcher et al. (2006) sugeriram um procedimento para remover as reflexões indesejáveis durante a propagação do campo de ondas. Neste procedimento, a ideia principal é aplicar um termo de amortecimento direcional à equação de onda em áreas do modelo de velocidade onde ocorrem as reflexões indesejadas, derivando desta forma a equação de onda não-reflexiva. O uso dessa abordagem torna-se inconveniente quando é aplicada em um modelo com interfaces muito complicadas, isso devido à necessidade do conhecimento adicional da direção na qual a energia está se propagando. Usando uma ideia similar, Yoon e Marfurt (2006) usaram o fato de que eventos de reflexão (ângulos de abertura curtos) e artefatos (afastamento fonte-receptor distante) possuem diferentes faixas de ângulo de abertura, portanto as direções de propagação de onda podem ser usadas para eliminar artefatos na seção migrada. Desta forma, antes de aplicar a condição de imagem, o ângulo entre as ondas incidente e refletida é limitado através do cálculo do vetor de Poynting. O método proposto por Yoon e Marfurt (2006) funciona bem para modelos simples, mas requer um custo de armazenamento adicional e não produz resultados satisfatórios em subsuperfícies complexas (Guitton et al., 2007). Uma abordagem prática na qual os artefatos são filtrados após a geração da imagem migrada é o filtro Laplaciano (Youn e Zhou, 2001; Zhang e Sun, 2009), que é fácil de aplicar e mostra boa atenuação do ruído de baixa frequência espacial, mas pode filtrar também o sinal de interesse (Guitton et al., 2007).

Outra forma de mitigar o problema dos artefatos presentes na imagem RTM é modificando a condição de imagem. Nesse sentido, Brandsberg-Dahl et al. (2013) e Rocha et al. (2016) apresentaram um esquema de imageamento baseado na teoria do espalhamento inverso generalizado (Stolk et al., 2009). Nessa abordagem, os artefatos causados pela energia retroespalhada são atenuados usando a combinação de duas condições de imagem separadas: *i)* o produto das derivadas temporais dos campos de ondas da fonte e do receptor, e *ii)* o produto dos gradientes espaciais dos campos de ondas da fonte e do receptor. Então, uma soma ponderada dessas imagens é calculada para gerar a seção migrada final. Como uma aplicação da condição de imagem de espalhamento inverso, Pestana et al. (2014) propuseram um esquema onde o componente descendente do campo de onda da fonte - obtido pela aplicação do vetor de Poynting - é usado na aplicação do mencionado processo de imageamento. Mais recentemente, com base no conceito da norma energética, Rocha et al. (2016) desenvolveram uma condição de imagem flexível que não apenas atenua os artefatos na RTM, mas também atenua qualquer ângulo de reflexão selecionado. A condição da norma energética, proposta tanto para o caso acústico, como para meios com anisotropia, além de ser similar à condição de imagem de espalhamento inverso, também está relacionada ao filtro Laplaciano, conforme demonstrado em Rocha et al. (2016). Em geral, as condições de imagem baseadas na teoria introduzida por Stolk et al. (2009), produzem imagens de qualidade muito superior quando comparadas com aquelas obtidas mediante a correlação convencional.

Liu et al. (2011) propuseram uma condição de imagem baseada na decomposição do campo de ondas em componentes unidirecionais, a qual também pertence ao grupo de métodos que modificam a correlação cruzada padrão na RTM. Nessa condição de imagem, é permitida apenas a correlação dos componentes do campo de ondas que se propagam em direções opostas. O método proposto por Liu et al. (2011) é uma técnica de separação implícita, que pode remover com sucesso muitos tipos de artefatos, enquanto preserva a amplitude da imagem, sem a necessidade de aplicar um filtro Laplaciano após a condição de imagem. No entanto, uma decomposição incompleta do campo de ondas pode dar origem a artefatos na seção migrada, como mostrado por Fei et al. (2014), Shen e Albertin (2015) e Wang et al. (2016b). Desta maneira, dado que a abordagem proposta por Liu et al. (2011) baseia-se numa separação implícita, os campos de ondas ascendentes e descendentes não estão disponíveis e suas aplicações são limitadas. A fim de obter os componentes unidirecionais, o campo de ondas é geralmente levado ao domínio de Fourier ($\omega - k$), e então define-se a direção de propagação levando em conta o sinal da frequência e do número de onda (Hu e McMechan, 1987; Liu et al., 2011). Dessa forma, observa-se que o método convencional de decomposição do campo de ondas no domínio do tempo precisa armazenar o campo de ondas e realizar uma transformada de Fourier ao longo do eixo do tempo. Esse processo aumenta o custo de entrada/saída (I/O), dado que o eixo temporal corresponde à dimensão com maior número de amostras do campo de ondas armazenado, e a transformada de Fourier opera de maneira mais eficiente nos dados que são armazenados contiguamente.

Por outro lado, se podemos definir um campo de ondas no domínio do tempo cujo espectro seja apenas positivo ou negativo (Shen e Albertin, 2015; Wang et al., 2016a; Wang et al., 2017), a direção da propagação do campo de pressão estará apenas determinada pelo sinal do número de onda espacial, e então, o alto custo de I/O será evitado. Este sinal é o sinal analítico que é amplamente utilizado no processamento de sinais. O sinal analítico é um sinal complexo cuja parte real é o próprio sinal e sua parte complexa é a transformada de Hilbert da parte real. Para a técnica RTM, o conceito do sinal analítico é estendido e então chamado de campo de ondas analítico (Zhang et al., 2007; Sun et al., 2016). Como o campo de ondas analítico contém apenas frequências positivas, os componentes de onda ascendente e descendente podem ser convenientemente obtidos pela aplicação de um filtro de Fourier 1D ao longo da direção da profundidade. Comparado com o método de Liu et al. (2011) da construção de imagens RTM, uma grande vantagem do uso do campo de ondas analítico é que os componentes ascendente e descendente do campo de pressão são completamente separados e estão disponíveis de forma explícita para diferentes aplicações, além de eliminar o requisito de armazenamento computacional, bem como a necessidade de transformadas rápidas de Fourier (do inglês "*Fast Fourier Transform*" - FFT) no eixo do tempo. Recentemente, Costa et al. (2018) apresentaram uma condição de imagem baseada na coerência da fase entre os campos de ondas propagados, a qual emprega os atributos instantâneos do campo de ondas analítico (envelope e a fase instantânea). Segundo os resultados de Costa et al. (2018), a condição de imagem aplicada pode ajudar a delinear características estratigráficas e estruturais que são mais difíceis de se ver em imagens convencionais, apresentando dessa forma outra importante aplicação do campo de ondas analítico.

Nos últimos anos, vários trabalhos sobre a decomposição do campo de ondas usando o campo de ondas analítico foram apresentados. Para tal fim, na simulação da evolução temporal do campo de pressão e avaliação do operador Laplaciano, o método convencional de diferenças finitas foi adotado por Shen e Albertin (2015), Wang et al. (2016b), Wang et al. (2016a), Zheng et al. (2018) e Costa et al. (2018). Como descrito no trabalho de Shen e Albertin (2015), a parte imaginária do campo de ondas analítico é construída através da solução da equação da onda tendo como termo fonte a transformada de Hilbert do próprio termo fonte. O par de campos de ondas - aquele propagado com o termo fonte e o outro gerado pela sua transformada de Hilbert - constituem o campo de ondas analítico. Com base na construção do campo de ondas analítico, os componentes unidirecionais podem ser encontrados de forma explícita, então Shen e Albertin (2015) propuseram uma condição de imagem, denominada imagem causal, que correlaciona os componentes descendente e ascendente da fonte e do receptor, respectivamente. Este método foi testado e provou ser bem-sucedido na remoção de muitos tipos de artefatos, os quais são comuns nas seções resultantes da aplicação da condição de imagem de correlação cruzada proposta por Claerbout (1971).

Métodos para simular a propagação do campo de ondas analítico, que apenas precisam do estado presente para extrapolar o campo ao passo seguinte no tempo, têm sido desenvolvidos a fim de evitar a dispersão numérica, problema gerado no esquema de diferenças finitas quando o intervalo de discretização espacial ou temporal é grande; Du et al. (2014) revisaram esses métodos e os denominaram métodos de extrapolação integral recursiva no tempo (do inglês "*Recursive Integral Time-Extrapolation Methods*" - RITE). Em Revelo et al. (2016) e Wang e Liu (2017), a implementação de dois diferentes esquemas de extrapolação do campo de ondas analítico é apresentada, bem como a sua aplicação na construção dos componentes unidirecionais do campo de ondas; para a técnica RTM, os campos de ondas da fonte e do receptor são extrapolados no tempo, seguido da etapa da separação em forma explícita nos seus componentes ascendente e descendente, isto para cada intervalo de tempo e aplicando o esquema de separação proposto por Shen e Albertin (2015). A distinção clara entre o método de Revelo et al. (2016) e o proposto por Shen e Albertin (2015) é que no primeiro usa-se uma solução de equação de onda de primeira ordem com um termo fonte analítico, enquanto em Shen e Albertin (2015) foi necessário resolver a equação de onda duas vezes: uma vez para a fonte e outra para a transformada de Hilbert do próprio termo fonte. Em relação ao trabalho de Liu et al. (2011), a principal diferença é que o método proposto por Shen e Albertin (2015) pode fornecer uma separação explícita do campo de ondas, enquanto o esquema de Liu et al. (2011) resulta em uma separação implícita.

Levando em conta o desafio computacional que pode apresentar a construção do campo de ondas analítico, na primeira parte de esta tese, é proposto um esquema que tem como base o método de expansão rápida (do inglês "*Rapid Expansion Method*" - REM) (Tal-Ezer et al., 1987; Pestana e Stoffa, 2010), no qual o campo de ondas analítico é calculado apenas resolvendo a equação de onda uma vez. O REM permite propagar ondas livres do efeito de dispersão numérica e é capaz de extrapolar o campo de pressão usando intervalos de tempo próximos ao limite de Nyquist. Com o REM também é possível obter a derivada de primeira ordem no tempo do campo de ondas ao mesmo tempo que o próprio campo é extrapolado e, assim, calcular a parte imaginária do campo de ondas analítico como proposto por Zhang e Zhang (2009). Depois disso, podemos separar o campo de ondas em seus componentes ascendentes e descendentes. Desta forma, no método proposto, a equação de onda é resolvida apenas uma vez, melhorando a eficiência computacional do procedimento de separação do campo de ondas seguido pela aplicação da condição de imagem causal para a RTM. Os bons resultados obtidos com a abordagem proposta, em termos de redução do tempo de execução, transformam a técnica em uma interessante alternativa, especialmente quando se trata com modelos de velocidades complexos e grandes volumes de dados.

LSRTM no domínio da frequência com uso eficiente de memória por meio de métodos SVD estocásticos

A geração de seções migradas é uma etapa crucial no processamento sísmico, responsável por construir imagens em profundidade do subsolo a partir de dados registrados no tempo. Ela corrige a profundidade e a inclinação dos refletores e suprime as difrações (Claerbout, 1992; Andrade et al., 2017). Entre as técnicas de migração sísmica, a RTM, que envolve a retropropagação dos dados de campo utilizando a equação da onda bidirecional (Ren et al., 2013), tem se mostrado a técnica de imageamento sísmico mais precisa. Isso se deve à sua capacidade de imagear estruturas arbitrariamente complexas e com mergulhos acentuados no subsolo, desde que um modelo de velocidade preciso esteja disponível. Com o aumento das demandas na exploração de óleo e gás, há uma necessidade crescente de que o imageamento sísmico forneça informações mais abrangentes além da simples estrutura do subsolo, como a refletividade. Apesar dos resultados satisfatórios obtidos pela RTM, o operador de migração sísmica possui uma relação adjunta com o operador de modelagem Born (Liu et al., 2022). Portanto, um aspecto importante que afeta a imagem da migração sísmica é a incapacidade do operador adjunto de aproximar com precisão o operador inverso (Claerbout, 1992; Symes, 2009). Consequentemente, a imagem resultante pode sofrer de efeitos de desfoque, com amplitudes incorretas e artefatos de migração em condições de aquisição imperfeitas, como fonte sísmica com largura de banda limitada, abertura de registro finita, geometria de amostragem irregular ou frequências ausentes (Nemeth et al., 1999; Etgen et al., 2009; Liu et al., 2022; Kim et al., 2022).

Para superar esse problema, Tarantola (1984) introduziu um método eficaz para melhorar a qualidade da imagem de migração e gerar um resultado de imageamento com preservação de amplitude. Essa abordagem, conhecida como migração por mínimos quadrados (do inglês "*Least Square Migration*" - LSM) (Bamberger et al., 1982), é um esquema de inversão linearizada baseado na minimização de uma função de mínimos quadrados. Ela aproxima o operador inverso minimizando iterativamente a função objetivo definida, utilizando um método de otimização baseado no gradiente (Nemeth et al., 1999; Dutta e Schuster, 2014). Em particular, quando o esquema LSM é aplicado utilizando a equação completa da onda, é denominado de migração reversa no tempo por mínimos quadrados (do inglês "*Least Square Reverese Time Migration*" - LSRTM) (Schuster, 1993; Nemeth et al., 1999; Dong et al., 2012; Yao et al., 2022). Esse método, baseado na aproximação de Born, tem mostrado ser mais eficiente na migração de estruturas geológicas complexas (Wong et al., 2012). O esquema LSRTM iterativo típico consiste em três componentes principais: um operador de modelagem para simular dados sísmicos, um operador de migração para calcular o gradiente e um esquema de inversão para minimizar a função objetivo. Considerando que o gradiente da função erro calculado no LSRTM no domínio do tempo (TLSRTM) deve ser computado de forma independente para cada sismograma do dado sísmico (Herrmann e Li, 2012; Dai et al., 2012; Zhang et al., 2015), o custo computacional do TLSRTM pode aumentar drasticamente proporcionalmente ao número de tiros. Avanços significativos foram alcançados recentemente visando melhorar a qualidade do imageamento sísmico, ao mesmo tempo em que se reduz o custo computacional do TLSRTM (Herrmann e Li, 2012; Dai e Schuster, 2013; Xue et al., 2016; Yao e Jakubowicz, 2016; Liu e Peter, 2018).

O esquema LSRTM no domínio da frequência (FLSRTM) pode ser empregado para reduzir o custo computacional na aplicação do LSRTM em dados sísmicos com um número considerável de tiros, oferecendo várias vantagens sobre a versão no domínio do tempo. Notavelmente, apenas alguns componentes de frequência válidos dos dados são necessários para gerar a seção migrada (Kim et al., 2022). Além disso, se as funções de Green puderem ser armazenadas na memória do computador, o gradiente e os dados modelados via operador de Born podem ser eficientemente calculados sem a necessidade de extrapolações adicionais do campo de ondas (Ren et al., 2013). Observamos que, no esquema FLSRTM, o campo de ondas espalhado e o gradiente da função de desajuste são expressos em função das funções de Green de fundo no domínio da frequência. Considerando que o FLSRTM representa uma inversão linearizada, e não atualiza o modelo de velocidade, todas as funções de Green de fundo, desde as fontes até os refletores e dos refletores até os receptores, que apenas dependem da velocidade de fundo, devem ser calculadas uma vez e armazenadas na memória do computador para cada frequência. Embora a FLSRTM tenha se mostrado eficiente, esse esquema pode ser severamente limitado pelos requisitos substanciais de armazenamento de memória para salvar as funções de Green de fundo, especialmente quando um grande conjunto de dados e modelo são usados (Liu et al., 2022). Para mitigar esse problema, Ren et al. (2013) implementaram uma versão do FLSRTM em que as funções de Green das fontes e dos receptores são armazenadas na memória durante a primeira iteração do esquema de inversão. Embora esse esquema seja limitado pela memória interna do computador, a eficiência do método é atraente. Como uma abordagem alternativa, Zhao e Sen (2019) propuseram a codificação de registros de disparo com ondas planas para reduzir os requisitos de armazenamento de memória para salvar as funções de Green.

Mais recentemente, Kim et al. (2022) introduziram uma versão rápida e eficiente em termos de memória da FLSRTM, na qual adotaram a decomposição em valores singulares (do inglês "*Singular Value Decomposition*" - SVD) para construir a representação de baixo posto das funções de Green e reduzir o armazenamento de memória necessário. Embora o esquema FLSRTM com funções de Green de baixo posto possa produzir resultados de migração tão precisos quanto o esquema FLSRTM convencional com menor uso de memória, a geração dessa representação de baixo posto via SVD pode ser computacionalmente intensiva, especialmente ao lidar com grandes conjuntos de dados ou modelos. Alternativamente, algoritmos iterativos, como aqueles baseados nos subespaços de Krylov, podem ser empregados para aproximar os vetores singulares dominantes de forma mais eficiente (Golub e Van Loan, 1996). Esses algoritmos representam as abordagens mais amplamente utilizadas para calcular aproximações de matrizes de baixo posto, especialmente para grandes matrizes esparsas. No entanto, nas últimas duas décadas, algoritmos estocásticos ganharam popularidade. Isso se deve ao fato de que algoritmos randomizados geralmente apresentam melhor desempenho na prática e são mais robustos em comparação com os métodos de Krylov (Martinsson, 2019). A ideia básica desses algoritmos é empregar certa quantidade de aleatoriedade para derivar uma matriz menor a partir da matriz original de alta dimensão, que captura a informação essencial e oferece uma alternativa confiável e computacionalmente eficiente para obter uma representação SVD de baixo posto (Sarlos, 2006; Gu, 2015; Erichson et al., 2019).

Nesta segunda parte da tese, propomos a implementação do esquema FLSRTM que utiliza funções de Green de baixo postos geradas via algoritmos SVD aleatório (do inglês "*randomized SVD*" - rSVD) (Halko et al., 2011; Martinsson et al., 2011; Halko, 2012; Tropp e Webber, 2023) e comprimido (do inglês "*compressed SVD*" - cSVD) (Erichson et al., 2017; Erichson et al., 2019) para melhorar o desempenho em tempo de execução. O algoritmo aprimorado aborda os desafios computacionais associados ao esquema FLSRTM convencional.

O ponto central da solução reside na proficiência dos algoritmos rSVD e cSVD em extrair eficientemente informações relevantes das funções de Green para construir suas representações de baixo posto. Diferente do algoritmo SVD convencional, as versões rSVD e cSVD começam gerando uma matriz comprimida a partir da matriz original, utilizando uma matriz aleatória Gaussiana e uma decomposição QR econômica. O tamanho da matriz comprimida é determinado pelo coeficiente de truncamento, que corresponde ao posto ótimo e é determinado utilizando um critério específico (Kim et al., 2022). Liu e Peter (2020) demonstraram que, se o critério de truncamento for ajustado corretamente, esses algoritmos podem comprimir significativamente a matriz original, levando a uma redução no uso de memória e no tempo de computação. Embora o algoritmo rSVD seja matematicamente robusto e ofereça limites de erro fortes, há potencial para inovações e melhorias, como as introduzidas no algoritmo cSVD apresentado por Ji e Li (2014). O algoritmo cSVD fornece um equilíbrio eficaz entre precisão e tempo de cômputo, sendo particularmente adequado para aproximar grandes matrizes. Consequentemente, suas vantagens computacionais tornam-se mais significativas à medida que as dimensões aumentam. Por meio de experimentos numéricos conduzidos em modelos sintéticos, comprovamos a eficácia do algoritmo proposto na geração de imagens sísmicas de alta qualidade. Além disso, por meio de uma análise comparativa dos resultados de migração e dos custos computacionais em exemplos numéricos, evidenciamos a eficiência do esquema FLSRTM proposto em termos de uso de memória e tempo de computação, utilizando a representação de baixo posto das funções de Green por meio de algoritmos SVD estocásticos.

Migração sísmica através da solução da equação de onda unidirecional baseada na expansão de Jacobi-Anger

A equação da onda unidirecional, derivada de uma solução aproximada da equação de onda completa, é de fundamental importância na extrapolação em profundidade do campo de ondas usado dentro do esquema da migração através da equação de onda (do inglês "*Wave-equation Migration*" - WEM) (Claerbout, 1971). Nesta abordagem, a equação de onda completa é decomposta ao longo da direção dominante de propagação, reduzindo a dimensionalidade computacional. Como resultado, o método WEM apresenta uma vantagem significativa em problemas de grande escala. Diferentemente da técnica RTM, o WEM oferece precisão de fases e amplitudes apenas dentro de ângulos de propagação limitados, especialmente em meios com fortes contrastes de velocidade e refletores com mergulhos acentuados. Embora a RTM seja amplamente estudada na indústria e na academia, ela apresenta desvantagens, como altos custos de memória e artefatos de baixa frequência, que podem ser atenuadas pelo algoritmo WEM. Os propagadores de ondas unidimensionais, utilizados em métodos de migração que se baseiam na separação da equação de onda completa, oferecem uma solução cinemática confiável para ondas acústicas. A fatoração da equação de onda em operadores ascendentes e descendentes introduz o operador de raiz quadrada (ou número de onda vertical), que é caracterizado por sua não-localidade.

Embora diversos métodos tenham sido desenvolvidos para aproximar o operador de raiz quadrada por um operador local, a precisão dessas aproximações ainda é limitada. Os algoritmos WEM convencionais, inicialmente desenvolvidos para dados 2D pós-empilhamento, foram amplamente aprimorados para aplicação em migração pré-empilhamento. Originalmente projetados para meios homogêneos, esses métodos foram ajustados para considerar as variações laterais no campo de velocidades, incorporando diversas correções para melhorar sua precisão. Destacam-se, nesse contexto, os métodos de migração *Phase shift plus interpolation* (PSPI) (Gazdag, 1978; Gazdag e Sguazzero, 1984), *Split-step* (SS) (Stoffa et al., 1990) e *Fourier finite difference* (FFD) (Ristow e Rühl, 1994), amplamente utilizados na indústria do petróleo. Outros trabalhos, na tentativa de contornar os problemas associados com variações significativas no modelo de velocidade, têm se concentrado na expansão direta do operador de raiz quadrada, sem introduzir aproximações no campo de velocidade. Esses trabalhos utilizam técnicas matemáticas como séries de Taylor e Padé, além de polinômios de Chebyshev (Gazdag, 1978; Gazdag e Sguazzero, 1984; Stoffa et al., 1990). No entanto, os erros de truncamento gerados por essas abordagens limitam os ângulos de propagação do campo de pressão, tornando muito difícil alcançar 90°. Essa limitação, refletida nos ângulos dos refletores recuperados na seção sísmica, representa uma desvantagem significativa do WEM. Para aproveitar plenamente as vantagens da migração sísmica com base na equação de onda unidimensional, é essencial evitar metodologias convencionais que utilizam expressões polinomiais aproximadas para o cálculo do operador raiz quadrada. Na literatura, dois métodos notáveis e bem-sucedidos, que não recorrem a aproximações, foram propostos: o método de decomposição em valores próprios (Grimbergen et al., 1998) e o esquema iterativo de Schulz acoplado (Higham, 1987), baseado na relação entre a função sinal da matriz e sua raiz quadrada. Considerando que a decomposição em valores próprios pode ter um alto custo computacional para modelos de grande escala (You et al., 2018), optamos por utilizar o esquema de Higham para calcular o número de onda vertical em nosso algoritmo WEM proposto.

Outro problema na implementação do algoritmo de imageamento WEM é a notória instabilidade no propagador de extrapolação em profundidade, causada pela presença de componentes de ondas evanescentes (Grimbergen et al., 1998; Wapenaar e Grimbergen, 1998). Kosloff e Baysal (1983) propõem suprimir essas ondas evanescentes no domínio do número de onda utilizando a transformada de Fourier e um filtro de corte ideal. No entanto, essa abordagem considera um modelo de subsuperfície com variação vertical de velocidade. Para um modelo de velocidade com variação lateral, sugerem empregar um filtro de corte ajustado à velocidade máxima em um determinado nível de profundidade, também recorrendo à transformada de Fourier como ferramenta. Como demonstrado por Thorbecke et al. (2004), a aplicação deste filtro de corte pode ser estendida à equação de onda unidimensional sem perda de generalidade. Exemplos numéricos mostram que, para a extrapolação em profundidade com a equação de onda completa, essa estratégia resulta na remoção de algumas ondas propagantes juntamente com as ondas evanescentes, levando a uma imagem migrada com pouca presença de refletores íngremes (Sandberg e Beylkin, 2009). Como alternativa, um dos métodos mais promissores é o projetor espectral (Kenney e Laub, 1995), que pode filtrar as ondas evanescentes sem perder nenhum componente de onda propagante. Para modelos de velocidade com a presença apenas de variação vertical, a combinação da transformada de Fourier e do filtro de corte ideal, como proposto por Kosloff e Baysal (1983), constitui tal projetor. No esquema de imageamento OWEM proposto nesta tese, implementamos um algoritmo para calcular os projetores espectrais que aproveita sua relação com a função sinal de uma matriz, que, por sua vez, utiliza recursões polinomiais da matriz (Auslander e Tsao, 1992; You et al., 2019).

Um aspecto crucial do esquema de imageamento que propomos é a eliminação da suposição de que o operador raiz quadrada pode ser tratado como um operador local. Em consequência, o extrapolador em profundidade não pode mais ser aplicado localmente e deve ser implementado como um operador derivado da exponencial de uma matriz. Embora muitos pesquisadores tenham se concentrado no cálculo do operador de raiz quadrada e na atenuação de ondas evanescentes, poucos têm abordado a construção desse operador exponencial de uma matriz. You et al. (2019) utilizaram a expansão em série de Taylor (TS) para aproximar a função exponencial de uma matriz. No entanto, nesta parte da tese, propomos o uso da expansão de Jacobi-Anger (JA) como uma alternativa mais eficiente para esse propósito. A expansão JA representa funções oscilatórias de forma mais natural, tornando-a particularmente adequada para aplicações envolvendo propagação de ondas, como a extrapolação de profundidade sísmica. Esta expansão converge mais rapidamente devido às propriedades das funções de Bessel, o que diminui o número de termos necessários para uma aproximação precisa (Watson, 1944). Além disso, a ortogonalidade das funções de Bessel minimiza a interferência cruzada entre os termos, aumentando ainda mais a precisão e a compactação da representação (Abramowitz e Stegun, 1972). Consequentemente, a expansão JA não só fornece uma aproximação mais exata com menos termos, mas também resulta em uma eficiência computacional significativa e precisão em simulações numéricas (Bowman, 1958). Com base no que foi exposto, e visando superar as limitações das abordagens convencionais para a solução das equações de onda unidimensionais, a última parte desta tese pretende integrar o projetor espectral, o esquema iterativo de Schulz acoplado e a expansão JA na técnica de imageamento WEM. Para validar a eficácia do esquema proposto, são computadas respostas ao impulso utilizando tanto a expansão TS quanto a expansão JA, além dos algoritmos convencionais WEM. Para obter resultados de imagem mais precisos e detalhados, migrações pós-empilhamento e pré-empilhamento são realizadas em modelos subsuperficiais complexos, empregando tanto métodos convencionais WEM quanto o algoritmo de migração sísmica proposto. Por fim, aplicamos esses métodos de migração a dados sísmicos reais.

Material e métodos

Para desenvolver a primeira parte deste trabalho (capítulo 1), realizamos uma revisão bibliográfica das principais técnicas voltadas para a melhoria da condição de imagem, com o objetivo de contornar os efeitos que contaminam a seção migrada gerada pela RTM. A condição de imagem causal proposta por Shen e Albertin (2015), que correlaciona os componentes descendente e ascendente da fonte e do receptor, respectivamente, mostrou-se eficaz na remoção de diversos tipos de artefatos. Contudo, essa abordagem requer a construção do campo de ondas analítico, realizada por meio de duas propagações, o que acarreta um elevado custo computacional. Esse fator foi identificado como um aspecto essencial a ser investigado e aprimorado. Nesse contexto, propomos um esquema eficiente para a construção do campo de ondas analítico, cuja implementação demandou um sólido domínio dos conceitos teóricos sobre propagação de ondas, separação explícita do campo de ondas e a técnica de migração RTM.

Na segunda parte desta tese (capítulo 2), conduzimos uma pesquisa bibliográfica detalhada sobre a implementação do esquema LSRTM no domínio da frequência. Nesse sentido, encontramos diversos trabalhos que utilizam diferentes técnicas, destacando-se o método proposto por Kim et al. (2022), que apresenta uma versão do FLSRTM eficiente em termos de memória. Embora essa abordagem reduza a quantidade de memória exigida pelo esquema de inversão, a técnica adotada para gerar a representação de baixo posto das funções de Green, utilizando o algoritmo SVD convencional, pode aumentar significativamente o tempo de cálculo, especialmente ao lidar com grandes conjuntos de dados ou modelos. Diante disso, para tornar a etapa de geração da representação de baixo posto das funções de Green mais eficiente, propomos o uso dos algoritmos SVD aleatório e comprimido. Portanto, o domínio dos conceitos teóricos sobre modelagem Born, migração sísmica, esquemas de inversão sísmica e técnicas SVD foi crucial para o desenvolvimento de nosso esquema FLSRTM com uso eficiente de memória por meio de métodos SVD estocásticos.

Na terceira parte desta tese (capítulo 3), investigamos os operadores de extrapolação em profundidade do campo de ondas utilizados no esquema WEM, destacando as principais limitações das aproximações tradicionais: o tratamento de ondas evanescentes, o imageamento de refletores com mergulhos acentuados e a estabilidade do propagador unidirecional. Para superar esses desafios, propomos um algoritmo de migração em profundidade que é robusto e eficiente. Esse algoritmo emprega um projetor espectral para suprimir modos evanescentes, o esquema iterativo de Schulz acoplado para o cálculo do operador raiz quadrada, e a expansão de Jacobi-Anger para uma construção estável do propagador de extrapolação. A implementação desse algoritmo exigiu um domínio sólido dos conceitos teóricos dos três componentes mencionados, além de um conhecimento aprofundado do esquema de migração em profundidade WEM

Com relação aos aspectos de implementação computacional, utilizamos a linguagem Fortran 90 para implementar os algoritmos descritos em cada capítulo, além do protocolo de comunicação distribuída (do inglês, "*Message Passing Interface*- MPI) para realizar a divisão do trabalho, otimizando assim o tempo total de execução. Os modelos, as imagens e os dados sísmicos foram plotados com o pacote *Seismic Unix* (Stockwell, 1999), o software de código aberto *Gnuplot* (Williams et al., 2010) e o sistema de composição tipográfica LaTeX (Lamport, 1994)

Produtos

Este trabalho resultou em um artigo científico e dois manuscritos, que correspondem aos capítulos desta tese. A seguir, é apresentada uma breve descrição de cada um deles. Além disso, são listados os subprodutos de cada capítulo, totalizando nove resumos expandidos apresentados em eventos de divulgação científica.

O capítulo 1 compreende o artigo intitulado **Up/down acoustic wavefield decomposition using a single propagation and its application in reverse time migration**, publicado na revista *Geophysics* (Revelo e Pestana, 2019). Nele, propomos um método alternativo para o cálculo do campo de ondas analítico, baseado na equação diferencial parcial de primeira ordem no tempo e resolvendo a equação da onda apenas uma vez. Como demonstrado por alguns exemplos numéricos, este método melhora o cálculo da separação explícita do campo de ondas, permite a aplicação eficiente da condição de imagem causal em RTM e produz imagens livres de ruído de baixa frequência.

Trabalhos em eventos:

- Reverse time migration with causal imaging condition using an improved method to calculate the analytical wavefield. 15th International Congress of the Brazilian Geophysical Society, 2017, doi: 10.1190/sbgf2017-257;
- An Improved Method to Calculate the Analytical Wavefield for Causal Imaging Condition. 79th EAGE Conference & Exhibition, 2017, doi: 10.3997/2214-4609.201701133;
- An improved method to calculate the analytical wavefield for causal imaging condition. SEG International Exposition & 87th Annual Meeting, 2017, doi: 10.1190/segam2017-17664808.1;
- De-primary TTI–RTM using the P-pure analytical wavefield. 81st EAGE Conference & Exhibition, 2019, doi: 10.3997/2214-4609.201900838;
- Reverse time migration as the transpose of forward operator by rapid expansion method (REM). SEG International Exposition & 89th Annual Meeting, 2019, doi: 10.1190/segam2019-3215582.1;
- Combination of the LSMME scheme and causal imaging condition to remove RTM artifacts. 17th International Congress of the Brazilian Geophysical Society, 2021, doi: 10.22564/17cisbgf2021.081.

O capítulo 2 refere-se ao manuscrito intitulado **Memory-efficient frequency-domain least-squares RTM using low-rank Green's functions via stochastic SVD algorithms**, no qual abordamos um desafio crítico na implementação da migração reversa no domínio da frequência por mínimos quadrados (FLSRTM): a grande demanda de memória para armazenar as funções de Green. Embora o FLSRTM tenha potencial para gerar modelos de refletividade de alta resolução, sua aplicação prática é limitada pela inviabilidade de armazenar funções de Green no hardware disponível. Para mitigar esse problema, propomos uma abordagem inovadora que utiliza funções de Green de baixo posto, decompostas por versões estocásticas do algoritmo de decomposição em valores singulares (SVD), tais como os algoritmos rSVD e cSVD. Nosso método permite o armazenamento eficiente dessas funções sem comprometer a eficiência computacional, oferecendo uma solução robusta para melhorar o desempenho e a viabilidade computacional na aplicação do esquema FLSRTM.

Trabalhos em eventos:

- Memory-efficient frequency-domain least-squares RTM using low-rank Green's functions via randomized SVD. IMAGE24 - International Meeting for Applied Geoscience & Energy, 2024.

Por fim, no capítulo 3, apresentamos o manuscrito intitulado **One-way wave-equation migration based on Jacobi-Anger expansion in arbitrarily lateral varying media**. Nele, abordamos os principais desafios da migração em profundidade usando a equação de onda unidirecional, como o tratamento de ondas evanescentes, o imageamento de estruturas com ângulos pronunciados, e a garantia de estabilidade. Propomos um método estável e eficiente que utiliza um projetor espectral para suprimir as ondas evanescentes e o esquema acoplado de Schulz para o cômputo do operador raiz quadrada. Além disso, introduzimos uma abordagem inovadora para a construção do operador de extrapolação usando a expansão de Jacobi-Anger, o que facilita a implementação eficiente do algoritmo de migração. Nossos resultados, demonstrados por meio de testes de resposta ao impulso, modelos subsuperficiais complexos e dados de campo, indicam melhorias significativas em precisão e na capacidade de imagear estruturas complexas em comparação com métodos tradicionais.

Trabalhos em eventos:

- One-way wave-equation migration for wide-angle and for strong lateral velocity variation using the Jacobi-Anger expansion. 83rd EAGE Conference & Exhibition, 2022, doi: 10.3997/2214-4609.202210898;
- One-way wave-equation migration based on the Jacobi-Anger expansion for a medium with a strong lateral velocity variation. 18th International Congress of the Brazilian Geophysical Society, 2023.

Referências

Abramowitz, M. e Stegun, I. A. (1972) Handbook of Mathematical Functions with Formulas, Graphs, and Mathematical Tables, National Bureau of Standards.

Andrade, P.; Pestana, R. e Revelo, D. E. (2017) Reverse time migration in the frequency domain by the rapid expansion method, Brazilian Journal of Geophysics, **35**(4):287–306.

Auslander, L. e Tsao, A. (1992) On parallelizable eigensolvers, Advances in Applied Mathematics, **13**:253–261.

Bamberger, A.; Chavent, G.; Hemon, C. e Lailly, P. (1982) Inversion of normal incidence seismograms, Geophysics, **47**(5):757–770.

Baysal, E.; Kosloff, D. e Sherwood, J. (1983) Reverse time migration, Geophysics, **48**(11):1514–1524.

Bowman, F. (1958) Introduction to Bessel Functions, Dover Publications.

Brandsberg-Dahl, S.; Chemingui, N.; Whitmore, D.; Crawley, S.; Klochikhina, E. e Valenciano, A. (2013) 3D RTM angle gathers using an inverse scattering imaging condition, 83th Annual Int. Meeting, SEG, Expanded Abstracts, pp. 3958–3962.

Claerbout, J. (1992) Earth Soundings Analysis: Processing Versus Inversion, Blackwell Scientific Publications.

Claerbout, J. F. (1971) Toward a unified theory of reflector mapping, Geophysics, **36**(3):467–481.

Costa, J. C.; Medeiros, W. E.; Schimmel, M.; Santana, F. L. e Schleicher, J. (2018) Reverse time migration using phase crosscorrelation, Geophysics, **83**:S345–S354.

Dai, W. e Schuster, G. T. (2013) Plane-wave least-squares reverse-time migration, Geophysics, **78**(4):S165–S177.

Dai, W.; Fowler, P. e Schuster, G. T. (2012) Multi-source least-squares reverse time migration, Geophysical Prospecting, **60**(4):681–695.

Dong, S.; Cai, J.; Guo, M.; Suh, S.; Zhang, Z.; Wang, B. e Li, Z. (2012) Least-squares reverse time migration: towards true amplitude imaging and improving the resolution, In: *82nd*

Annual International Meeting, SEG, Expanded Abstracts, pp. 1–5.

Du, X.; Fowler, P. e Fletcher, R. (2014) Recursive integral time-extrapolation methods for waves: A comparative review, Geophysics, **79**(1):T9–T26.

Dutta, G. e Schuster, G. T. (2014) Attenuation compensation for least-squares reverse time migration using the viscoacoustic-wave equation, Geophysics, **79**(6):S251–S262.

Erichson, N. B.; Brunton, S. L. e Kutz, J. N. (2017) Compressed Singular Value Decomposition for Image and Video Processing, In: *2017 IEEE International Conference on Computer Vision Workshops (ICCVW)*, pp. 1880–1888.

Erichson, N. B.; Voronin, S.; Brunton, S. L. e Kutz, J. N. (2019) Randomized Matrix Decompositions Using R, Journal of Statistical Software, **89**(11):1–48.

Etgen, J.; Gray, S. H. e Zhang, Y. (2009) An overview of depth imaging in exploration geophysics, Geophysics, **74**(6):WCA5–WCA17.

Fei, T. W.; Luo, Y. e Qin, F. (2014) An endemic problem in reverse-time migration, 84th Annual Int. Meeting, SEG, Expanded Abstracts, pp. 3811–3815.

Fei, T. W.; Luo, Y.; Yang, J.; Liu, H. e Quin, F. (2015) Removing false images in reverse time migration: The concept of de-primary, Geophysics, **80**:S237–S244.

Fletcher, R. P.; Fowler, P. J.; Kitchenside, P. e Albertin, U. (2006) Suppressing unwanted internal reflections in prestack reverse-time migration, Geophysics, **71**:E79–E82.

Gazdag, J. (1978) Wave equation migration with phase-shift method, Geophysics, **43**:1342–1351.

Gazdag, J. e Sguazzero, P. (1984) Migration of seismic data by phase shift plus interpolation, Geophysics, **49**:124–131.

Golub, G. e Van Loan, C. (1996) Matrix Computations, Johns Hopkins University Press, 3º edic..

Grimbergen, J. L. T.; Dessing, F. J. e Wapenaar, K. (1998) Modal expansion of one-way operators in laterally varying media, Geophysics, **63**:995–1005.

Gu, M. (2015) Subspace Iteration Randomization and Singular Value Problems, SIAM Journal on Scientific Computing, **37**(3):1139–1173.

Guitton, A.; Kaelin, B. e Biondi, B. (2007) Least-squares attenuation of reverse-time migration artifacts, Geophysics, **72**:S19–S23.

Halko, N.; Martinsson, P. G. e Tropp, J. A. (2011) Finding structure with randomness: Probabilistic algorithms for constructing approximate matrix decompositions, SIAM Review, **53**(2):217–288.

Halko, N. P. (2012) Randomized methods for computing low-rank approximations of matrices, Tese de Doutorado, USA.

Herrmann, F. J. e Li, X. (2012) Efficient least-squares imaging with sparsity promotion and compressive sensing, Geophysical Prospecting, **60**(4):696–712.

Higham, N. J. (1987) Computing real square roots of a real matrix, Linear Algebra Appl., **88/89**:405–430.

Hu, L. e McMechan, G. A. (1987) Wave-field transformations of vertical seismic profiles, Geophysics, **52**:307–321.

Ji, H. e Li, Y. (2014) GPU Accelerated Randomized Singular Value Decomposition and Its Application in Image Compression, In: *Modeling, Simulation, and Visualization Student Capstone Conference.*

Kenney, C. S. e Laub, A. J. (1995) The matrix sign function, IEEE Transactions on Automatic Control, **40**:1330–1348.

Kim, S.; Kim, Y. S. e Chung, W. (2022) Fast and memory-efficient frequency domain least-squares reverse time migration using singular value decomposition (SVD), IEEE Transactions on Geoscience and Remote Sensing, **60**:1–11.

Kosloff, D. D. e Baysal, E. (1983) Migration with the full acoustic wave equation, Geophysics, **48**(6):677–687.

Lamport, L. (1994) LaTeX: A Document Preparation System, Addison-Wesley, Reading, Massachusetts, $2^{\underline{o}}$ edic., ISBN 0-201-52983-1.

Liu, F.; Zhang, G.; Morton, S. e Leveille, J. (2011) An effective imaging condition for reverse-time migration using wavefield decomposition, Geophysics, **76**:S29–S39.

Liu, Q. e Peter, D. (2018) One-step data-domain least-squares reverse time migration, Geophysics, **83**(4):R361–R368.

Liu, Q. e Peter, D. (2020) Square-Root Variable Metric-Based Nullspace Shuttle: A Characterization of the Nonuniqueness in Elastic Full-Waveform Inversion, Journal of Geophysical Research: Solid Earth, **125**(2).

Liu, Y.; Liu, W.; Wu, Z. e Yang, J. (2022) Reverse time migration with an exact two-way illumination compensation, Geophysics, **87**(2):S53–S62.

Martinsson, P.-G. (2019) Randomized methods for matrix computations.

Martinsson, P.-G.; Rokhlin, V. e Tygert, M. (2011) A randomized algorithm for the decomposition of matrices, Applied and Computational Harmonic Analysis, **30**(1):47–68.

McMechan, G. A. (1983) Migration by extrapolation of time-dependent boundary values, Geophysics Prospecting, **31**(3):413–420.

Nemeth, T.; Wu, C. e Schuster, G. T. (1999) Least-squares migration of incomplete reflection data, Geophysics, **64**(1):208–221.

Pestana, R.; dos Santos, A. W. G. e Araujo, E. S. (2014) RTM imaging condition using impedance sensitivity kernel combined with Poynting vector, 84th Annual Int. Meeting, SEG, Expanded Abstracts, pp. 3763–3768.

Pestana, R. C. e Stoffa, P. L. (2010) Time evolution of wave equation using rapid expansion method, Geophysics, **75**:T121–T131.

Ren, H.; Wang, H. e Chen, S. (2013) Least-squares reverse time migration in frequency domain using the adjoint-state method, Journal of Geophysics and Engineering, **10**(3).

Revelo, D.; Pestana, R. e Gomez, L. (2016) Reverse time migration (RTM) using analytical wavefield and causal imaging condition, 78th Annual Intern. Conference and Exibition, EAGE, Extended Abstract, **Th P1 01**.

Revelo, D. E. e Pestana, R. C. (2019) Up/down acoustic wavefield decomposition using a single propagation and its application in reverse time migration, Geophysics, **84**(4):S341–S353.

Ristow, D. e Rühl, T. (1994) Fourier finite-difference migration, Geophysics, **59**(12):1882–1893.

Rocha, D.; Tanushev, N. e Sava, P. (2016) Acoustic wavefield imaging using the energy norm, Geophysics, **81**:S151–S163.

Sandberg, K. e Beylkin, G. (2009) Full-wave-equation depth extrapolation for migration, Geophysics, **74**(6):WCA121–WCA128.

Sarlos, T. (2006) Improved Approximation Algorithms for Large Matrices via Random Projections, In: *47th Annual IEEE Symposium on Foundations of Computer Science*, pp. 143–152, IEEE.

Schuster, G. T. (1993) Least-squares cross-well migration, In: *63rd Annual International Meeting, SEG, Expanded Abstracts*, pp. 110–113.

Shen, P. e Albertin, U. (2015) Up-Down separation using Hilbert transformed source for causal imaging condition, pp. 4175–4179.

Stockwell, J. W. (1999) The CWP/SU: Seismic Unix package, Computers & Geosciences, **25**(4):415–419.

Stoffa, P.; Fokkema, J.; de Luna Freire, R. e Kessinger, W. (1990) Split-step fourier migration, Geophysics, **55**:410–421.

Stolk, C. C.; de Hoop, M. V. e Root, T. J. P. M. O. (2009) Inverse scattering of seismic data in the reverse time migration (RTM) approach, Proceedings of the Project Review, Geo-Mathematical Imaging Group of Purdue University, pp. 91–108.

Sun, J.; Fomel, S. e Ying, L. (2016) Low-rank one-step wave extrapolation for reverse time migration, Geophysics, **81**:S39–S54.

Symes, W. W. (2009) The seismic reflection inverse problem, Inverse Problems, **25**(12):123008.

Tal-Ezer, H.; Kosloff, D. e Koren, Z. (1987) An accurate scheme for seismic forward modelling, Geophysical Prospecting, **35**(5):479–490.

Tarantola, A. (1984) Inversion of seismic reflection data in the acoustic approximation, Geophysics, **49**:1942–2156.

Thorbecke, J. W.; Wapenaar, K. e Swinnen, G. (2004) Design of one-way wavefield extrapolation operators, using smooth functions in WLSQ optimization, Geophysics, **69**(4):1037–1045.

Tropp, J. A. e Webber, R. J. (2023) Randomized algorithms for low-rank matrix approximation: Design, analysis, and applications.

Wang, E. e Liu, Y. (2017) The hybrid absorbing boundary condition for one-step extrapolation and its application in wavefield decomposition-based reverse time migration, Journal of Geophysics and Engineering, **14**:1177–1188.

Wang, W.; McMechan, G. A.; Tang, C. e Xie, F. (2016a) Up/Down and P/S decompositions of elastic wavefields using complex seismic traces with applications to calculating poynting vectors and angle-domain common-image gathers from reverse time migrations, Geophysics, **81**:S181–S194.

Wang, W.; McMechan, G. A. e Xie, F. (2016b) Analysis of up/down decomposed acoustic reverse time migration images, Geophysics, **81**:S253–S259.

Wang, Y.; Zheng, Y.; Xue, Q.; Chang, X.; Fei, T. e Luo, Y. (2017) Reverse time migration of multiples: Reducing migration artifacts using the wavefield decomposition imaging condition, Geophysics, **82**:S307–S314.

Wapenaar, K. e Grimbergen, J. L. T. (1998) A discussion on stability analysis of wave field depth extrapolation, 68th Annual International Meeting, SEG, Expanded Abstracts, pp. 1716–1719.

Watson, G. N. (1944) A Treatise on the Theory of Bessel Functions, Cambridge University Press.

Whitmore, N. D. (1983) Iterative depth migration by backward time propagation, In: *SEG Technical Program Expanded Abstracts 1983*, pp. 382–385.

Williams, T.; Kelley, C. e outros (2010) Gnuplot 4.4: an interactive plotting program, `http://gnuplot.sourceforge.net/`.

Wong, M.; Ronen, S. e Biondi, B. (2012) Least-squares reverse time migration/inversion for ocean bottom data: A case study, In: *81st Annual International Meeting, SEG, Expanded Abstracts*, pp. 2369–2373.

Xue, Z.; Chen, Y.; Fomel, S. e Sun, J. (2016) Seismic imaging of incomplete data and simultaneous-source data using least-squares reverse time migration with shaping regularization, Geophysics, **81**(1):S11–S20.

Yao, G. e Jakubowicz, H. (2016) Least-squares reverse-time migration in a matrix-based formulation, Geophysical Prospecting, **64**(3):611–621.

Yao, G.; Wu, B.; da Silva, N. V.; Debens, H. A.; Wu, D. e Cao, J. (2022) Least-squares reverse time migration with a multiplicative Cauchy constraint, Geophysics, **87**(3):S151–S167.

Yoon, K. e Marfurt, K. J. (2006) Reverse-time migration using the Poynting vector, Exploration Geophysics, **37**:102–107.

You, J.; Wu, R.-S. e Liu, X. (2018) One-way true-amplitude migration using matrix decomposition, Geophysics, **83**(5):S387–S398.

You, J.; Liu, Z.; Liu, J. e Li, C. (2019) One-way propagators based on matrix multiplication in arbitrarily lateral varying media with GPU implementation, Computers and Geosciences, **130**:32–42.

Youn, O. e Zhou, H. (2001) Depth imaging with multiples, Geophysics, **66**:246–255.

Zhang, Y. e Sun, J. (2009) Practical issues in reverse time migration: True amplitudes gathers, noise removal and harmonic-source encoding, First Break, **26**:24–25.

Zhang, Y. e Zhang, G. (2009) One-step extrapolation method for reverse time migration, Geophysics, **74**(4):A29–A33.

Zhang, Y.; Zhang, G.; Yingst, D. e Sun, J. (2007) Explicit marching method for reverse-time migration, 77th Annual Int. Meeting, SEG, Expanded Abstracts, pp. 2300–2304.

Zhang, Y.; Duan, L. e Xie, Y. (2015) A stable and practical implementation of least-squares reverse time migration, Geophysics, **80**:V23–V31.

Zhao, Z. e Sen, M. K. (2019) Frequency-domain double-plane-wave least-squares reverse time migration, Geophysical Prospecting, **67**(8):2061–2084.

Zheng, Y.; Wang, Y. e Chang, X. (2018) 3D forward modeling of upgoing and downgoing wavefields using Hilbert transform, Geophysics, **83**:F1–F8.

1

Up/Down Acoustic Wavefields Decomposition Using a Single Propagation and its Application in Reverse Time Migration

This chapter has been published as Daniel E. Revelo and Reynam C. Pestana. *Up/down acoustic wavefield decomposition using a single propagation and its application in reverse time migration.* In: Geophysics, 84(4) (July-August 2019), pp. S341-353. Minor modifications have been applied to maintain consistency within this thesis.

Abstract

The separation of up- and downgoing wavefields is an important technique in the processing of multicomponent recorded data, propagating wavefields, and reverse time migration (RTM). Most of the previous methods for separating up/down propagating wavefields can be grouped according to their implementation strategy: requirement to save time steps to perform Fourier transform over time, or construction of the analytical wavefield through a solution of the wave equation twice (one for the source and another for the Hilbert transformed source), where both strategies have shown a high computational cost. For computing the analytical wavefield we are proposing an alternative method based on the first-order partial equation in time and by just solving the wave equation once. Our strategy improves the computation of wavefield separation and can bring the causal imaging condition into practice. For time extrapolation, we are using the rapid expansion method (REM) to compute the wavefield and its first-order time derivative and then we can compute the analytical wavefield. By computing the analytical wavefield, we can, therefore, separate the wavefield into up- and downgoing components for each time step in an explicit way. Applications to synthetic models indicate that our proposed method allows performing the wavefields decomposition similarly to the obtained by the conventional method, as well as a potential application for the 3D case. For RTM applications, we can now employ the causal imaging condition for several synthetic examples. Acoustic RTM up/down decomposition demonstrate that it can successfully remove the low-frequency noise, which is common in the typical crosscorrelation imaging condition, and usually removed by applying a Laplacian filter. Moreover, our method is efficient in terms of computational time when compared to RTM using an analytical wavefield computed by two propagations, and it is a little more costly than conventional RTM using the crosscorrelation imaging condition.

Introduction

Prestack reverse time migration (RTM) (Baysal et al., 1983; McMechan, 1983) has become one of the most used migration approaches because it has the ability to image arbitrarily complex and steeply dipping structures in the subsurface, whereby it allows obtaining a high-resolution imaging result. In the traditional RTM, the source and receiver wavefields are forward and backward propagated and correlated along the time axis at zero-lag. The resulting image obtained by applying the conventional crosscorrelation between source and receiver wavefields is always contaminated by high-amplitude, spatial-low-frequency noise and false images due to the unwanted crosscorrelation of head, diving, and backscattered waves, caused by the use of a migration velocity model with strong velocity gradients or sharp velocity interfaces. In recent years, more attention has been given to improving the imaging condition and reducing the low-frequency noise. (Fei et al., 2015) gave a comparative review of the methods that have been proposed in the literature to address this issue and grouped them into three categories: before, after, or during application of the imaging condition.

Fletcher et al. (2006) suggested a procedure for removing unwanted reflections during propagation of wavefields. In this procedure, the main idea is to apply a directional damping term to the non-reflecting wave equation in areas of the velocity model where unwanted reflections occur. It is inconvenient to apply this approach on a model with very complicated interfaces due to the requirement of additional knowledge about the direction in which energy is propagating. Using a similar idea, Yoon and Marfurt (2006) used the fact that reflection events (narrow opening angles) and artifacts (far offset) have different ranges of opening angle, therefore the wave-propagation directions can be used to eliminate artifacts. In this way, before applying the imaging condition, the angle between the incident and reflected waves is limited via calculating Poynting vectors. The method advocated by Yoon and Marfurt (2006) works well for simple models, but requires an additional storage cost and it does not produce satisfactory results in complex subsurfaces (Guitton et al., 2007). A practical approach in which the artifacts are filtered after imaging is the Laplacian filter (Youn and Zhou, 2001; Zhang and Sun, 2009), which is easy to apply and shows good attenuation of the low-frequency noise, but can damage the signal of interest (Guitton et al., 2007).

Another way to address this type of migration artifact is to modify the imaging condition. To this end Whitmore and Crawley (2012) and Brandsberg-Dahl et al. (2013) presented an imaging process based on a generalized inverse scattering theory (Stolk et al., 2009). In that process, the artifacts caused by backscattered energy are attenuated by using the combination of two separate images: one is the product of the time derivatives of the source and receivers wavefields, and the other is the product of the spatial gradients of the source and the receivers wavefields. Then, the weighted sum of these images is calculated in order to generate the migrated image. As an application of the inverse-scattering imaging condition, Pestana et al. (2014) proposed a scheme where the downgoing component of the source wavefield - obtained by applying the Poynting vector - is used in the application of the mentioned imaging process. More recently, based on the energy norm concept, Rocha et al. (2016) developed a flexible imaging condition which is used not only to attenuate backscattering artifacts, but also to attenuate any selected reflection angle. The energy norm condition, besides being similar to the inverse-scattering imaging condition is also related to the Laplacian filter, as shown by the author. In general, the inverse-scattering imaging condition produces images where the backscattered noise is reduced significantly and the true reflection data is preserved, i.e., it produces images with much higher quality than the conventional correlation method.

Liu et al. (2011) proposed an imaging condition based on the decomposition of the wavefield into one-way components, which also belongs to the group of methods that modify the standard zero-lag crosscorrelation between the source and receiver wavefields. The imaging condition introduced by Liu et al. (2011) only allows correlation of wave components that propagate in opposite directions. This method is an implicit separation technique that can successfully remove many types of artifacts while preserving the imaging amplitude without the need to apply a Laplacian filter after the imaging condition. However, an incomplete wavefield decomposition gives rise to imaging artifacts such as shown by Fei et al. (2014), Shen and Albertin (2015) and Wang et al. (2016b). Since the method of Liu et al. (2011) is an implicit separation method, the up- and downgoing wavefields are not available and its applications are limited. To address the wavefield separation, the wave-propagation direction is usually defined in the double Fourier domain ($\omega - k$). In the frequency-wavenumber domain, wave-propagation is defined by the sign of the frequency and the wavenumber (Hu and McMechan, 1987; Liu et al., 2011). If we use the conventional wavefield decomposition method in the time-domain, we should store the wavefields and perform a Fourier transform along the time axis. This process increases the input/output cost, because the time axis is the slowest dimension of the stored wavefield, and the Fourier transform operates most efficiently on data that are stored contiguously.

On the other hand, if we can define a time-domain wavefield whose spectrum only contains a positive or negative frequency (Shen and Albertin, 2015; Wang et al., 2016a; Wang et al., 2017), we can define the wave-propagation direction using the sign of the spatial wavenumber and avoid the high I/O cost. This signal is the analytical signal which is widely used in signal processing. The analytical signal is a complex variable whose real part is the signal itself and its complex part is the Hilbert transform of the real part. For RTM, we extend the analytic-signal concept and call it the analytical wavefield (Zhang et al., 2007; Sun et al., 2016). Because the analytical wavefield only contains positive frequencies, the up- and downgoing wave components can then be conveniently obtained by applying a 1D Fourier filter along the depth direction. Compared with the method of Liu et al. (2011) of constructing RTM images, a major advantage of using analytical wavefields is that completely separated up- and downgoing wavefields are available (explicit form) to different applications, and it also eliminates the computational-storage requirement as well as the need of expensive fast Fourier transforms (FFT).

In recent years, various works on wavefield decomposition using the analytical wavefield have been presented. To perform the wavefield extrapolation in time and evaluate the Laplacian operator, the conventional finite-differences method (FD) was adopted by Shen and Albertin (2015), Wang et al. (2016a), Wang et al. (2016b) and Zheng et al. (2018), followed by the construction of the analytical wavefield. In a recent paper presented by Shen and Albertin (2015), the imaginary part of the analytical wavefield is obtained by applying a temporal Hilbert transform to the source term of the wave equation followed by a conventional propagation. The pair of wavefields - the one propagated with a conventional source and the other generated by its Hilbert transform - constitutes the analytical wavefield. Shen and Albertin (2015) proposed a causal imaging condition that correlates the downgoing source component with the upgoing receiver component for subsurface imaging. This method was tested and proved to be successful on removing many types of salt-imaging artifacts that were present in the images obtained from the conventional crosscorrelation imaging condition

(Claerbout, 1971).

One-step methods have been developed in order to avoid numerical dispersion that is present in the FD method when the spatial interval or temporal step is large; Du et al. (2014) reviewed these methods and named them recursive integral time extrapolation (RITE) methods. In Revelo et al. (2016) and Wang and Liu (2017), the implementation of these schemes for the analytical wavefield extrapolation is presented, as well as its application in the construction of the unidirectional components of the wavefield; for RTM both source and receiver wavefields were extrapolated in time and the source and receiver wavefields were separated into their up- and downgoing components for each time step in an explicit way based on Shen and Albertin (2015). The clear distintion between the method in Revelo et al. (2016) and the one proposed by Shen and Albertin (2015) is that Revelo et al. (2016) used a first-order wave-equation solution with an analytical source term, while in Shen and Albertin (2015) it was necessary to solve the wave equation twice: once for the source and another time for the Hilbert transform of the source. In relation to the work of Liu et al. (2011), the major difference is that the method proposed by Shen and Albertin (2015) and also used by Revelo et al. (2016) can provide an explicit separation of the wavefield, while the scheme of Liu et al. (2011) results in an implicit separation.

In this article, we present a detailed version of the proposed method by Pestana and Revelo (2017), where the analytical wavefield is calculated using the rapid expansion method (REM) (Pestana and Stoffa, 2010). The REM propagates waves free of numerical dispersion noise and is able to extrapolate waves in time using a time step up to Nyquist's limit. With the REM we can also obtain the first-order time derivative of the wavefield at the same time step and thus compute the Hilbert transform of the wavefield as proposed by Zhang and Zhang (2009). After that, we can separate the wavefields into their up- and downgoing components. In our proposed method, the wave equation is only solved once, improving the computational efficiency of the wavefield separation procedure and therefore the application of the causal imaging condition for RTM. In the following sections, we first introduce the wavefield decomposition-based RTM with the causal imaging condition and illustrate the methodology of up- and downgoing decomposition using analytical wavefields. Then, we derive our improved method to calculate the analytical wavefield via REM. Numerical examples are given to demonstrate the validity of the proposed method of explicit wavefield separation (two dimensions and three dimensions) and the effectiveness of the causal imaging condition in RTM images. Finally, conclusions are drawn.

Methodology

Causal imaging condition for RTM

RTM is a method widely used to obtain an accurate subsurface image in and below areas with both geological and velocity complexities. The zero-lag crosscorrelation between the extrapolated source (S) and receiver (R) wavefields is the nonsource-normalized crosscorrelation imaging condition conventionally used in RTM. This imaging condition was proposed originally by Claerbout (1971) and is defined as follows:

$$I_{cc}(\mathbf{x}) = \int_0^T S(\mathbf{x},t)\; R(\mathbf{x},t)\; dt, \tag{1.1}$$

where $\mathbf{x} = (x, z)$, t represents the time, T is the total time of propagation, and $I_{cc}(\mathbf{x})$ is the crosscorrelation image. The major drawback of RTM is that the two-way wave equation generates low-frequency back-scattering noise and false images when reflecting interfaces or strong velocity gradients exist in the migration velocity model (Liu et al., 2011; Fei et al., 2015; Wang et al., 2017). Taking into account that different artifacts observed in the RTM image are associated with the direction of the wavefield propagation (correlated), the decomposition of source and receiver wavefields into their up- and downgoing components can be used to remove the low-frequency noise and another types of artifacts present in RTM (Liu et al., 2011; Fei et al., 2014; Wang et al., 2016b).

During the acoustic RTM, the source and receiver extrapolated wavefields contain up- (u) and downgoing (d) components, which can be partitioned mathematically as

$$S(\mathbf{x},t) = S_d(\mathbf{x},t) + S_u(\mathbf{x},t) \tag{1.2}$$

and

$$R(\mathbf{x},t) = R_d(\mathbf{x},t) + R_u(\mathbf{x},t). \tag{1.3}$$

Using equations 1.2 and 1.3, we can rewrite equation 1.1 as follows (Liu et al., 2011):

$$\begin{aligned} I_{cc}(\mathbf{x}) = &\int_0^T S_d(\mathbf{x},t)\; R_u(\mathbf{x},t)\; dt + \int_0^T S_u(\mathbf{x},t)\; R_d(\mathbf{x},t)\; dt \\ &+ \int_0^T S_d(\mathbf{x},t)\; R_d(\mathbf{x},t)\; dt + \int_0^T S_u(\mathbf{x},t)\; R_u(\mathbf{x},t)\; dt. \end{aligned} \tag{1.4}$$

The high-amplitude and low-frequency noise present in the migrated images occurs at shallow depths and is associated with the wavefields propagating in the same direction, corresponding to the last two terms of the equation 1.4. On the other hand, the crosscorrelation of wavefields with opposite directions of propagation will give rise to an effective image. By using the wavenumber to determine the direction of the wavefields' propagation (more specifically, the opposite directions), Liu et al. (2011) introduced an effective imaging condition that uses a sum of $S_d R_u$ and $S_u R_d$. More recently, taking into account the angle between the wavenumber vectors of the source and receiver wavefields, Rocha et al. (2016) showed that their energy imaging condition can attenuate also the low-frequency noise and preserves the reflectors. The application of the imaging conditions proposed by Liu et al. (2011) and Rocha et al. (2016) successfully removes the low-frequency artifacts; however, these imaging conditions can not differentiate between the first two terms of equation 1.4, which may generate different backscattering-related artifacts (Fei et al., 2014; Wang et al., 2016b).

According to Fei et al. (2015), the second term of equation 1.4, $S_u(\mathbf{x},t)\, R_d(\mathbf{x},t)$, is the upward-turned raypath result, which has the same traveltime of the physical primary raypath and can generate a false image in RTM in most cases. Therefore, this term should also be excluded from the final image. In order to avoid the low-frequency noise produced by the crosscorrelation imaging condition and the artifacts shown in RTM results, Revelo et al. (2016) used a causal - or de-primary - imaging condition (Shen and Albertin, 2015; Fei et al., 2015) that is given by the first term of equation 1.4. It just correlates the downgoing component of the source, S_d, with the upgoing component of receiver wavefield, R_u, which can be written as

$$I_{causal}(\mathbf{x}) = \int_0^T S_d(\mathbf{x},t)\ R_u(\mathbf{x},t)\ dt. \tag{1.5}$$

This imaging condition will correlate wavefields only at points in space that correspond to seismic reflectors, avoiding noise along wavepaths and artifacts which are typical of conventional RTM.

Up/down separation using analytical wavefields

In order to obtain the individual components involved in equation 1.5, we need to introduce a procedure for explicit wavefield separation. The up/down separation is based on the sign of the apparent propagation velocity along the depth z-axis (v_z), which using the dispersion relation is given by (Wang et al., 2016a)

$$v_z = \omega/k_z, \tag{1.6}$$

where ω is the angular frequency and k_z is the apparent vertical wavenumber. Then, a straightforward way to perform the source-side wavefield decomposition in the $\omega - k$ domain can be implemented as follows (Hu and McMechan, 1987; Liu et al., 2011)

$$S_u(k_z,\omega) = \begin{cases} S(k_z,\omega), & \text{if } \omega/k_z < 0 \\ 0, & \text{if } \omega/k_z \geq 0 \end{cases} \tag{1.7}$$

and

$$S_d(k_z,\omega) = \begin{cases} S(k_z,\omega), & \text{if } \omega/k_z \geq 0 \\ 0, & \text{if } \omega/k_z < 0, \end{cases} \tag{1.8}$$

where $S(k_z,\omega)$ is the 2D Fourier transform of the source acoustic wavefield. The application of equations 1.7 and 1.8 requires knowing ω before the wavefield separation, which means that wavefield extrapolation must be completed and stored before performing the 2D Fourier transform over time, which is often expensive in terms of memory. In order to eliminate the problem described, analytical traces can be employed.

The analytical trace $\hat{f}(t)$ is constructed with the original real-valued trace $f(t)$ as the real part, and the Hilbert transform $\mathcal{H}\{\cdot\}$ of $f(t)$ as the imaginary part (Fei et al., 2015)

$$\hat{f}(t) = f(t) + i\,\mathcal{H}\{f(t)\}. \tag{1.9}$$

Unlike the real trace $f(t)$, which has a symmetric amplitude spectrum in the Fourier domain, $\hat{f}(t)$ only contains a positive spectrum (Gabor, 1946; Ville, 1948). Figure 1.1 illustrates the properties of the analytical trace; in this example, a Ricker wavelet with dominant frequency of 20 Hz and 0.5 ms as time interval was used (Figure 1.1a). In Figure 1.1c we can note an important aspect: the amplitude spectrum at negative frequencies is zero, and doubled at positive frequencies.

Based on the definition of analytical trace, the analytical (complex) wavefield can be defined as $\hat{P} = P(\mathbf{x},t) + iQ(\mathbf{x},t)$, where $P(\mathbf{x},t)$ is the pressure wavefield and $Q(\mathbf{x},t)$ its Hilbert transform, i.e., $Q(\mathbf{x},t) = \mathcal{H}\{P(\mathbf{x},t)\}$. For general media, this complex pressure wavefield $\hat{P}$ satisfy a first-order partial equation in time (Zhang and Zhang, 2009). Since analytical wavefields contains only positive frequencies, the temporal Fourier transform needed in the scheme of Hu and McMechan (1987) can be avoided, and the procedure to perform up- and downgoing separation in the $t-k$ domain is simplified into

$$S_u(k_z,t) = \begin{cases} \hat{S}(k_z,t), & \text{if } k_z < 0 \\ 0, & \text{if } k_z \geq 0, \end{cases} \tag{1.10}$$

and

$$S_d(k_z,t) = \begin{cases} \hat{S}(k_z,t), & \text{if } k_z \geq 0 \\ 0, & \text{if } k_z < 0, \end{cases} \tag{1.11}$$

where $\hat{S}$ is the source analytical wavefield. Equations 1.10 and 1.11 represent the up- and downgoing components of the source wavefield; this separation is more efficient than the one presented by equations 1.7 and 1.8, because it requires only a 1D inverse Fourier transform over the k_z-axis. An alternative form to equations 1.10 and 1.11 can be obtained following Shen and Albertin (2015), which used a Fourier transform along the depth direction of the analytical wavefield considering mono-frequency components (Liu et al., 2011). The upgoing component of the source wavefield, S_u, in space and time becomes

$$S_u(x,z,t) = \frac{1}{2\pi}\Re \int_{-\infty}^{+\infty}\int_{-\infty}^{+\infty} \hat{S}(x,z',t)e^{ik_z(z-z')}\kappa(k_z)dz'dk_z, \tag{1.12}$$

where

$$\kappa(k_z) = \begin{cases} 1, & \text{if } k_z < 0 \\ 0, & \text{if } k_z \geq 0. \end{cases} \tag{1.13}$$

The downgoing source wavefield component forward in time, S_d, is obtained using the analytical source wavefield in equation 1.12 and replacing κ by $1-\kappa$. Figure 1.2 shows a process flowchart to implement equation 1.12 applied to a wavefield that propagates in a three-layer velocity model.

Calculation of analytical wavefield by REM

In order to apply the causal imaging condition (equation 1.5), explicit wavefield separation is required. As shown above, the analytical wavefield must be calculated in order to obtain the explicit wavefield components in a cheap way regarding computacional storage. In recent years, several methods have been proposed to construct this wavefield. The conventional approach to construct the imaginary part of the analytical wavefield is based on the principle that the Hilbert transform, $\mathcal{H}_t$, commutes with the acoustic wave-equation operator (Shen and Albertin, 2015), that is

$$\mathcal{H}_t\left(\frac{1}{v^2(\mathbf{x})}\partial_t^2 - \nabla^2\right)P(\mathbf{x},t) = \left(\frac{1}{v^2(\mathbf{x})}\partial_t^2 - \nabla^2\right)\mathcal{H}_t\, P(\mathbf{x},t) = \mathcal{H}_t\, f(\mathbf{x}_S,t), \tag{1.14}$$

where $v(\mathbf{x})$ is the propagation velocity in the medium, ∇^2 is the Laplacian operator and f is the source wavelet. Thus, the imaginary part of the analytical wavefield can be obtained by solving the wave equation with its forward in time Hilbert transformed source term. Shen and Albertin (2015), Wang et al. (2017), and Zheng et al. (2018) solved the real and the imaginary part of the analytical wavefield individually: from the wave equation with its source term corresponding to the original source wavelet, and its Hilbert transform in time, respectively. The disadvantage of this approach is that two wavefield propagations are required, which can be computationally expensive for large two-dimensional models or 3D case applications.

A different approach to perform explicit wavefield separation, based on the solution of a first-order wave equation using as a source term the analytical signal of the source pulse (Zhang and Zhang, 2009), has also been presented. In this way, Revelo et al. (2016) used the one-step extrapolation (OSE) matrix method to compute the analytical wavefield (Revelo and Pestana, 2016), in which two wavefield propagations (for P and Q) are carried out implicitly in time. Using a similar idea, Wang and Liu (2017) proposed a procedure that uses the low-rank one-step extrapolation method (Fomel et al., 2013); since this is an FFT-based algorithm, the main disadvantage is the number of Fourier transforms (direct and inverse) that must be applied for every marching time step.

Here, we propose computing the analytical wavefield by solving the wave equation only once (Pestana and Revelo, 2017). In order to do this, we have taken into account the relation between Q and P proposed by Zhang and Zhang (2009)

$$Q(\mathbf{x},t) = \frac{1}{L}\frac{\partial P(\mathbf{x},t)}{\partial t}, \tag{1.15}$$

where L is a pseudo-differential operator in the space domain, defined by $L = v(\mathbf{x})\sqrt{-\nabla^2}$. Its symbolic representation is $L = v(\mathbf{x})\sqrt{k_x^2 + k_z^2}$, where k_x and k_z are the wavenumber components. In order to obtain the pressure wavefield and its first-order time derivative, let us consider the acoustic constant-density wave equation, without a source term, which can be written as

$$\frac{\partial^2 P(\mathbf{x},t)}{\partial t^2} = -L^2 P(\mathbf{x},t), \tag{1.16}$$

where $-L^2 = v^2\nabla^2$ and $P(\mathbf{x},t)$ is the pressure field at location $\mathbf{x} = (x,\, z)$ and time t. In order to solve the acoustic wave equation in time we use the REM as proposed by Pestana and Stoffa (2010), in which the wavefield is given by the following propagation scheme

$$P(\mathbf{x},t+\Delta t) = -P(\mathbf{x},t-\Delta t) + 2\left[\sum_{k=0}^{M} c_{2k} J_{2k}(\Delta t R) Q_{2k}\left(\frac{iL}{R}\right)\right] P(\mathbf{x},t), \tag{1.17}$$

where $L = v(\mathbf{x})\sqrt{-\nabla^2}$, $c_0 = 1$ and $c_k = 2$ if $k \neq 0$. J_{2k} represents the Bessel function of order $2k$, Q_{2k} are modified Chebyshev polynomials, and R is a scalar larger than the range of the eigenvalues of L. The REM provides a solution with very high degree of accuracy and can be reduced to various finite-difference time-derivative schemes (Pestana and Stoffa, 2010).

In Appendix A, we show that starting from equation 1.16 the time derivative of the pressure wavefield can be obtained. Taking into account that the only time-dependent term in the expansion of equation 1.17 is the Bessel function, we can obtain the first time derivative of the wavefield in the following form

$$\dot{P}(\mathbf{x},t+\Delta t) = \dot{P}(\mathbf{x},t-\Delta t) + 2\left[\sum_{k=0}^{M} c_{2k} R \frac{d}{d\tau}\left[J_{2k}(\tau = \Delta t R)\right] Q_{2k}\left(\frac{iL}{R}\right)\right] P(\mathbf{x},t), \tag{1.18}$$

where the derivate of the Bessel function J'_n can be calculated using the relation $J'_n(\Delta t R) = -J_{n+1}(\Delta t R) + \frac{n}{\Delta t R} J_n(\Delta t R)$ (Abramowitz and Stegun, 1972). Using the REM solution, we can compute the wavefield for each time step, as well as its first-order time derivative. Next, using equation 1.15 we compute the Hilbert transform wavefield for both source and receivers and get the analytical wavefields for each time step, which are needed for wavefield separation and application of the causal imaging condition.

In summary, in our implementation we are proposing to use the REM to obtain the real part of the wavefield through equation 1.17. Inside the time step loop, the imaginary part of analytical wavefield is computed based on equations 1.15 and 1.18. The pseudocode for the proposed analytical wavefield calculation method, for every marching time step, is given in Algorithm 1. An important aspect to mention is that the operator $1/\sqrt{k_x^2 + k_z^2}$ must be applied in the Fourier domain, since its application is not possible through finite-difference schemes. The computation of double (2D) or triple (3D) forward and backward FFTs may represent an extra cost. However, this cost is not comparable with the execution of an additional extrapolation to compute the wavefield associated with the Hilbert transform of the source pulse, which is considerably more costly. After application the proposed method, we can separate the wavefields into its down- and upgoing components for source and receiver wavefields using equations 1.12 and 1.13. Thus, we need to solve the wave equation only once, improving the computational efficiency of the wavefield separation procedure. This allows us to apply the causal imaging condition for RTM at a reasonable computational cost.

Numerical tests

In this section, we test our proposed method to calculate the imaginary part of the analytical wavefield and display a comparison between the explicit wavefield decomposition obtained by the conventional method (two propagations) and the proposed scheme. In all of the performed tests, the rapid expansion method was selected as method to perform seismic modeling. Additionally, we analyze the RTM images obtained using the mentioned wavefield decomposition imaging.

We use a 2D synthetic four-layer isotropic model (Figure 1.3) to compare the conventional wavefield separation and the procedure proposed in this work. The 2D model consists of 315 × 195 grid nodes with 10 m of grid spacing. The velocities of the different layers in a descending order are 2000 m/s, 3000 m/s, 4000 m/s, and 2000 m/s, respectively. The interface between the top two layers is a flat surface, the following interface presents a wavy structure, and the deepest interface is a flat surface with two discontinuities. To test the separation procedure, we inject a Ricker pulse with a 50 Hz cut-off frequency, located at position $x = 1570\,\mathrm{m}$ and $z = 10\,\mathrm{m}$ with a time sampling of 1 ms. All the snapshots for this model show the wavefield at $t = 0.81\,\mathrm{s}$. For comparison, we show the real and the imaginary parts of the analytical wavefield (Figures 1.4a and 1.4c) and also the up- (reflected waves - Figure 1.4e) and downgoing components (transmitted waves - Figure 1.4g), which were obtained through the propagation of both the source and Hilbert transformed source (two propagations). Applying the proposed method, just a single propagation by REM, we compute the real wavefield and its Hilbert transform by equation 1.15, resulting in the analytical wavefield. The real and imaginary parts (Figures 1.4b and 1.4d) and the up- and downgoing components, Figures 1.4f and 1.4h, respectively, are shown on the right part of the Figure 1.4.

From the results presented in Figure 1.4, we notice that the images are similar in quality, proving that the results obtained for both procedures are equivalent and the images are free of dispersion noise. Moreover, with these results we demonstrate that the analytical wavefield can be computed by solving the wave equation using as a wavelet a real source pulse. A comparison of the seismic traces acquired at $x = 1570\,\mathrm{m}$ is given in Figure 1.5, for both the conventional method (two propagations) and the proposed method (single propagation), showing that for the two methods used to calculate the analytical wavefield the phase and the amplitude of the pulses match quite well.

To validate the effectiveness of the proposed method in the 3D case, we test the acoustic wavefield simulation of up- and downgoing wavefields on a simple three-layer model. The synthetic model has 210 mesh points with a uniform spacing of 10 m in each direction. The velocity parameters from the top to the bottom layer are 1500 m/s, 2000 m/s, and 2500 m/s, respectively. A Ricker wavelet with a maximum frequency of 50 Hz and a time sampling of 2 ms is used as a source wavelet; the source is placed at the center of the model. The analytical wavefield is constructed and equations 1.12 and 1.13 are applied to separate the up- and downgoing components. Since for both procedures, two propagations and single propagation, the real part of the analytic wavefield is obtained by the REM, the expected snapshots will be similar, as shown in Figure 1.6a and 1.7a. Figure 1.6b presents the imaginary wavefield snapshot at 0.47 s using the Hilbert transform of the wavelet as the source - conventional method - and Figures 1.6c and 1.6d are the up- and downgoing components, respectively. Figure 1.7 displays the real and imaginary parts of the analytical wavefield, and the decomposed unidirectional wavefields for the three-layer model at 0.47 s obtained by a single extrapolation in time. From the comparison between Figures 1.6 and 1.7 we can notice that the imaginary part constructed by the proposed method is very similar to the one obtained through the propagation of the Hilbert transform of the source, preserving the amplitude and phase of the wavefield. Additionally, it can be observed that the explicit wavefield separation is performed as expected, therefore the forward-modeling approach for up- and downgoing components is still effective for the 3D case and can be used in the migration process to generate the decomposed images.

The first example for RTM presents the decomposed image generated with the unidirectional components of the source and receiver wavefields - equation 1.4. For this numerical example, we generate a 2D split-spread synthetic dataset for the overthrust velocity model (Aminzadeh et al., 1997) shown in Figure 1.8a, which includes complex structures and thin layers. The grid spacings in the x- and z-directions are 25 m. 265 sources are excited one by one on the surface of the model from $x = 125$ to 20 000 m with a horizontal spacing of 75 m. The length of each shot record is 4 s with a time step of 1 ms and a maximum frequency of 30 Hz. A fixed array of 361 receivers is located along the model surface with receiver spacing of 25 m and 4500 m of maximum offset. In Figure 1.8b, we have the result obtained by the crosscorrelation of the source and receiver wavefields, which is the conventional RTM result employing equation 1.1. This image is contaminated by large-amplitude noise, which completely masks the signals. Figure 1.8d shows the result related to the last two terms of equation 1.4 (wavefields propagating in the same direction) and it is completely contaminated by the low-frequency noise. The RTM result generated by the causal imaging condition (first part of equation 1.4), is presented in Figure 1.8c. In this image, the artifacts produced by the conventional RTM, including the low-frequency noise, are removed, and we can see a noticeable improvement in image quality in comparison with the result shown in Figure 1.8b.

The second numerical test to compute the seismic migration images is carried on the four-layers velocity model (Figure 1.3). In this example, we compare the RTM result using the conventional migration and the de-primary RTM - analytical wavefield constructed by making two propagations, or by the proposed scheme (Algorithm 1). We generate a synthetic 2D split-spread dataset using an acoustic simulation that consists of 315 shot gathers evenly distributed across a horizontal distance of 3140 m and maximum offset of 1000 m. Figure 1.9a is the result of the conventional imaging condition, which is contaminated throughout with a very low-frequency noise. Figure 1.9b shows the RTM result obtained by the conventional correlation imaging condition followed by application of the Laplacian filter (Youn and Zhou, 2001); the RTM results using the causal imaging condition are shown in Figures 1.9c and 1.9d. In the result with the conventional imaging condition, we can see imaging artifacts caused by the internal multiples (marked by the white rectangle), mainly on top of the first reflector. Figures 1.9c and 1.9d are results obtained applying the causal imaging condition, where the analytical wavefield was calculated using two-propagations and single propagation algorithms, respectively. We should notice that these results have a better quality compared to Figure 1.9b and that the artifacts above the first interface are removed because the S_d component is zero in this region. In order to analyze the spectral content of the results presented in Figure 1.9, we generate their 2D spectrum (Figure 1.10). Figure 1.10b shows the strong attenuation of the low-frequency components close to the origin ($k_x = k_z = 0$). Comparing the spectral plots of the RTM result with the Laplacian filtering and the RTM result with the de-primary image condition (Figures 1.10c and 1.10d), we can see that the spectrum of the RTM result is well preserved and shows less attenuation around the region $k_x = 0$ and $k_z = 0$. With these results, obtained using the RTM with causal imaging condition, we can confirm the effectiveness of the implemented algorithm to construct the imaginary part of the analytical wavefield and its employment to remove the low-frequency noise usually seen in a typical reverse time migration images.

In the last example, to make sure that our conclusions do not apply to a simple velocity model or a single data set only and to demonstrate the applicability of the proposed method, we also apply the RTM with the causal imaging condition for the dataset of the fault velocity model shown in Figure 1.11. In order to improve the migration result, we have included the source illumination compensation in the conventional and the de-primary imaging conditions (Kaelin and Guitton, 2006). The fault model is characterized by several faults, as well as a complicated base, with the presence of intrusions. The numerical discretization contains 600×265 samples, with spacing of 20 m in both directions. This is a high-quality dataset generated with REM modeling with shot spacing of 40 m, receiver spacing of 20 m, and 2560 m maximum offset. In the migration, the highest frequency is 50 Hz and the time step is $\Delta t = 4\,\mathrm{ms}$. Figure 1.11 displays the comparison of the migration results obtained by the crosscorrelation imaging condition (Figure 1.11b) and the causal imaging condition with source illumination using the two-propagations method and the procedure that we are proposing in the present work (Figure 1.11d). For such a dataset, the results show that our method can handle complex velocities fairly well and shows a good delineation of the faults, specially at the main fault, as well as the domes and the horizontal plane at the bottom. Theses results confirm the successful application of the single propagation method on RTM, in which the REM is used for forward and backward propagations, combined with the analytical wavefield computation, allowing wavefield separation and further application of the causal imaging condition. In short, it shows the effectiveness of the implemented algorithm in removing the low-frequency noise produced by the crosscorrelation imaging condition.

The correct separation of the wavefield in different tests shows that the proposed scheme to build the analytical wavefield works well, and the successful applications of de-primary RTM to three different datasets confirm that the causal imaging condition is effective to remove the low-frequency noise usually seen in the conventional RTM. Unlike the methods that involve complex traces, where the cost of seismic modeling is doubled as a complex wavefield is extrapolated, the construction of the imaginary wavefield part involves a 2D FFT and IFFT in each time step, which can be further speed up using faster FFT methods. The proposed method separates the up- and downgoing components directly in the wavefield propagation and avoids the high disk space cost; in addition, the process of up- and downgoing separation requires two 1D FFTs per trace. Figure 1.12 shows the normalized times consumed only for the explicit wavefield separation applied to a single shot of each of the various datasets used; in general, we can see that our scheme represents around a 20.2 % increase in computational time. The migrated time consumed by each method is presented in Figure 1.13 for the overthrust model, four-layer model, and the fault model datasets. It is observed that the time consumed by the present method - single propagation - is lower than the time consumed by the conventional method used in the calculation of the analytical wavefield, and a little higher than the conventional RTM with crosscorrelation imaging condition. Therefore, the proposed method can make use of the causal imaging condition for RTM at a lower computational cost and still provide similar results when compared to RTM using two propagations. This improvement to obtain the unidirectional wavefield components can be used in the calculation of the gradient in full-waveform adjoint inversion (FWI), since it has a similar crosscorrelation form as the imaging condition of RTM; then the FWI gradient can be decomposed with the same procedure into its reflection components (migration term) and the transmission component (tomographic term), just as it is shown in Rocha et al. (2016). However, the up-up and down-down parts of equation 1.4, which are considered noise in migration, are more valuable in FWI because they can be used to invert for the low-frequency components of the model parameters (Wang et al., 2016a).

Conclusion

Reverse time migration can image steeply dipping reflectors and complicated velocity models. However, this also causes the conventional correlation-based imaging condition to produce large amplitude, low-frequency noises that contaminate the migrated image. Decomposing the extrapolated wavefields and applying the de-primary imaging condition successfully removes these artifacts from the images. The causal imaging condition needs an up- and down-separation algorithm, which can be achieved by using analytical wavefield extrapolation and is much cheaper than separation methods via Fourier transforms over time since the latter requires saving the wavefield at all time steps. We present an efficient forward-modeling approach to compute the analytical wavefield based on the rapid expansion method in a stable way and free of dispersion noise. In our proposed method the source wavefield is extrapolated in time and for each time step we can compute the first-order time derivative and then the Hilbert transform of the wavefield. Based on the analytical wavefield the up- and downgoing components in a 2D or 3D acoustic wavefield simulation are generated. We tested the proposed scheme on a four-layer model and demonstrated that we can compute the analytical wavefield using just a single propagation, with the same quality of the common procedure which needs to apply two propagations. The numerical tests on different models demonstrate that the method is effective, avoiding the expensive storage requirement and only increasing the computation cost by 20.2 % for the separation part. Using our method to compute the analytical wavefield and explicitly separate the wavefield into up- and downgoing components, we could employ the causal imaging condition for RTM at a computation cost just a little higher than the conventional crosscorrelation imaging condition. We applied the de-primary image condition on different velocity models and saw that the RTM with the causal imaging condition can effectively remove the undesired low-frequency noise produced by the conventional crosscorrelation imaging condition. The proposed numerical scheme for wavefield decomposition significantly improves the efficiency of the de-primary imaging condition and increases the computational cost by approximately 27 % when compared with the conventional crosscorrelation imaging condition.

Acknowledgements

We are thankful to the associate editor D. Draganov and three anonymous reviewers for the effort put into the review and for the numerous valuable comments that helped to improve this manuscript. R. C. Pestana thanks CNPq for the financial support through the Instituto Nacional de Ciências e Tecnologia em Geofísica do Petróleo (INCT-GP). D. E. Revelo thanks the Coordenação de Aperfeiçoamento de Pessoal de Nível Superior – Brasil (CAPES) – Finance Code 001. Finally, we would like to acknowledge the project PIE00005/2016 of the FAPESB 003/2015 and the CPGG/UFBA, where this research was carried out.

Appendix

Derivation of the first time derivative of the wavefield by REM

Here, we present how we can compute the first time derivative of the wavefield directly from the solution of the acoustic wave equation obtained by the rapid expansion method (REM). We consider the two-dimensional (2D) acoustic medium with constant density, and a varying velocity in both vertical and horizontal directions. The wave equation, in the form of equation 1.16, is given by

$$\frac{\partial^2 P(\mathbf{x},t)}{\partial t^2} = -L^2 P(\mathbf{x},t).$$

Now, considering the following initial conditions

$$P(\mathbf{x},t=0) = P_0 \qquad \text{and} \qquad \left.\frac{\partial P(\mathbf{x},t)}{\partial t}\right|_{t=0} = \dot{P}_0 \tag{1.19}$$

the formal solution is

$$P(\mathbf{x},t) = \cos(L\,t)\,P_0 + \frac{1}{L}\sin(L\,t)\,\dot{P}_0, \tag{1.20}$$

where the dot denotes a time derivative. Using equation 1.20, the first time derivative of $P(\mathbf{x},t)$ is

$$\dot{P}(\mathbf{x},t) = -L\sin(L\,t)\,P_0 + \cos(L\,t)\,\dot{P}_0. \tag{1.21}$$

In addition, we calculate $\dot{P}(\mathbf{x},t)$ at time $-t$, i.e.,

$$\dot{P}(\mathbf{x},-t) = L\sin(L\,t)\,P_0 + \cos(L\,t)\,\dot{P}_0. \tag{1.22}$$

To eliminate the time derivative initial condition ($\dot{P}_0$), we subtract equation 1.22 from equation 1.21 and solve for $\dot{P}(\mathbf{x},t)$, obtaining

$$\dot{P}(\mathbf{x},t) = \dot{P}(\mathbf{x},-t) - 2L\sin(L\,t)\,P_0. \tag{1.23}$$

This scheme allows extrapolation of the field $\dot{P}(\mathbf{x},t)$ from the fields $\dot{P}(\mathbf{x},-t)$ and P_0.

Now, consider that the sine function can also be expressed as follows

$$\sin(L\,t) = -\frac{d}{dt}\left[\frac{1}{L}\cos(L\,t)\right]. \tag{1.24}$$

Following Kosloff et al. (1989) and using the expansion method presented by Tal-Ezer et al. (1987), the cosine function is expanded (equation 1.17) as

$$\cos(L\,t) = \sum_{k=0}^{M} c_{2k} J_{2k}(R\,t) Q_{2k}\left(\frac{iL}{R}\right). \tag{1.25}$$

Substituting equation 1.25 in equation 1.24 and taking into account that the only time-dependent term in this expansion is the Bessel function, we have that

$$\begin{aligned}\sin(L\,t) &= -\frac{d}{dt}\left[\frac{1}{L}\sum_{k=0}^{M} c_{2k} J_{2k}(R\,t) Q_{2k}\left(\frac{iL}{R}\right)\right] \\ &= -\frac{1}{L}\sum_{k=0}^{M} c_{2k} R \frac{d}{d\tau}\left[J_{2k}(\tau = R\,t)\right] Q_{2k}\left(\frac{iL}{R}\right).\end{aligned} \tag{1.26}$$

Therefore, in order to obtain an extrapolation scheme for a single time step, we replace the time t by the time step Δt in equations 1.23 and 1.26 and the initial wavefield (P_0) in equation 1.23 by some arbitrary reference time t, which results in

$$\dot{P}(\mathbf{x}, t+\Delta t) = \dot{P}(\mathbf{x}, t-\Delta t) + 2\left[\sum_{k=0}^{M} c_{2k} R \frac{d}{d\tau}\left[J_{2k}(\tau = \Delta t R)\right] Q_{2k}\left(\frac{iL}{R}\right)\right] P(\mathbf{x}, t). \quad (1.27)$$

Thus, the final result presented in equation 1.27 can be used to compute the first time derivative of the wavefield for each time step by the REM, which is the expression presented by Tessmer (2011).

Algorithm 1 Proposed algorithm to calculate the analytical wavefield

```
Read: $\Delta x$, $\Delta z$, $\Delta t$, $f_{\max}$, $v(x,z)$        ▷ parameters
Calculate: $R$, $M$
Initialize $P^{t+\Delta t} = 0$ and $Q^{t+\Delta t} = 0$
for each time step
$P_0 \leftarrow P^t$        ▷ for $n = 0$
$P_{aux}^{t+\Delta t} \leftarrow J_0(\Delta t R) P_0$
$Q_{aux}^{t+\Delta t} \leftarrow R * [-J_1(\Delta t R) + J_0(\Delta t R)] P_0$
$P_1 \leftarrow \frac{2v^2}{R^2} \mathrm{DFT}^{-1} \left\{ [-k_x^2 - k_z^2] \, \mathrm{DFT}[P_0] \right\}$        ▷ for $n = 1$
$P_{aux}^{t+\Delta t} \leftarrow P_{aux}^{t+\Delta t} + 2J_2(\Delta t R) P_1$
$Q_{aux}^{t+\Delta t} \leftarrow Q_{aux}^{t+\Delta t} + 2R * [-J_3(\Delta t R) + \frac{2}{\Delta t R} J_2(\Delta t R)] P_1$
for $n \leftarrow 1, M$ do
    $P_{n+1} \leftarrow 2P_n + \frac{4v^2}{R^2} \mathrm{DFT}^{-1} \left\{ [-k_x^2 - k_z^2] \, \mathrm{DFT}[P_n] \right\} - P_{n-1}$
    $P_{aux}^{t+\Delta t} \leftarrow P_{aux}^{t+\Delta t} + 2J_{2n+2}(\Delta t R) P_{n+1}$
    $Q_{aux}^{t+\Delta t} \leftarrow Q_{aux}^{t+\Delta t} + 2R * [-J_{2n-1}(\Delta t R) + \frac{2n}{\Delta t R} J_{2n}(\Delta t R)] P_{n+1}$
end for
$P^{t+\Delta t} \leftarrow -P^{t-\Delta t} + 2P_{aux}^{t+\Delta t}$        ▷ Real wavefield
$Q^{t+\Delta t} \leftarrow Q^{t-\Delta t} + 2Q_{aux}^{t+\Delta t}$
$Q^{t+\Delta t} \leftarrow \frac{1}{v} \mathrm{DFT}^{-1} \left\{ \frac{1}{\sqrt{k_x^2 + k_z^2}} \, \mathrm{DFT}\left[ Q^{t+\Delta t} \right] \right\}$        ▷ Imaginary wavefield
```

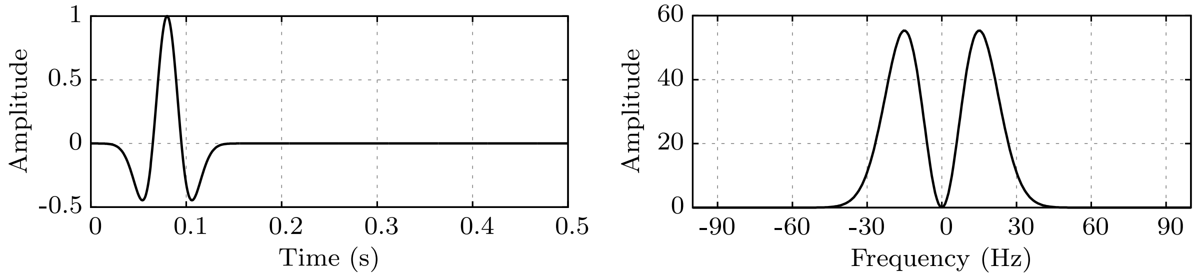

(a) Real trace

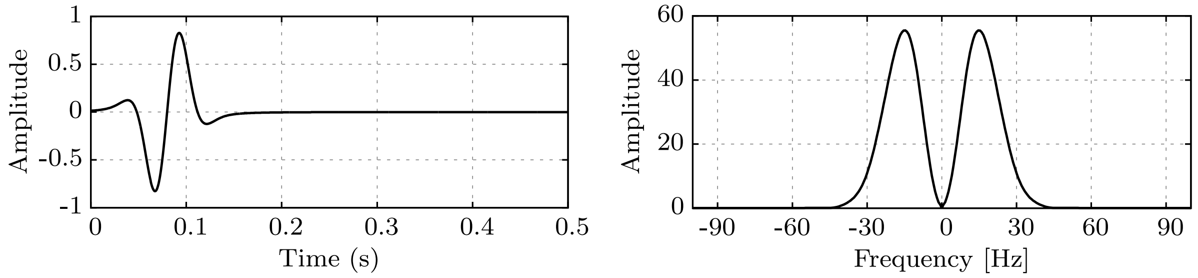

(b) Trace after Hilbert transform

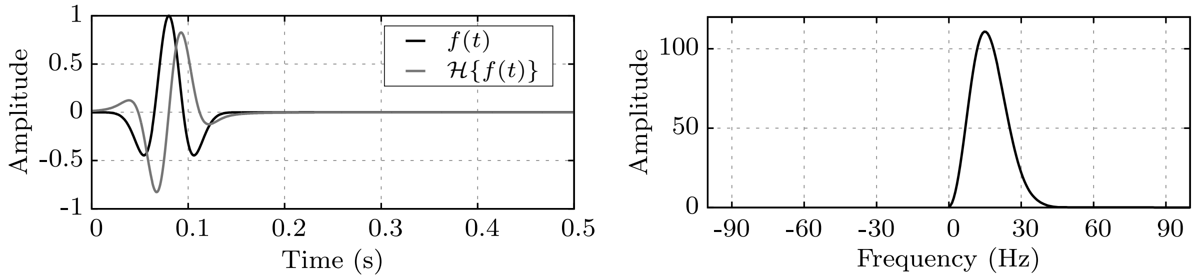

(c) Analytical trace

Figure 1.1: The input trace and its frequency spectra for (a) a real trace (a Ricker wavelet), (b) the Hilbert transform of (a), and (c) the analytical trace constructed using equation 1.9 - (a) as the real part and (b) as the imaginary part. Notice that (a) and (b) have the same symmetric amplitude spectra, but in (c) the amplitude spectrum at negative frequencies is zero, and the amplitudes of the positive frequencies are scaled by two - doubled when compared with (a) and (b).

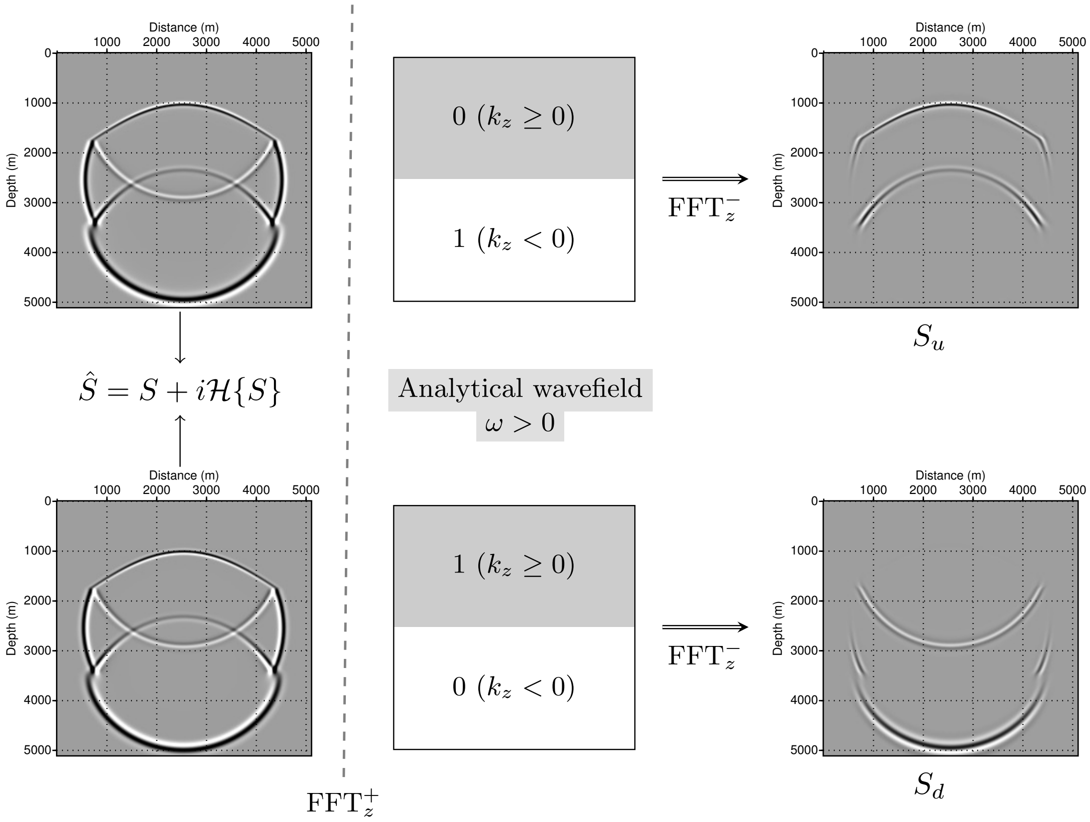

Figure 1.2: Process flowchart to obtain up- (S_u) and downgoing (S_d) components using the analytical wavefield. For every marching time step, the source analytical wavefield ($\hat{S}$) is constructed by the real wavefield and its Hilbert transform. Then, a direct Fourier transform is applied to the z-axis (FFT$_z^+$); the filter given in equations 1.10 and 1.11 is applied to obtain the unidirectional components, and, finally, an inverse Fourier transform (FFT$_z^-$) is applied to return to the spatial domain.

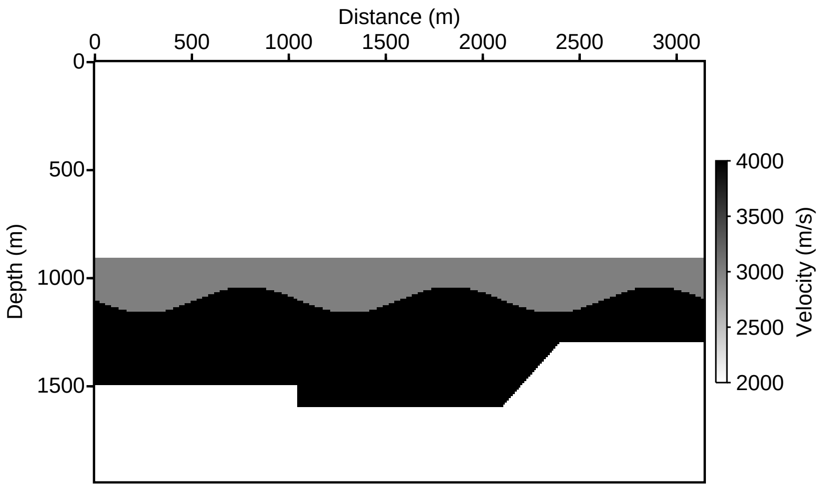

Figure 1.3: Four-layer velocity model used for numerical experiments.

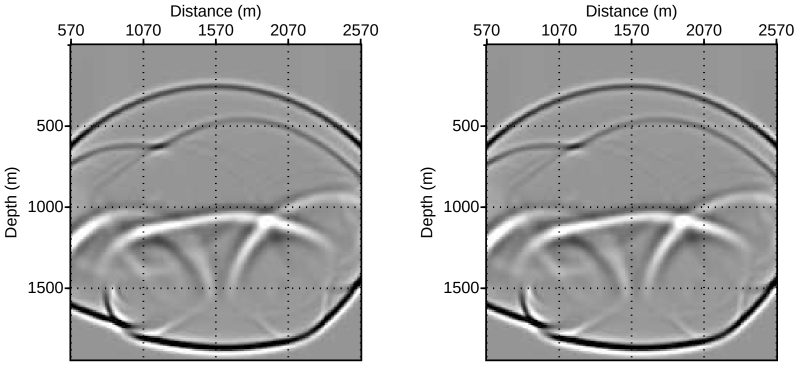

(a) Real part (b) Real part

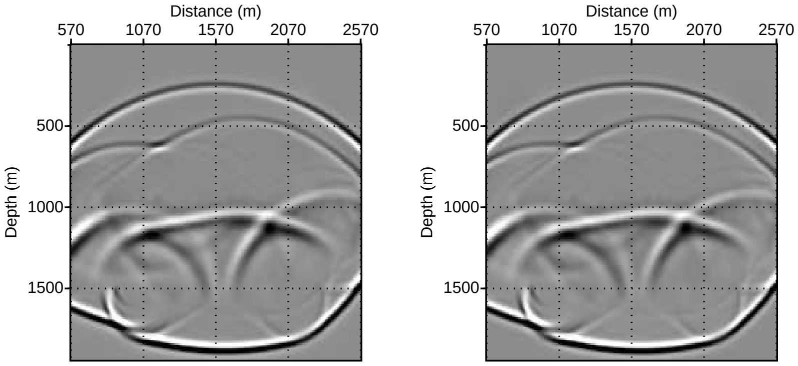

(c) Imaginary part (d) Imaginary part

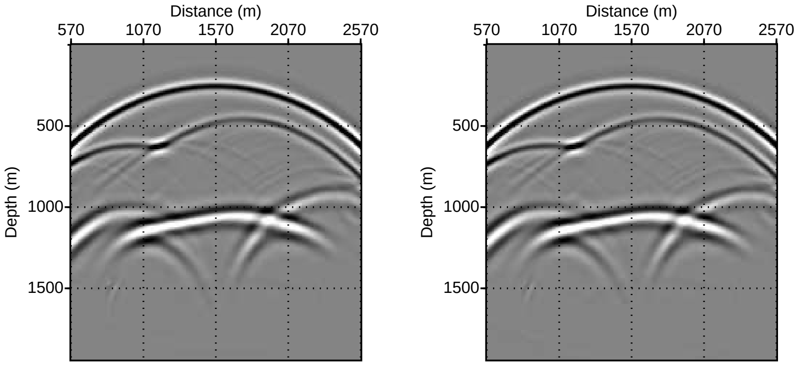

(e) Upgoing component (f) Upgoing component

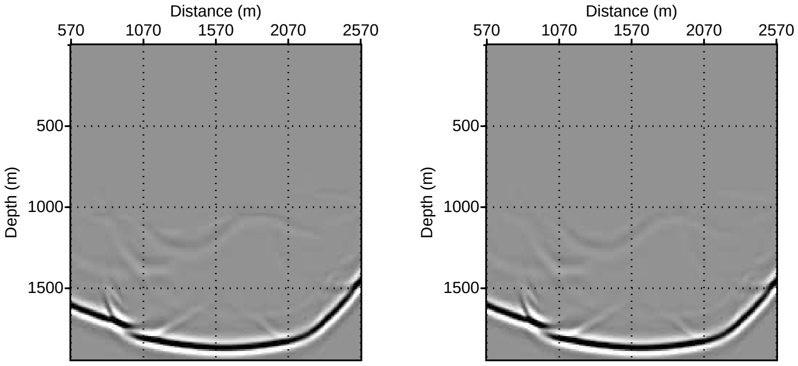

(g) Downgoing component (h) Downgoing component

Figure 1.4: Snapshots for the source wavefield at $t = 0.81\,\mathrm{s}$ for the real and imaginary parts and for the up- and downgoing wavefields. The figures on the left were obtained using a source and the Hilbert transformed source - two propagations. The figures on the right were obtained using equations 1.15 and 1.18 - using only a single propagation.

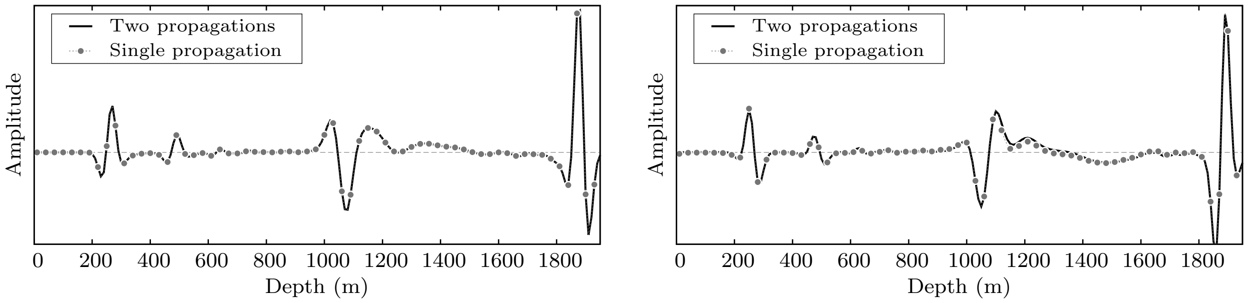

(a) Real part

(b) Imaginary part

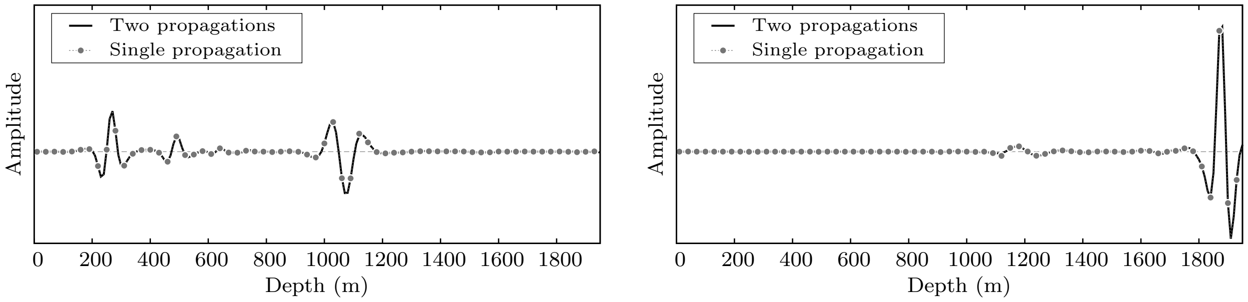

(c) Upgoing component

(d) Downgoing component

Figure 1.5: Comparison in wiggle format of the seismic traces at $x = 1570\,\text{m}$ (Figure 1.4) using the conventional method (two propagations) and the proposed method to calculate the analytical wavefield for the four-layer model (Figure 1.3).

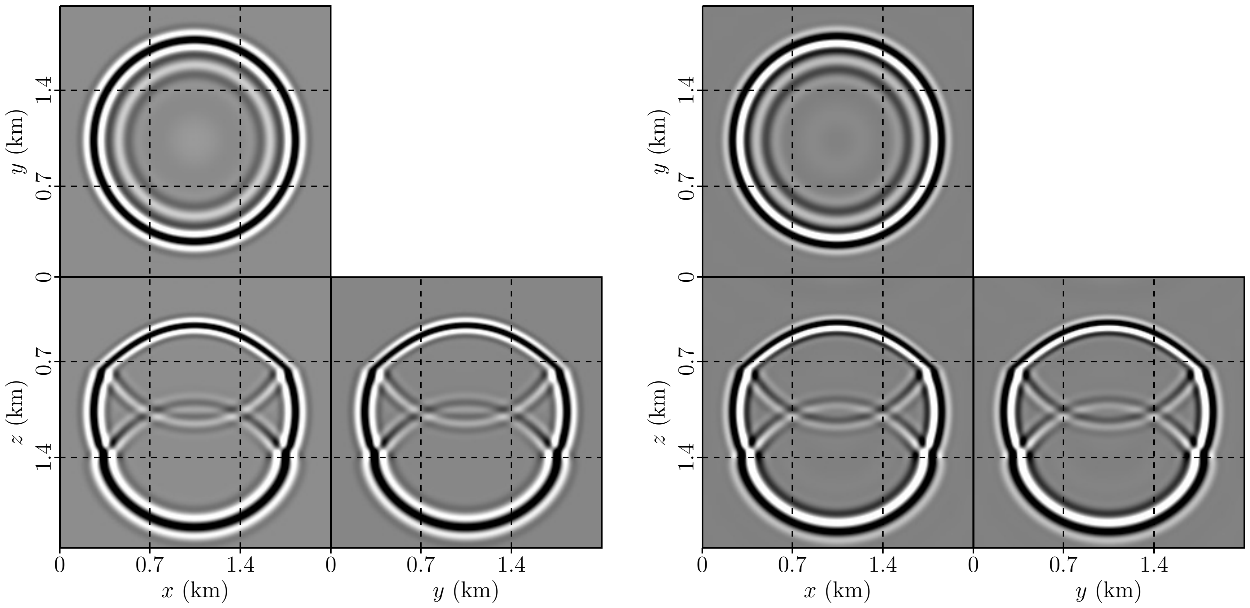

(a) Real part (b) Imaginary part

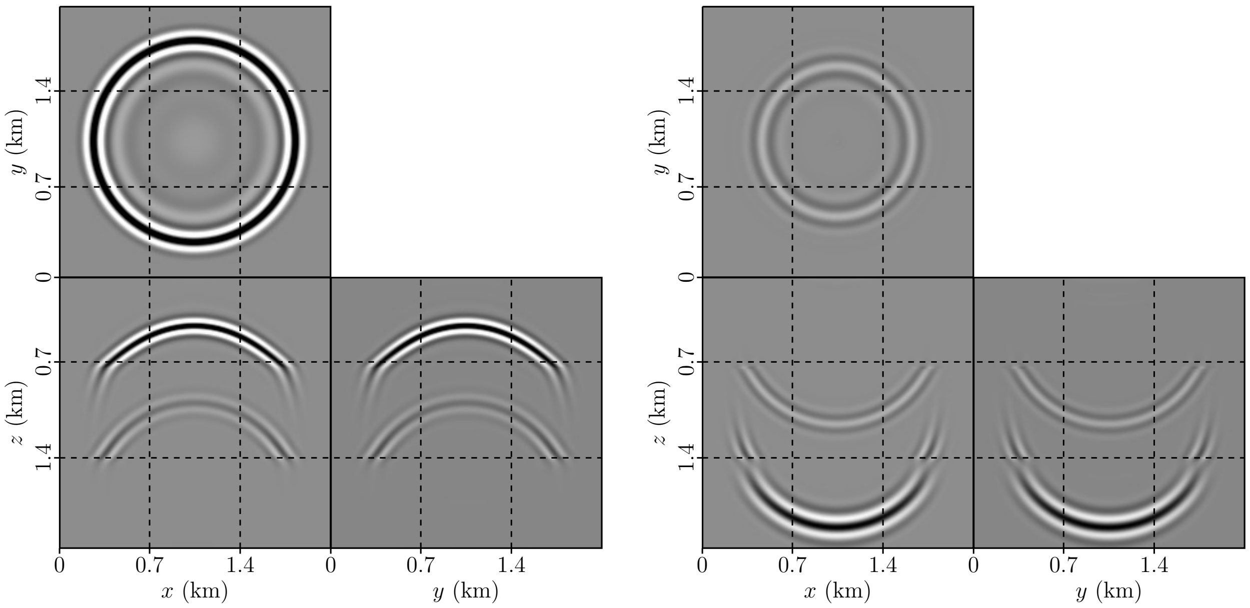

(c) Upgoing component (d) Downgoing component

Figure 1.6: The snapshots obtained through the conventional method for the three-layer model at 0.47 s: (a) real wavefield, (b) imaginary wavefield, (c) upgoing component, and (d) downgoing component.

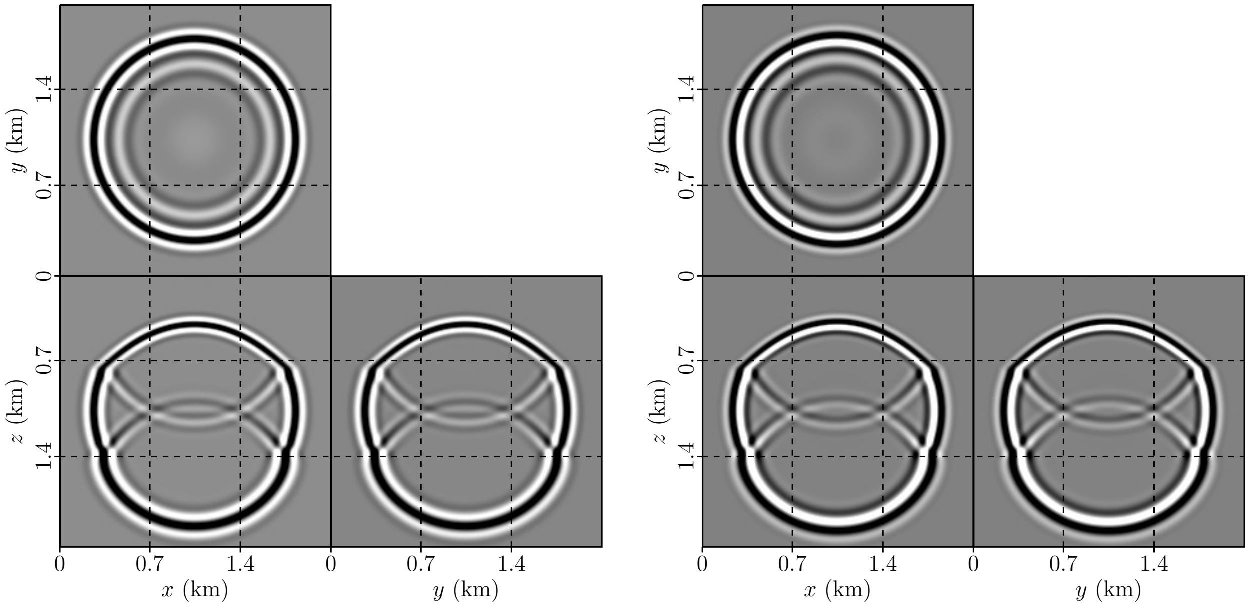

(a) Real part

(b) Imaginary part

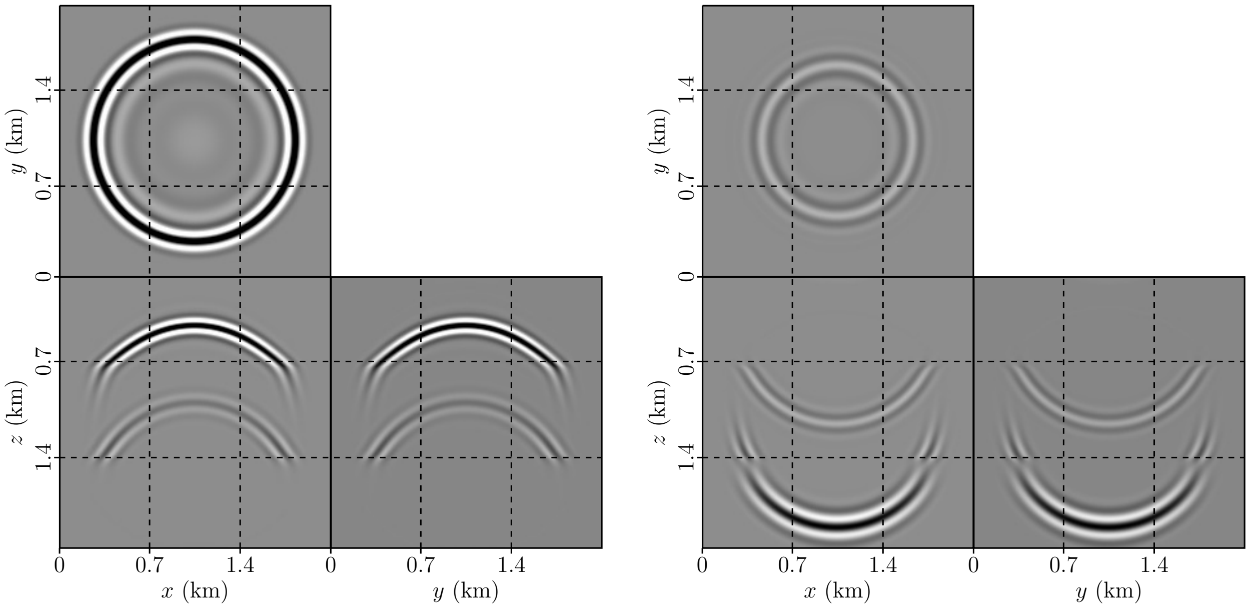

(c) Upgoing component

(d) Downgoing component

Figure 1.7: The snapshots obtained through the proposed method for the three-layer model at 0.47 s: (a) real wavefield, (b) imaginary wavefield, (c) upgoing component, and (d) downgoing component. As shown in this image, the imaginary wavefield presents a correct form and the unidirectional components are well-separated.

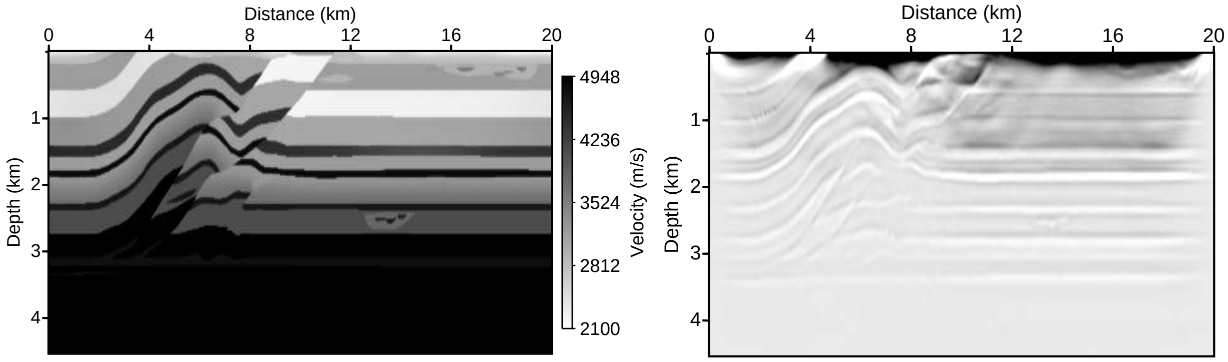

(a) Overthrust velocity model (b) $S(\mathbf{x},t)\,R(\mathbf{x},t)$

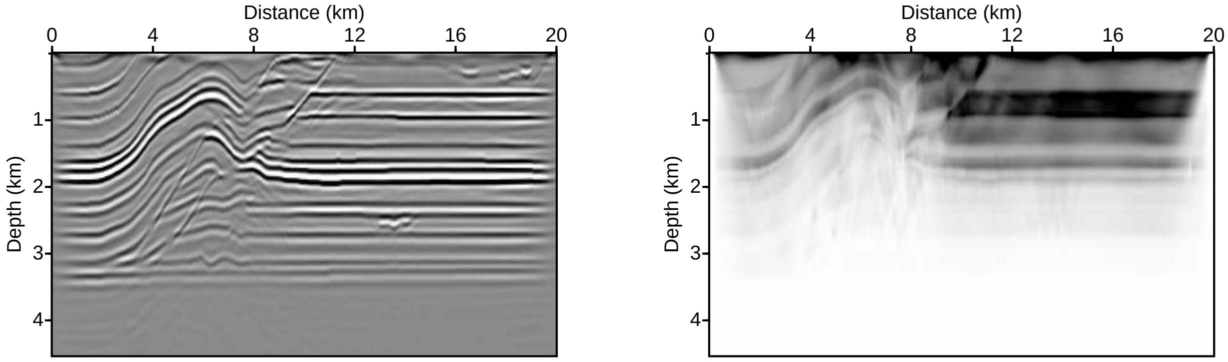

(c) $S_d(\mathbf{x},t)\,R_u(\mathbf{x},t)$ (d) $S_u(\mathbf{x},t)\,R_u(\mathbf{x},t) + S_d(\mathbf{x},t)\,R_d(\mathbf{x},t)$

Figure 1.8: (a) Velocity model used in the overthrust RTM experiment. Results of the RTM method using the (b) conventional crosscorrelation, (c) causal imaging condition (the first term of equation 1.4), and (d) correlation between the wavefields that propagate in the same direction (the latter two terms in equation 1.4), which generates low-frequency noise.

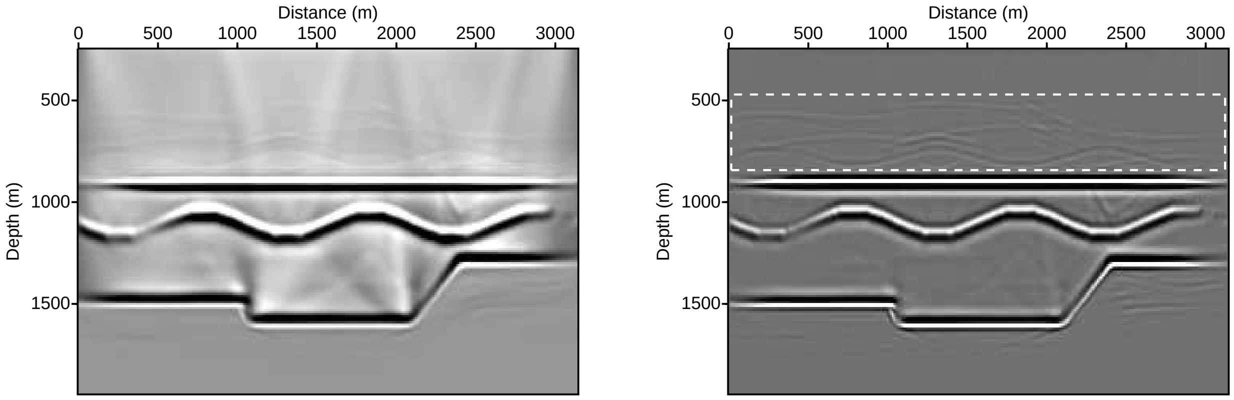

(a) Conventional crosscorrelation imaging (b) Crosscorrelation with Laplacian filter

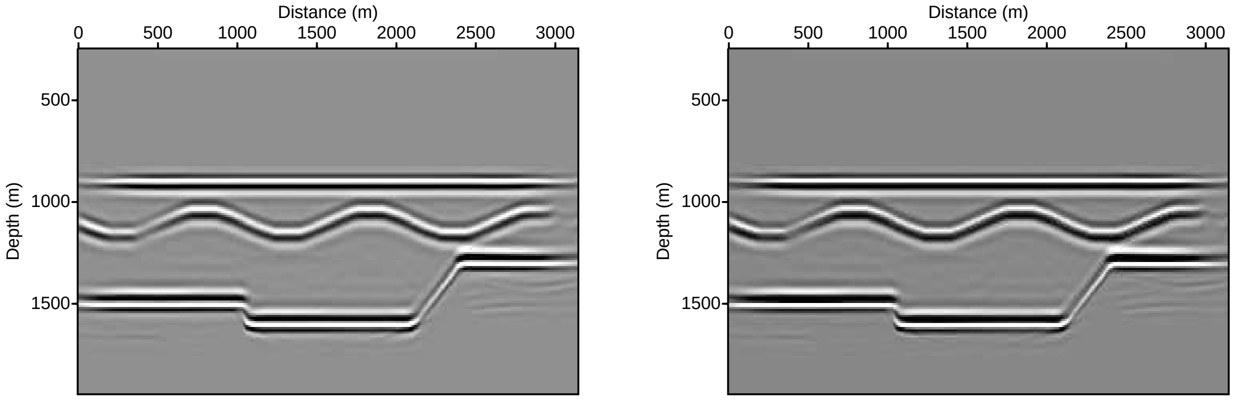

(c) Causal imaging condition - two propagations (d) Causal imaging condition - single propagation

Figure 1.9: The RTM results. The image is obtained by applying (a) the conventional crosscorrelation imaging condition, (b) band-pass filtered result of the image in (a), (c) and (d) by the causal imaging condition. Panel (b) contains the correct image and migration artifacts indicated by the white rectangle. Comparing (b) with the result of the de-primary result (c) and (d); these last two have better quality and no artifacts.

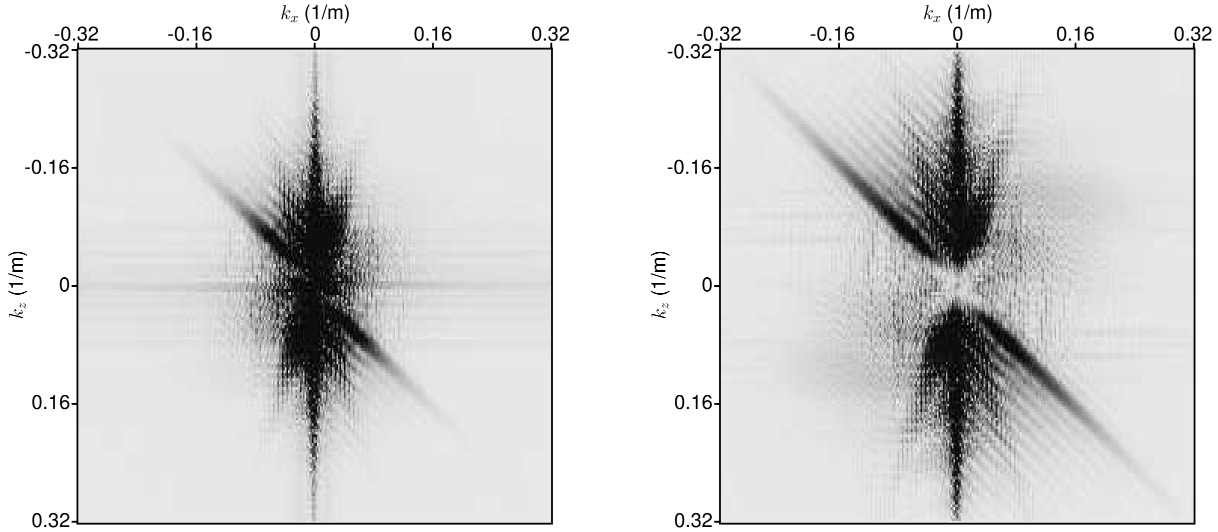

(a) Conventional crosscorrelation imaging

(b) Crosscorrelation with Laplacian filter

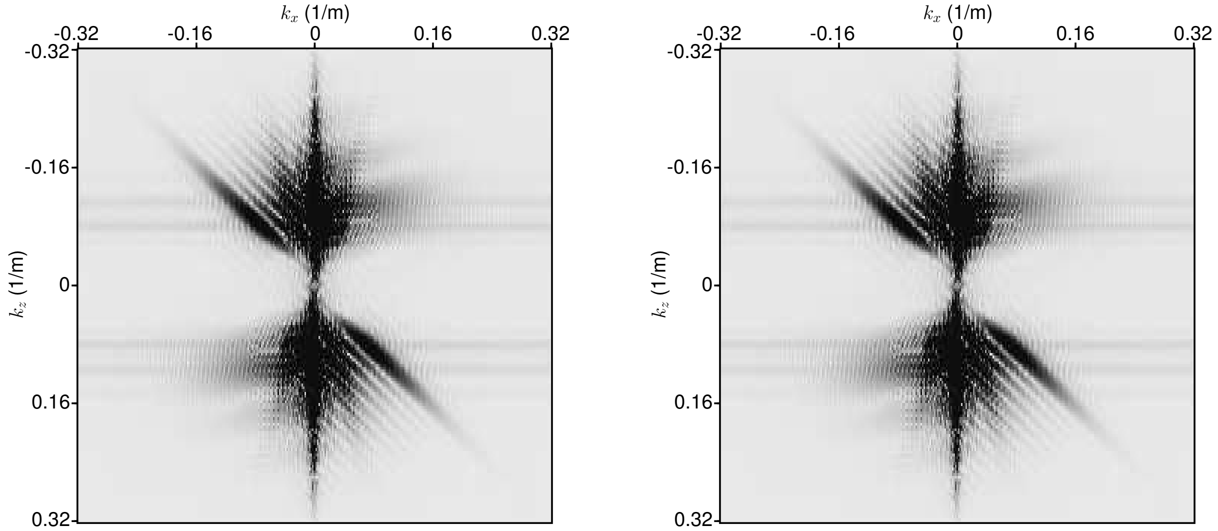

(c) Causal imaging condition - two propagations

(d) Causal imaging condition - single propagation

Figure 1.10: The 2D Fourier spectrum of the four-layer data set after the (a) conventional imaging condition, (b) conventional imaging condition plus Laplacian filter, and (c) and (d) causal imaging condition.

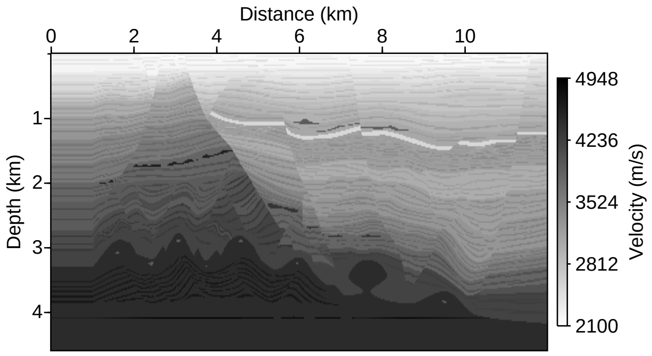

(a) Fault velocity model

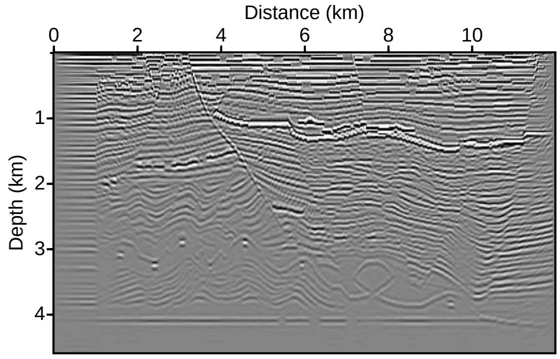

(b) Crosscorrelation with Laplacian filter

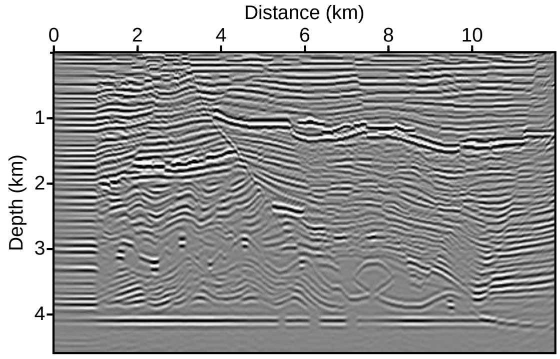

(c) Causal imaging condition - two propagations

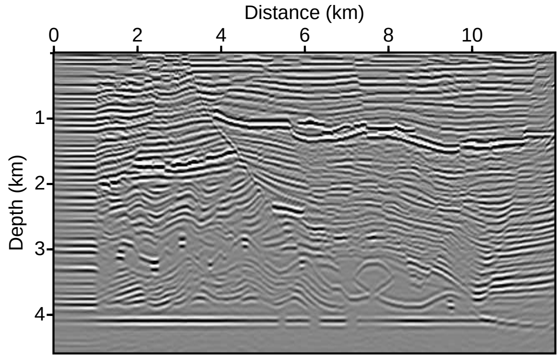

(d) Causal imaging condition - single propagation

Figure 1.11: The RTM results. (a) Migration velocity model. (b) Image obtained by applying the conventional crosscorrelation imaging condition. (c and d) Use a causal imaging condition and explicit wavefield separation, in which the former uses the two-propagations method and the latter uses the single propagation method.

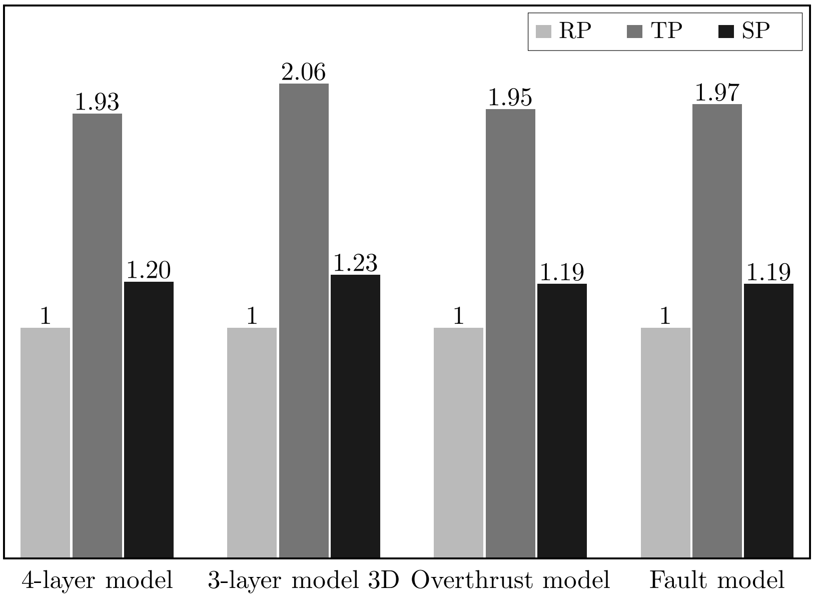

Figure 1.12: Normalized time consumed to perform the explicit wavefield separation using two propagations (TP) and the proposed method - single propagation (SP). RP represents the time consumed by the real wavefield propagation.

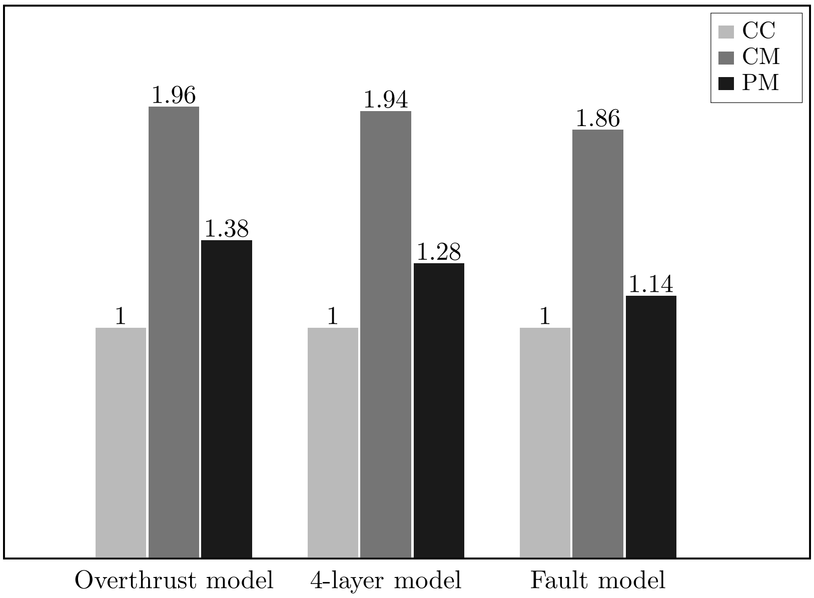

Figure 1.13: Total migration normalized time. CC, conventional crosscorrelation; CM, causal imaging condition; PM, causal imaging condition applying the proposed method.

References

Abramowitz, M. and Stegun, I. A. (1972) Handbook of mathematical functions with formulas, graphs, and mathematical tables, 9th Printing. New York: Dover.

Aminzadeh, F.; Brac, J. and Kunz, T. (1997) 3D Salt and Overthrust models, SEG/EAGE Modeling Series, No. 1:SEG.

Baysal, E.; Kosloff, D. D. and Sherwood, J. W. (1983) Reverse time migration, Geophysics, **48**:1514–1524.

Brandsberg-Dahl, S.; Chemingui, N.; Whitmore, D.; Crawley, S.; Klochikhina, E. and Valenciano, A. (2013) 3D RTM angle gathers using an inverse scattering imaging condition, 83th Annual Int. Meeting, SEG, Expanded Abstracts, pp. 3958–3962.

Claerbout, J. F. (1971) Toward a unified theory of reflector mapping, Geophysics, **36**:467–481.

Du, X.; Fowler, J. and Fletcher, P. (2014) Recursive integral time-extrapolation methods for waves: A comparative review, Geophysics, **79**:T9–T26.

Fei, T. W.; Luo, Y. and Qin, F. (2014) An endemic problem in reverse-time migration, 84th Annual Int. Meeting, SEG, Expanded Abstracts, pp. 3811–3815.

Fei, T. W.; Luo, Y.; Yang, J.; Liu, H. and Quin, F. (2015) Removing false images in reverse time migration: The concept of de-primary, Geophysics, **80**:S237–S244.

Fletcher, R. P.; Fowler, P. J.; Kitchenside, P. and Albertin, U. (2006) Suppressing unwanted internal reflections in prestack reverse-time migration, Geophysics, **71**:E79–E82.

Fomel, S.; Ying, L. and Song, X. (2013) Seismic wave extrapolation using low-rank symbol approximation, Geophysical Prospecting, **61**:526–536.

Gabor, D. (1946) Theory of communications, Journal of the Institution of Electrical Engineers, **93**:429–457.

Guitton, A.; Kaelin, B. and Biondi, B. (2007) Least-squares attenuation of reverse-time migration artifacts, Geophysics, **72**:S19–S23.

Hu, L. and McMechan, G. A. (1987) Wave-field transformations of vertical seismic profiles, Geophysics, **52**:307–321.

Kaelin, B. and Guitton, A. (2006) Imaging condition of reverse time migration, 76th Annual Int. Meeting, SEG, Expanded Abstracts, pp. 2594–2598.

Kosloff, D.; Filho, A. Q.; Tessmer, E. and Behle, A. (1989) Numerical solution of the acoustic and elastic wave equations by a new rapid expansion method, Geophysical Prospecting, **37**:383–394.

Liu, F.; Zhang, G.; Morton, S. and Leveille, J. (2011) An effective imaging condition for reverse-time migration using wavefield decomposition, Geophysics, **76**:S29–S39.

McMechan, G. A. (1983) Migration by extrapolation of time-dependent boundary values, Geophysical Prospecting, **31**:413–420.

Pestana, R. and Revelo, D. (2017) An improved method to calculate the analytical wavefield for causal imaging condition, 87th Annual Int. Meeting, SEG, Expanded Abstracts, pp. 4640–4644.

Pestana, R. and Stoffa, P. (2010) Time evolution of the wave equation using rapid expansion method, Geophysics, **75**:T121–T131.

Pestana, R.; dos Santos, A. W. G. and Araujo, E. S. (2014) RTM imaging condition using impedance sensitivity kernel combined with Poynting vector, 84th Annual Int. Meeting, SEG, Expanded Abstracts, pp. 3763–3768.

Revelo, D.; Pestana, R. and Gomez, L. (2016) Reverse time migration (RTM) using analytical wavefield and causal imaging condition, 78th Annual Intern. Conference and Exibition, EAGE, Extended Abstract, **Th P1 01**.

Revelo, D. E. and Pestana, R. C. (2016) One-step wave extrapolation matrix method for reverse time migration, Geophysics, **81**:S359–S366.

Rocha, D.; Tanushev, N. and Sava, P. (2016) Acoustic wavefield imaging using the energy norm, Geophysics, **81**:S151–S163.

Shen, P. and Albertin, U. (2015) Up-Down separation using Hilbert transformed source for causal imaging condition, 85th Annual Int. Meeting, SEG, Expanded Abstracts, pp. 4175–4179.

Stolk, C. C.; de Hoop, M. V. and Root, T. J. P. M. O. (2009) Inverse scattering of seismic data in the reverse time migration (RTM) approach, Proceedings of the Project Review, Geo-Mathematical Imaging Group of Purdue University, pp. 91–108.

Sun, J.; Fomel, S. and Ying, L. (2016) Low-rank one-step wave extrapolation for reverse time migration, Geophysics, **81**:S39–S54.

Tal-Ezer, H.; Kosloff, D. and Koren, Z. (1987) An accurate scheme for forward seismic modeling, Geophysical Prospecting, **35**:479–490.

Tessmer, E. (2011) Using the rapid expansion method for accurate time-stepping in modeling and reverse-time migration, Geophysics, **76**:S177–S185.

Ville, J. A. (1948) Theorie et application de la notion du signal analytique, Cables Transmission, **2**:61–74.

Wang, E. and Liu, Y. (2017) The hybrid absorbing boundary condition for one-step extrapolation and its application in wavefield decomposition-based reverse time migration, Journal of Geophysics and Engineering, **14**:1177–1188.

Wang, W.; McMechan, G. A.; Tang, C. and Xie, F. (2016a) Up/Down and P/S decompositions of elastic wavefields using complex seismic traces with applications to calculating poynting vectors and angle-domain common-image gathers from reverse time migrations, Geophysics, **81**:S181–S194.

Wang, W.; McMechan, G. A. and Xie, F. (2016b) Analysis of up/down decomposed acoustic reverse time migration images, Geophysics, **81**:S253–S259.

Wang, Y.; Zheng, Y.; Xue, Q.; Chang, X.; Fei, T. and Luo, Y. (2017) Reverse time migration of multiples: Reducing migration artifacts using the wavefield decomposition imaging condition, Geophysics, **82**:S307–S314.

Whitmore, N. D. and Crawley, S. (2012) Applications of RTM inverse scattering imaging conditions, 82th Annual Int. Meeting, SEG, Expanded Abstracts, pp. 1–6.

Yoon, K. and Marfurt, K. J. (2006) Reverse-time migration using the Poynting vector, Exploration Geophysics, **37**:102–107.

Youn, O. K. and Zhou, H. (2001) Depth imaging with multiples, Geophysics, **66**:246–255.

Zhang, Y. and Sun, J. (2009) Practical issues in reverse time migration: True amplitudes gathers, noise removal and harmonic-source encoding, First Break, **26**:24–25.

Zhang, Y. and Zhang, G. (2009) One-step extrapolation method for reverse time migration, Geophysics, **74**(4):A29–A33.

Zhang, Y.; Zhang, G.; Yingst, D. and Sun, J. (2007) Explicit marching method for reverse-time migration, 77th Annual Int. Meeting, SEG, Expanded Abstracts, pp. 2300–2304.

Zheng, Y.; Wang, Y. and Chang, X. (2018) 3D forward modeling of upgoing and downgoing wavefields using Hilbert transform, Geophysics, **83**:F1–F8.

2

Memory-Efficient Frequency-Domain Least-Squares RTM Using Low-Rank Green's Functions Via Stochastic SVD Algorithms

This chapter has been submitted as Daniel E. Revelo, Reynam C. Pestana, and Diego F. Barrera. *Memory-Efficient Frequency-Domain Least-Squares RTM Using Low-Rank Green's Functions Via Stochastic SVD Algorithms* to IEEE Transactions on Geoscience and Remote Sensing. Minor modifications have been applied to maintain consistency within this thesis.

Abstract

Least-squares reverse time migration in the frequency domain (FLSRTM) is capable of producing a high-resolution reflectivity model, provided that the Green's functions can be stored in memory. The Green's functions employed to compute the gradient and Born-modeled data must be calculated once and then stored; however, their size can be large, making this storage infeasible depending on the available hardware. FLSRTM using low-rank Green's functions decomposed via singular value decomposition (SVD) can be used to alleviate this constraint. However, the SVD decomposition could result in a significant increase in computational time when dealing with large datasets and models of considerable size. To overcome this issue, we propose the FLSRTM scheme with a low-rank Green's function by exploiting randomized (rSVD) and compressed (cSVD) singular value decomposition algorithms. The Green's functions can then be saved efficiently as two unitary matrices with

a few dominant singular values, thus requiring little memory. Following the demonstration of the feasibility of rank reduction in Green's functions, we evaluate the proposed rSVD and cSVD FLSRTM schemes versus the reference fully-stored Green's functions FLSRTM and versus conventional low-rank SVD FLSRTM. These evaluations are conducted using both a layered model and the modified Marmousi-2 model. Our proposed FLSRTM scheme can generate image results identical to the comparative methods while also requiring less memory than FLSRTM, which saves the complete Green's functions, and less computational time compared to the FLSRTM scheme with low-rank Green's functions via conventional SVD.

Introduction

Migration is a crucial seismic processing stage responsible for building images in depth of the subsurface from time-recorded data. It corrects the depth and inclination of the reflectors and suppresses diffractions (Claerbout, 1992; Andrade et al., 2017). Among the seismic migration techniques, reverse time migration (RTM) (Baysal et al., 1983; McMechan, 1983; Whitmore, 1983; Levin, 1984), which involves back-propagating field data, using the two-way wave equation (Ren et al., 2013), has been proven to be the most accurate imaging technique. This is due to its ability to image arbitrarily complex and steeply dipping structures in the subsurface provided an accurate velocity model is available. With the increasing demands of oil and gas exploration, there is a growing need for seismic imaging to provide more comprehensive information beyond just the subsurface structure, such as reflectivity. Despite the satisfactory results obtained by RTM, the seismic migration operator has an adjoint relationship with a forward Born modeling operator (Liu et al., 2022). Therefore, an important aspect affecting the seismic migration image is the inability of the adjoint operator to accurately approximate the inverse operator (Claerbout, 1992; Symes, 2009). Consequently, the resulting image may suffer from blurred effects with incorrect amplitude and migration artifacts under imperfect acquisition circumstances, such as band-limited seismic source, finite recording aperture, irregular sample acquisition geometry, or missing frequencies (Nemeth et al., 1999; Etgen et al., 2009; Liu et al., 2022; Kim et al., 2022).

To overcome this issue, Tarantola (1984) introduced an effective method to enhance the quality of the migration image and to generate an amplitude-preserved imaging result. This approach, known as least-squares migration (LSM) (Bamberger et al., 1982), is a linearized inversion scheme based on the minimization of a least-squares function. It approximates the inverse operator by minimizing the defined objective function with a gradient-based optimization method iteratively (Nemeth et al., 1999; Dutta and Schuster, 2014). In particular, when the LSM is based on the two-way wave equation, it is referred to as least-squares reverse time migration (LSRTM) (Schuster, 1993; Nemeth et al., 1999; Dong et al., 2012; Yao et al., 2022), which is based on the Born approximation and is more efficient at accurately migrating complex geological structures (Wong et al., 2012). A typical iterative LSRTM consists of three main components: a modeling operator to simulate seismic data, a migration operator to compute the gradient, and an inversion solver to minimize the objective function. Considering that the gradient of the misfit function computed in time-domain LSRTM (TLSRTM) must be calculated independently for each shot gather (Herrmann and Li, 2012; Dai et al., 2012; Zhang et al., 2015), the computational cost of TLSRTM can dramatically increase proportionally to the number of data gathers used. Significant advancements have been achieved recently aimed at enhancing the quality of seismic imaging while concurrently reducing computational costs of TLSRTM (Herrmann and Li, 2012; Dai and Schuster, 2013; Xue et al., 2016; Yao and Jakubowicz, 2016; Liu and Peter, 2018).

Frequency-domain LSRTM (FLSRTM) can be employed to reduce the computational cost of LSRTM for multi-source processing, offering several advantages over TLSRTM. Notably, only a few valid frequency components of the data are needed to generate the migrated section (Kim et al., 2022). Furthermore, if the Green's functions can be stored in the computer's memory, the gradient and Born-modeled data can be efficiently computed without the need for additional wavefield extrapolation (Ren et al., 2013). We note that in the FLSRTM scheme, the perturbed scattering wavefield and the gradient of the misfit function are expressed as a function of background Green's functions in the frequency domain. Considering that this framework is a linearized inversion and does not update the background model, all of the background Green's functions from the sources to the reflectors and from the reflectors to the receivers, which depend on the background velocity, must be calculated once and stored in the computer's memory for each frequency. Although FLSRTM is shown to be efficient, this scheme can be severely limited by the substantial memory storage requirements for saving the Green's functions, especially when a large dataset and model are used (Liu et al., 2022). To mitigate this, Ren et al. (2013) implemented a version of FLSRTM in which the shot and receiver Green's functions are stored in memory during the first iteration of the inversion scheme. As an alternative approach, Zhao and Sen (2019) proposed the double-plane-wave encoding of shot records to reduce memory storage requirements for saving the Green's functions.

More recently, Kim et al. (2022) introduced a fast and memory-efficient version of FLSRTM, in which they adopted the singular value decomposition (SVD) to construct the low-rank representation of Green's functions and reduce the required memory storage. Although the FLSRTM scheme with low-rank background Green's functions can produce migration results as accurately as conventional FLSRTM schemes with less memory usage, generating this low-rank representation via SVD can be computationally intensive, particularly when dealing with large-scale datasets or models. Alternatively, iterative algorithms such as Krylov-subspace methods can be employed to approximate the dominant singular vectors more efficiently (Golub and Van Loan, 1996). These algorithms are the most widely used approach for computing low-rank matrix approximations, especially for large sparse matrices. However, over the past two decades, stochastic algorithms have gained popularity. This is because randomized algorithms often perform better in practice and are more robust compared to Krylov methods (Martinsson, 2019). The basic idea of these probabilistic matrix algorithms is to employ some amount of randomness to derive a smaller matrix from a high-dimensional matrix, which captures the essential information and offers reliability and a computationally efficient alternative to obtain a low-rank SVD representation (Sarlos, 2006; Gu, 2015; Erichson et al., 2019).

In this study, we propose implementing an FLSRTM scheme that utilizes low-rank Green's functions decomposed via randomized (rSVD) (Halko et al., 2011; Martinsson et al., 2011; Halko, 2012; Tropp and Webber, 2023) and compressed (cSVD) (Erichson et al., 2017; Erichson et al., 2019) SVD algorithms to improve runtime performance. The enhanced algorithm aims to tackle the computational challenges associated with conventional FLSRTM. The cornerstone of the solution lies in the rSVD and cSVD algorithms' proficiency in efficiently extracting critical information from Green's functions to construct their low-rank representations. Unlike conventional SVD, the rSVD and cSVD algorithms begins by generating a compressed matrix from the original matrix using a Gaussian random matrix and an economic QR decomposition. The size of the compressed matrix is determined by the truncation coefficient, which corresponds to the optimal rank and is determined using a specific criterion (Kim et al., 2022). Liu and Peter (2020) demonstrated that if the truncation coefficient is finely adjusted, these algorithms can significantly compress the original matrix, leading to decreased memory usage and reduced computation time. Although the rSVD algorithm is mathematically robust and offers strong error bounds, there is potential for innovations and improvements, such as those introduced in the cSVD algorithm presented by Ji and Li (2014). The cSVD algorithm provides an effective balance between accuracy and speed, and is particularly well-suited for approximating large matrices. Consequently, its computational advantages become more significant as the dimensions increase.

This article is structured as follows. First, we provide a brief overview of LSM and FLSRTM. Following this, we introduce the SVD algorithm and its low-rank randomized variations. Subsequently, we explain the integration of SVD algorithms within the FLSRTM framework. Then, we demonstrate the capability of the proposed algorithm to produce high-quality seismic images through numerical experiments conducted on synthetic models.

Afterwards, through a comparative analysis of migration results and computational costs based on numerical examples, we illustrate the efficiency of the FLSRTM scheme in terms of memory storage and computing time by employing the low-rank representation of Green's functions via stochastic SVD algorithms.

Methodology

Least-squares migration

According to the Born approximation Woodward1992,BornWolf1999, the reflectivity model $\mathbf{m}$ and the first-order scattering data $\mathbf{d}$ satisfy the following linear relationship

$$\mathbf{d} = \mathbf{L}\mathbf{m}, \tag{2.1}$$

where $\mathbf{L}$, known as the sensitivity kernel, represents the forward Born modeling operator that uses a smooth background velocity model.

Conventionally, the adjoint of the $\mathbf{L}$ operator is considered as the migration operator (Claerbout, 1992), and the reflectivity model $\mathbf{m}_{\text{mig}}$ is retrieved by applying it to the observed data $\mathbf{d}_{\text{obs}}$, represented as

$$\mathbf{m}_{\text{mig}} = \mathbf{L}^{\text{T}}\mathbf{d}_{\text{obs}}, \tag{2.2}$$

where T means the conjugate transpose. Despite the widespread use of the imaging method outlined in equation 2.2, known for its high precision, it is important to note that seismic migration images may still be subject to issues such as blurring effects, low resolution, and unbalanced amplitudes (Schuster, 2017; Shoja et al., 2022). To partially mitigate these issues, least-squares migration (LSM), often referred to as linearized Born inversion (Tarantola, 1984; Nemeth et al., 1999), is commonly proposed for the inversion of seismic data to obtain the reflectivity distribution. Provided that the migration velocity model is sufficiently accurate, LSM can mitigate many of the previously mentioned problems, leading to a more detailed and resolved migration image (Schuster, 2017). In the LSM method, the strategy to improve the quality of $\mathbf{m}_{\text{mig}}$ involves defining an objective function E. This function is designed to seek the reflectivity by minimizing the L_2-norm of the difference between the forward-modeled data and the recorded data

$$E(\mathbf{m}) = \frac{1}{2}||\mathbf{L}\mathbf{m} - \mathbf{d}_{\text{obs}}||^2. \tag{2.3}$$

In the least-squares sense, the optimal solution for equation 2.3 is expressed as $\mathbf{m} = \mathbf{H}^{-1}\mathbf{m}_{\text{mig}}$, where $\mathbf{H} = \mathbf{L}^{\text{T}}\mathbf{L}$ is the Hessian operator. However, the computation of the inverse Hessian is prohibitively expensive (Zhou et al., 2014; Schuster, 2017). To circumvent this limitation, the reflectivity distribution $\mathbf{m}$ can be iteratively estimated using gradient-based methods to solve the optimization problem presented in equation 2.3. In this study, we will employ the steepest descent method (Nemeth et al., 1999) for this purpose. With this approach, the solution is updated at each iteration by

$$\mathbf{m}_{\tau+1} = \mathbf{m}_{\tau} - \alpha \mathbf{g}_{\tau}, \tag{2.4}$$

where τ is the iteration number, α is the optimized step length

$$\alpha = \frac{\mathbf{g}_{\tau}^{\mathrm{T}} \mathbf{g}_{\tau}}{(\mathbf{L}\mathbf{g}_{\tau})^{\mathrm{T}}(\mathbf{L}\mathbf{g}_{\tau})}, \tag{2.5}$$

and the migration of the difference between Born data modeling and observed data, i.e., $\Delta \mathbf{d} = \mathbf{L}\mathbf{m}_{\tau} - \mathbf{d}_{\mathrm{obs}}$, corresponds to the gradient vector

$$\mathbf{g}_{\tau} = \mathbf{L}^{\mathrm{T}}(\mathbf{L}\mathbf{m}_{\tau} - \mathbf{d}_{\mathrm{obs}}) = \mathbf{L}^{\mathrm{T}} \Delta \mathbf{d}. \tag{2.6}$$

From equations 2.1, 2.5 and 2.6, it is evident that the implementation of an iterative LSM scheme requires a forward modeling engine. In the context of this study, the engine aligns with the forward linear modeling operator derived from the two-way equation in the frequency domain. Next, the derivation of the forward Born modeling operator will be presented, along with its incorporation into the LSM scheme.

Matrix formulation of the frequency-domain least-squares RTM

Assuming a constant density and an isotropic medium, the two-dimensional acoustic wave equation in the frequency domain is expressed as follows

$$\left[\nabla^2 + \frac{\omega^2}{c^2(\mathbf{x})}\right] P(\mathbf{x}, \omega) = \delta(\mathbf{x} - \mathbf{x}_s) F(\omega), \tag{2.7}$$

where $\mathbf{x} = (x, z)$, ω is the angular frequency, $c(\mathbf{x})$ represents the velocity of the medium, ∇^2 is the Laplacian operator, and $P(\mathbf{x}, \omega)$ denotes the pressure wavefield in the frequency domain associated with the spectrum of the source term $F(\omega)$ injected at the position $\mathbf{x}_s$.

In the Born approximation, a linear relationship is assumed where a perturbation in the velocity generates a corresponding perturbation in the pressure wavefield. Thus, defining $c(\mathbf{x})$ as $c_0(\mathbf{x}) + \delta c(\mathbf{x})$, where $\delta c(\mathbf{x})$ is the pertubation in the background velocity model $c_0(\mathbf{x})$, the pressure wavefield $P(\mathbf{x}, \omega)$ will be given by $P_0(\mathbf{x}, \omega) + \delta P(\mathbf{x}, \omega)$, with $\delta P(\mathbf{x}, \omega)$ representing the scattered wavefield due to the velocity model perturbation. After substituting these definitions into equation 2.7, and considering that $c_0 >> \delta c$ and $P_0 >> \delta P$, the scalar wave equation for the first-order scattering wavefield can be expressed as

$$\left[\nabla^2 + \frac{\omega^2}{c_0^2(\mathbf{x})}\right] \delta P(\mathbf{x}, \omega) = \omega^2 \frac{m(\mathbf{x})}{c_0^2(\mathbf{x})} P_0(\mathbf{x}, \omega), \tag{2.8}$$

where the reflectivity model $m(\mathbf{x})$ is defined as $\frac{2\delta c(\mathbf{x})}{c_0(\mathbf{x})}$ and $P_0(\mathbf{x},\omega)$ is the background acoustic wavefield, which satisfies equation 2.7 using the background velocity model. Equation 2.8 represents the linearized wave equation derived from the so-called Born approximation. The linearization in equation 2.8 is based on the premise that a perturbation in the model parameter, represented by the source term on the right side of equation 2.8, generates the first-order scattering $\delta P(\mathbf{x},\omega)$ (Albano et al., 2019).

By introducing the background Green's function $G_0(\mathbf{x},\omega)$, which solves the Helmholtz equation for the background medium (Morse and Feshbach, 1953), the background wavefield can be computed as the product of $G_0(\mathbf{x},\omega)$ and the spectrum of the source term, i.e., $P_0(\mathbf{x},\omega) = G_0(\mathbf{x},\omega)F(\omega)$ (Schuster, 2017). Utilizing this representation, equation 2.8 can be transformed into an equivalent integral equation of the Lippmann-Schwinger type (Lippmann and Schwinger, 1950). Therefore, the perturbed scattering wavefield recorded at $\mathbf{x}_r$ can then be determined using the following linear equation (Woodward, 1992; Born and Wolf, 1999)

$$\delta P(\mathbf{x}_r,\omega;\mathbf{x}_s) = -\int \omega^2 \frac{m(\mathbf{x})}{c_0^2(\mathbf{x})}\, F(\omega)\, G_0(\mathbf{x},\omega;\mathbf{x}_s)\, G_0(\mathbf{x},\omega;\mathbf{x}_r)d\mathbf{x}, \tag{2.9}$$

where $G_0(\mathbf{x},\omega;\mathbf{x}_s)$ is the Green's function from the source point at $\mathbf{x}_s$ to spreader position $\mathbf{x}$, $G_0(\mathbf{x},\omega;\mathbf{x}_r)$ is the Green's function from the receiver $\mathbf{x}_r$ to the position $\mathbf{x}$. Note that the Green's functions satisfy the source-receiver reciprocity principle, i.e., $G_0(\mathbf{x},\omega;\mathbf{x}') = G_0(\mathbf{x}',\omega;\mathbf{x})$.

Equation 2.9 provides the integral representation for Born forward modeling. Following Yao and Jakubowicz (2016), we will now discretize the scattered pressure field, the background velocity model, and the integral modeling operator to obtain a matrix-vector formulation for equation 2.9. For the 2D case, we considered the medium discretized onto a $nz \times nx$ mesh. We then represent the reflectivity distribution $m(\mathbf{x})$ as a model vector $\mathbf{m}$ with $N(= nz \times nx)$ elements, the first-order scattering wavefield $\delta P(\mathbf{x}_r,\omega;\mathbf{x}_s)$ as the data vector $\mathbf{d}$ with $M(= nr$, number of receivers) elements, and the Born modeling operator as the $\mathbf{L}$ matrix with $M \times N$ elements. Thus, for each frequency component, the integral in equation 2.9 can be approximated by a Riemman sum (Yao and Jakubowicz, 2016; Schuster, 2017; Liu et al., 2022), resulting in

$$\begin{bmatrix} d_1 \\ \vdots \\ d_i \\ \vdots \\ d_M \end{bmatrix} = \begin{bmatrix} l_{11} & \cdots & l_{1j} & \cdots & l_{1N} \\ \vdots & \ddots & \vdots & \ddots & \vdots \\ l_{i1} & \cdots & l_{ij} & \cdots & l_{iN} \\ \vdots & \ddots & \vdots & \ddots & \vdots \\ l_{M1} & \cdots & l_{Mj} & \cdots & l_{MN} \end{bmatrix} \begin{bmatrix} m_1 \\ \vdots \\ m_j \\ \vdots \\ m_N \end{bmatrix}, \tag{2.10}$$

where d_i represents the corresponding reflection data and l_{ij} is the value at the j-th grid of the sensitivity kernel corresponding to the i-th source-receiver pair, which is given by

$$l_{ij} = \frac{\omega^2}{c_0^2(\mathbf{x}_j)} F(\omega)\, G_0(\mathbf{x}_j, \omega; \mathbf{x}_s) G_0(\mathbf{x}_j, \omega; \mathbf{x}_{ri}). \tag{2.11}$$

The compact form of equation 2.10 can be expressed as a matrix-vector product, similar to the linear relationship presented in equation 2.1. Considering this and noting that the derivation of the equation 2.9 was based on the two-way equation in the frequency domain, the inversion scheme will be referred to as FLSRTM. From equation 2.6, it is evident that the steepest descent method requires the computation of the gradient vector $\mathbf{g}$. Consequently, using the matrix representation provided in equation 2.10, we compute the conjugate transpose of the $\mathbf{L}$ operator and obtain the following expression to calculate the gradient at each iteration of the FLSRTM scheme (Liu et al., 2022)

$$\begin{aligned}
\begin{bmatrix} g_1 \\ \vdots \\ g_j \\ \vdots \\ g_N \end{bmatrix} &= \mathfrak{Re}\left\{ \begin{bmatrix} \overline{l_{11}} & \cdots & \overline{l_{i1}} & \cdots & \overline{l_{M1}} \\ \vdots & \ddots & \vdots & \ddots & \vdots \\ \overline{l_{1j}} & \cdots & \overline{l_{ij}} & \cdots & \overline{l_{Mj}} \\ \vdots & \ddots & \vdots & \ddots & \vdots \\ \overline{l_{1N}} & \cdots & \overline{l_{iN}} & \cdots & \overline{l_{MN}} \end{bmatrix} \begin{bmatrix} \Delta d_1 \\ \vdots \\ \Delta d_i \\ \vdots \\ \Delta d_M \end{bmatrix} \right\} \\
&= \mathfrak{Re}\left\{ \sum_{i=1}^{M} \begin{bmatrix} \overline{l_{i1}} \\ \vdots \\ \overline{l_{ij}} \\ \vdots \\ \overline{l_{iN}} \end{bmatrix} \Delta d_i \right\},
\end{aligned} \tag{2.12}$$

where $\mathfrak{Re}$ denotes the real part of a complex number and $\mathbf{g}$ corresponds to the migration of residues and is shaped as a vector with $N(= nz \times nx)$ elements. In the $\mathbf{L}^{\mathrm{T}}$ operator, each element $\overline{l_{ij}}$, is represented as

$$\overline{l_{ij}} = \frac{\omega^2}{c_0^2(\mathbf{x}_j)} F^*(\omega)\, G_0^*(\mathbf{x}_j, \omega; \mathbf{x}_s) G_0^*(\mathbf{x}_j, \omega; \mathbf{x}_{ri}), \tag{2.13}$$

where $*$ is the complex conjugate.

As previously mentioned, because only the adjoint of the forward Born modeling operator is applied to the seismic data, as given in equation 2.2, the output migration profile is amplitude-biased. To partially balance the amplitudes, the migrated image can be preconditioned with the inverse of the diagonal of the Hessian operator (Shin et al., 2001; Liu et al., 2020). In a relevant study, Liu et al. (2022) developed a frequency-domain scattering-integral reverse time migration (SI-RTM), where the diagonal of the Hessian operator is explicitly computed in its exact form, i.e., $\mathbf{H}_0 = \mathrm{diag}\{\mathbf{L}^{\mathrm{T}}\mathbf{L}\}$. In this formulation, the preconditioned image with exact two-way illumination compensation is expressed as

$$\mathbf{m}_{\mathrm{mig}} = (\mathbf{H}_0 + \lambda \mathbf{I})^{-1} \mathbf{L}^{\mathrm{T}} \mathbf{d}_{\mathrm{obs}}, \tag{2.14}$$

where λ is a damping factor to prevent instability of the inverse operation, and $\mathbf{H}_0$ is computed by accumulating the squared modulus of each sensitivity kernel element over all source-receiver pairs, as follows

$$\mathbf{H}_0 = \sum_{i=1}^{M} \begin{bmatrix} \overline{l_{i1}} l_{i1} & \cdots & 0 & \cdots & 0 \\ \vdots & \ddots & \vdots & \ddots & \vdots \\ 0 & \cdots & \overline{l_{ij}} l_{ij} & \cdots & 0 \\ \vdots & \ddots & \vdots & \ddots & \vdots \\ 0 & \cdots & 0 & \cdots & \overline{l_{iN}} l_{iN} \end{bmatrix}. \tag{2.15}$$

The SI-RTM offers a significant advantage in terms of memory efficiency, as it does not necessitate storing large sensitivity kernels (Liu et al., 2022). Because the background Green's functions remain unchanged during the FLSRTM scheme, computational costs can be notably reduced, with $\mathbf{H}_0$ computed only once at the initial iteration of the optimization scheme. In this work, we have implemented the exact two-way illumination compensation to precondition the gradient. It is noteworthy that in our implementation, this preconditioned is also structured as a vector with $N(= nz \times nx)$ elements and is applied to the gradient via the Hadamard product.

Since in FLSRTM the background velocity model is kept unchanged, and only the reflectivity model is updated, the Green's functions needed for computing the scattered data and the gradient are computed only once. Therefore, if the Green's functions are stored in memory, both scattered data and gradient can be calculated without additional wavefield extrapolation. However, storing the Green's functions typically demands significant memory storage, which may become impractical for large-scale datasets and models. To alleviate this computational cost, in the next section, we propose an approach to FLSRTM using low-rank representation of Green's functions obtained via SVD algorithms.

Low-rank representation of Green's functions via SVD algorithms

In this explanation, we represent the background Green's functions as a two-dimensional $m \times n$ matrix $\mathbf{A}$, where m and n correspond to nz and nx, respectively. The conventional SVD of $\mathbf{A}$ admits the factorization of it into the product of three matrices, such that $\mathbf{A} = \mathbf{U}\mathbf{\Sigma}\mathbf{V}^{\mathrm{T}}$, where $\mathbf{U}$ is an $m \times n$ matrix of the orthonormal eigenvectors of $\mathbf{A}\mathbf{A}^{\mathrm{T}}$ and $\mathbf{V}^{\mathrm{T}}$ is the transpose of an $n \times n$ matrix containing the orthonormal eigenvectors of $\mathbf{A}^{\mathrm{T}}\mathbf{A}$ (Figure 2.1a). The $n \times n$ diagonal matrix $\mathbf{\Sigma}$ contains the corresponding non-negative singular values of $\mathbf{A}$ ($\sigma_1 \geq \ldots \geq \sigma_r \geq 0$), describing the spectrum of the data. The conventional SVD algorithm for a large matrix is computationally intensive and has cubic-time complexity with respect to the size of the given matrix (Golub and Van Loan, 1996), often necessitating substantial memory storage. However, in practice, a full SVD, including a fully unitary decomposition of the matrix's null space, is rarely required. Instead of the full factorization, it is often sufficient to compute a compact version of the SVD algorithm based on the matrix's rank, denoted by r, which corresponds to the number of non-zero singular values of $\mathbf{A}$.

In many applications, the rank of $\mathbf{A}$ is large, making it difficult to store even the SVD factors in memory. In such instances, the smallest singular values may need to be truncated to retain only the largest k non-zero singular values (low-rank approximation, where $k << r$). Thus, the low-rank SVD is no longer an exact decomposition of the original matrix $\mathbf{A}$, but rather provides the optimal low-rank matrix approximation $\mathbf{A}_k$ by any matrix of a fixed rank k, i.e., $\mathbf{A}_k \approx \mathbf{U}_k \mathbf{\Sigma}_k \mathbf{V}_k^{\mathrm{T}}$, where k denotes the desired target rank of the approximation, and only the k column vectors of $\mathbf{U}$ and k row vectors of $\mathbf{V}^{\mathrm{T}}$ corresponding to the k singular values with a significant magnitude are preserved (Figure 2.1b). Choosing an optimal target rank k is highly dependent on the task: a value for k close to the effective rank allows us to obtain a highly accurate reconstruction of $\mathbf{A}$, which on the other hand, a small value for k results in a very low-dimensional representation of the dominant features of $\mathbf{A}$ (Erichson et al., 2019). Kim et al. (2022) proposed an FLSRTM inversion scheme using low-rank Green's functions computed via conventional SVD, demonstrating the feasibility of this low-rank representation in reducing the required computational memory. Building on the work of Kim et al. (2022), we will adopt the following scheme in our implementation to determine the optimal target rank: (*i*) select the Green's function corresponding to the most energetic component of the frequency spectrum, (*ii*) apply conventional SVD to obtain the distribution of the singular values, and (*iii*) select the rank where the normalized accumulated singular value exceeds 99.9 %.

Although the amount of memory required to save the resulting factors of the low-rank SVD is less than the conventional SVD, this approach still requires the initial computation of the conventional SVD. From this, the first k components are extracted to form $\mathbf{A}_k$. Consequently, the computation of $\mathbf{A}_k$ via conventional SVD does not offer any reduction in computation time. This method, therefore, remains impractical for high-dimensional data matrices. To address the issue related to the computational execution time, we propose calculating the low-rank Green's functions using two stochastic SVD algorithms. The first method is the randomized SVD algorithm (rSVD), introduced by Halko et al. (2011), which is designed to obtain a low-rank approximation of a large matrix. Recognized as a state-of-the-art algorithm for computing low-rank matrix approximations (Mahoney, 2011), this algorithm circumvents the conventional SVD computation on a large matrix. Instead, it performs a random sampling on the original matrix to construct a small condensed subspace and then projects $\mathbf{A}$ onto this subspace (Ji and Li, 2014). Thereafter, a deterministic matrix factorization algorithm is applied to the smaller dense matrix to compute a near-optimal low-rank approximation of $\mathbf{A}$. Such algorithm has been shown to be computationally efficient with a relatively low computation cost and high confidence for approximating matrices with low-rank structures (Halko et al., 2011; Martinsson et al., 2011; Halko, 2012; Tropp and Webber, 2023).

The rSVD comprises the following six primary computational components (refer to Figure 2.2a): (*i*) generation of a $n \times k$ random matrix $\boldsymbol{\Omega}$, (*ii*) matrix-matrix multiplication of $\mathbf{A}\boldsymbol{\Omega}$ to produce $\mathbf{Y}$, (*iii*) QR decomposition of $\mathbf{Y}$ to obtain the near-optimal basis $\mathbf{Q}$, (*iv*) matrix-matrix multiplication to project the input matrix to low-dimensional space, i.e., $\mathbf{Q}^{\mathrm{T}}\mathbf{A}$, to produce the relatively small matrix $\mathbf{B}$, (*v*) conventional SVD decomposition on $\mathbf{B}$, and (*vi*) recovery of the left singular vectors $\mathbf{U}_k$ from the approximate left singular vectors $\tilde{\mathbf{U}}_k$ by pre-multiplying by $\mathbf{Q}$. As described by Erichson et al. (2019), the basis matrix $\mathbf{Q}$ often fails to provide a good approximation for the column space of the input matrix. Therefore, it is necessary to use a power iteration scheme (Rokhlin et al., 2010; Halko et al., 2011; Gu, 2015) in order to enhance the quality of this step. In this research, we have used the power iteration scheme with $p = 2$ and a QR decomposition as an intermediate step (Rokhlin et al., 2010), which is accurate and reduces the stability problems of conventional implementation. It is important to note that, after random matrix sampling by $\boldsymbol{\Omega}$, the input matrix $\mathbf{A}$ is condensed into either tall-and-skinny or a short-and-wide matrix, such as $\mathbf{Y}$ and $\mathbf{Q}$ are $m \times k$ matrices, and $\mathbf{B}$ is an $k \times n$ matrix, where k is much smaller than $\min(m, n)$. The small and dense matrix $\mathbf{B}$ is particularly suitable to reduce the computational cost of conventional SVD on the input matrix, being that significant computational speedups are achieved if the target rank k is about $3 - 6$ times smaller than the smallest dimension of $\mathbf{A}$ (Erichson et al., 2019). Finally, the amount of memory required to store the resulting arrays of this algorithm is similar to the memory demanded by the low-rank SVD, since it depends on the target rank k.

The other probabilistic matrix algorithm is the compressed SVD (cSVD), introduced by Ji and Li (2014). This method represents an advancement over the rSVD algorithm, focusing on computing the top-k singular vectors of $\mathbf{B}\mathbf{B}^{\mathrm{T}}$ instead of performing the conventional SVD directly on the matrix $\mathbf{B}$ (Figure 2.2b). It follows the initial four stages of the rSVD algorithm. Then, the matrix-matrix multiplication $\mathbf{B}\mathbf{B}^{\mathrm{T}}$ yields a small square matrix whose size only depends on the target rank k, offering a more efficient approach to derive the factor $\mathbf{U}_k$. Under the assumption that $\tilde{\mathbf{U}}_k^{\mathrm{T}}\tilde{\mathbf{U}}_k \approx \mathbf{I}$, the matrix $\mathbf{V}_k^{\mathrm{T}}$ can be effectively approximated via the single matrix-matrix operation $\tilde{\mathbf{U}}_k^{\mathrm{T}}\mathbf{B} \approx \boldsymbol{\Sigma}_k\mathbf{V}_k^{\mathrm{T}}$. As mentioned earlier, this algorithm reduces the computational execution time. However, the amount of memory required to store the resulting matrices is similar to that required by the rSVD.

In summary, we propose to implement the FLSRTM as described by equations 2.4-2.6 and to evaluate the resulting high-resolution images obtained from the inversion scheme using a low-rank representation of Green's functions. Implementing FLSRTM requires storing the background Green's functions to compute the Born data and gradient at each iteration, which can be impractical for large-scale datasets and models. To mitigate this issue, we advocate applying rSVD or cSVD algorithms to reduce the rank of the Green's functions. Therefore, alongside assessing the quality of the migrated images, we evaluate the computational performance of these stochastic SVD algorithms for computing low-rank representation of Green's functions. The workflows for implementing each FLSRTM, whether using the full Green's functions or the low-rank representation via SVD algorithms, are illustrated in Figure 2.3.

Numerical tests

In this section, we present two numerical examples to evaluate the performance of our proposed FLSRTM scheme in generating high-quality seismic images using the low-rank representation of Green's functions via stochastic SVD algorithms. For both synthetic examples, we used similar parameters to generate the background Green's functions, construct their low-rank representations, and execute the inversion scheme. Additionally, to ensure consistency and comparability of the results, all tests were performed using the same hardware configuration.

Considering that computing the background Green's functions for each iteration of the FLSRTM inversion scheme is uncommon and significantly increases computation time, we have precomputed these functions and stored them on disk for our tests. For this, we defined a split-spread geometry with shots and receivers located on the surface and equally distributed over the model range. A 15 Hz Ricker wavelet was employed as the source wavelet, with a record length of 4 s and a time sampling interval of 4 ms. Subsequently, utilizing the background velocity model, we conducted numerical modeling to compute the acoustic wavefield by employing the rapid expansion method (REM) (Pestana and Stoffa, 2010). The background Green's functions were then obtained by deconvolving these wavefields with the Ricker source wavelet.

On the other hand, it is important to mention that the value of the optimal rank depends on the frequency component of the background Green's function. To circumvent this dependence, we applied the approach proposed by Kim et al. (2022), wherein the Green's function representing the seismic source located at the midpoint of the model surface is initially selected. The component corresponding to the dominant frequency is then chosen, followed by the application of the conventional SVD algorithm to construct its distribution of normalized accumulated singular values. The selection criterion is subsequently applied to determine the optimal rank k, which can be extended to other frequency components as well as to sources and receivers in the split-spread geometry. This ensures that the reconstructed Green's functions are nearly identical to the original Green's functions. Once the optimal value k is defined, the rSVD and cSVD algorithms can be applied. In this study, we utilized routines from the Linear Algebra PACKage (LAPACK) (Anderson et al., 1999) to perform the necessary SVD and QR factorizations in the implementation of these stochastic SVD algorithms. To validate the accuracy of the reconstructed Green's function, we adopted the normalized root-mean-square (NRMS) error.

In the context of the FLSRTM scheme, we have set the number of iterations to 20. Furthermore, a modified Laplacian filter was applied to attenuate low-wavenumber artifacts observed in the gradient computed at each iteration of the inversion process (Kumar et al., 2023). Implemented in the frequency domain, this filter efficiently suppresses migration artifacts without distorting the spectrum and amplitude of the migrated image. To compare the performance of the proposed FLSRTM, four cases were tested: saving the original Green's functions (case 1 - see left part of Figure 2.3), utilizing the low-rank representation of the Green's functions via SVD (case 2), rSVD (case 3) and cSVD (case 4) algorithms. The workflow for implementing FLSRTM using low-rank Green's functions is depicted in the right part of Figure 2.3. It is important to note that in cases 2-4, before initiating the inversion scheme, the factors $\mathbf{U}_k$, $\mathbf{\Sigma}_k$ and $\mathbf{V}_k^{\mathrm{T}}$ are computed using the implemented SVD algorithms. However, only the terms $\mathbf{U}_k\mathbf{\Sigma}_k$ and $\mathbf{V}_k^{\mathrm{T}}$ are retained in memory. This approach does not influence the low-rank approximation, does not significantly increase computation time, and also circumvents the need for storing the singular values.

Layered model

The first experiment utilized a layered model, characterized by a gradual increase in velocities from 1500 to 2400 m/s, indicating a smoothly varying subsurface structure with no abrupt transitions, as illustrated in Figure 2.4a. The model space was discretized into 401 × 501 grid nodes with a grid interval of 4 m in the vertical direction and 8 m in the horizontal direction. Figure 2.4b presents the background velocity model, obtained by applying a smoothing filter to the true model, while the reflectivity model is shown in Figure 2.4c. For this model, we employed a split-spread geometry with 251 shots and 250 receivers located on the surface. Consequently, we have a source at 0 m, a receiver at 8 m, a source at 16 m, a receiver at 24 m and so on. Subsequently, the REM method was utilized to compute the background Green's functions for this configuration.

Before applying stochastic SVD algorithms to this numerical experiment, we analyzed the optimal rank for reducing the Green's function. As previously mentioned, the optimal rank must be determined from the Green's function at the dominant frequency. In this experiment, the 15 Hz Green's function generated by a source at 2000 m (see red star in Figure 2.4a) was used to identify the optimal rank. Figure 2.4d shows the real part of this function. Conventional SVD was performed on the Green's function to compute the distribution of normalized singular values (Figure 2.5a). To apply the criterion for determining k, we calculated the normalized accumulated singular values (Figure 2.5b) and set the rank that has an accumulated singular value above 99.9 %. We notice that $k = 39$ satisfies this criterion (see red mark in Figure 2.5b), and it is also smaller than $nz = 401$. With the optimal rank identified, we computed the low-rank representation of the Green's function using SVD, rSVD, and cSVD algorithms.

To verify the accuracy of low-rank representations, the Green's functions were reconstructed, and their differences from the raw Green's function were computed, as depicted in Figure 2.6. The reconstructed Green's functions, which closely approximate the true Green's function, have a NRMS error of 8.46×10^{-4} for the conventional SVD and 8.95×10^{-4} for the two stochastic SVD algorithms implemented. Horizontal profiles were extracted from the low-rank Green's functions at a vertical distance of 800 m, and a comparison with a reference is illustrated in Figure 2.7a. This comparison demonstrates that the profiles match quite well. To examine the distribution of singular values in these low-rank Green's functions, we applied SVD decomposition to them. Figure 2.7b shows that the rSVD and cSVD distributions align closely with the reference singular values. In this numerical experiment, it is observed that the memory footprint required to store the low-rank approximation of the 15 Hz Green's function (0.268 MB) constitutes merely a fraction of the memory required by the original function (1.533 MB). This clearly demonstrates that SVD methodologies offer superior memory efficiency. Figure 2.16a shows the normalized computational times to perform the SVD, rSVD, and cSVD algorithms. The computation times for both rSVD and cSVD are markedly lower than the time expended by the conventional SVD, with the cSVD algorithm being particularly noteworthy.

We proceed to compare the FLSRTM results from each case. The inversion process employs 180 frequencies, with an interval of 0.25 Hz, and ranging from 0.25Hz to 45 Hz. For the parallel inversion, we utilize 90 CPU cores, with each node processing two frequencies of Green's functions for every shot and receiver, requiring 1.500 GB for case 1. Given that the optimal rank is 39, the memory demand for each node is significantly reduced to 0.262 GB for cases 2-4, which is approximately 17.5 % of the memory required in case 1. Since the dimensions of the low-rank Green's functions are much smaller than those of the original Green's functions, cases 2-4 require small memory storage. Figure 2.9 presents the RTM images (left column) and the inverted reflectivity model (right column) after 20 iterations. The normalized misfit values, as a function of iteration, exhibit uniform results across all cases (Figure 2.8). However, an almost negligible difference in the convergence curves is observed, which is associated with the truncation carried out to generate the low-rank representation of the Green's functions. A comparison of the FLSRTM images with the RTM images reveals that the FLSRTM process enhances both the quality and resolution of the image beyond the RTM results. The FLSRTM reflectivity models align well with the true reflectivity (Figure 2.4c). As expected, case 1 demands the most memory usage but exhibits the least computation time, which is established as our time reference. Cases 2-4 consumed additional computational time to compute the low-rank Green's functions at the initial iteration and to reconstruct the Green's function at each subsequent iteration (refer to the shadowed gray area in Figure 2.3). As depicted in Figure 2.16b, the normalized times consumed for each case clearly indicate the superior efficiency of the FLSRTM scheme using stochastic SVD algorithms to construct the low-rank representation of the background Green's functions.

Modified Marmousi-2 model

To evaluate the performance of the proposed algorithm, we conducted a second test using the Marmousi-2 model (Martin et al., 2006), which features larger dimensions compared to the previous test. This model represents a marine subsurface section with complex geological structures, including sedimentary layers and irregular rock formations. As depicted in Figure 2.10a, the model used here is a modified version of the released Marmousi-2 model, generated according to the description in Kim et al. (2022). This modified model has a depth of 3500 m and a length of 9200 m, with grid dimensions of 351 × 921 and grid intervals of 10 m. Figure 2.10b illustrates the background velocity model, derived from applying a filter to the true velocity model. The reflectivity model is presented in Figure 2.10c. For this numerical experiment, we constructed a fixed-spread geometry with 461 sources, with shot positions ranging from 0 m to 9200 m at 20 m intervals. Each shot has 460 receivers, starting from 10 m to 9190 m at 20 m intervals. Using the background velocity model as input and employing the REM, we conducted forward modeling to compute and store the background Green's functions for the specified geometry.

In this example, given that the dominant frequency of the source wavelet is 15 Hz, we utilized the 15 Hz Green's function, generated by a source at 4600 m (see red star in Figure 2.10a), to validate the implementation of the SVD algorithms and determine the optimal rank k. Figure 2.10d shows the real part of this 15 Hz Green's function. Consequently, a conventional SVD was performed on the Green's function to compute its distribution of normalized singular values (Figure 2.11a). We then calculated the normalized accumulated singular values (Figure 2.11b) and applied the predefined criterion to set the optimal rank. We notice that $k = 75$ satisfies the defined criterion (see red mark in Figure 2.11b), therefore, we set the optimal rank as 75 for reducing the dimension of the Green's function safely. In contrast to the Green's function in the previous numerical example (Figure 2.4d), the current Green's function presents greater complexity due to wavefield simulations in a geologically intricate model. As a result, the necessary optimal rank for reconstructing the Green's function has increased. Using this optimal rank, we computed the low-rank representation of the Green's function via conventional and stochastic SVD algorithms.

Figure 2.12 shows the reconstructed Green's functions with only 75 decomposed matrices and their differences from the original Green's functions. It is clearly verified that the low-rank Green's functions with optimal rank are very similar to the original function. From the reconstructed Green's functions, we extracted horizontal profiles and compared them with the reference, as shown in Figure 2.13a. Overall, no noticeable differences can be observed, and the traces appear nearly identical. Figure 2.13b displays the distribution of the normalized singular values for each decomposition scheme, which are remarkably close to the reference singular values. The NRMS error between the low-rank Green's function and the reference for the SVD, rSVD, and cSVD algorithms was 4.84×10^{-4}, 5.13×10^{-4} and 5.16×10^{-4}, respectively. For this numerical experiment, the memory required to store the low-rank 15 Hz Green's function was 0.728 MB, representing only a fraction of the 2.466 MB needed for the original function. As another aspect of computational cost, the normalized times consumed for the SVD, rSVD, and cSVD were 1, 0.240, and 0.097, respectively. These results confirm that the use of stochastic SVD algorithms enhances memory efficiency akin to the conventional SVD algorithm. However, these algorithms require less computing time (Figure 2.16a), with the cSVD algorithm standing out by being 10.4× faster.

FLSRTM for each case was performed with 180 frequencies sampled at 0.25 Hz and ranging from 0.25 Hz to 45 Hz. We used 90 CPU cores for the parallel inversion, with each node storing two frequencies of Green's functions for every shot and receiver (4.436 GB of storage). Since the optimal rank is 75, the memory requirement for each node is reduced to 1.310 GB. The misfit convergence curves for the different cases are shown in Figure 2.14. Despite the minor differences between the curves, attributed to the truncation performed to obtain the low-rank representation of the Green's functions, it is clearly observed that cases

2-4 converge to values very close to those reached in case 1. Figure 2.15 presents the RTM images (left column) and the inverted reflectivity models (right column) after 20 iterations. Comparing the FLSRTM images with the RTM images, it is evident that FLSRTM enhances both the quality and resolution of the images. The FLSRTM reflectivity models demonstrate a strong agreement with the true reflectivity, as shown in Figure 2.10c. Cases 2-4, even with the use of low-rank Green's functions, produce an inverted reflectivity model with quality identical to that of case 1. As can be seen in Figure 2.3, case 1 necessitates the highest memory allocation, yet it exhibits the shortest computational duration. Conversely, cases 2-4 require additional computational time (Figure 2.16b). This extra time is needed initially to construct the low-rank representation of the Green's functions and subsequently to assemble these at each iteration (refer to the shadowed gray area in Figure 2.3).

The results demonstrate the effectiveness of the proposed FLSRTM scheme, which utilizes stochastic SVD algorithms to reduce the computation time for constructing low-rank Green's functions. Furthermore, this approach minimizes the memory requirements for storing the background Green's functions, as previously demonstrated by Kim et al. (2022) using the conventional SVD algorithm. In contrast to other implemented algorithms, the cSVD factorization demonstrates superior performance. This can be attributed to its internal application of SVD decomposition on a square matrix of dimensions $k \times k$. Notably, this approach remains independent of the dimensions of the original matrix (refer to Figure 2.2b). As observed, the value of the optimal rank varied in each numerical example. Therefore, we can infer that the optimal rank for accurately reconstructing the Green's function increases when the velocity model features a complex geological structure. Consequently, the cSVD algorithm emerges as the most suitable choice when implementing the proposed FLSRTM scheme.

Conclusion

In this study, we propose an efficient scheme for implementing FLSRTM by utilizing low-rank Green's functions. While FLSRTM with fully stored Green's functions faces memory limitations for large-scale datasets or models, our approach overcomes this challenge. Specifically, we decompose the Green's function associated with the dominant frequency of the source wavelet into rectangular and unitary matrices using both conventional and stochastic SVD algorithms. The optimal rank, determined by a criterion based on the accumulated normalized singular value distribution, ensures efficient memory storage. Furthermore, we extend our investigation by incorporating randomized SVD and compressed SVD algorithms. These advancements significantly reduce computational time for constructing low-rank Green's functions. By leveraging rSVD and cSVD, we achieve substantial reductions in memory requirements without compromising computational efficiency. Our numerical experiments, conducted on a layered model and a modified Marmousi-2 model, demonstrate that the reconstructed Green's functions exhibit high accuracy using rank-reduced matrices. Comparative studies with FLSRTM using fully stored Green's functions validate the accuracy of our proposed FLSRTM scheme. Notably, the cSVD method consistently outperformed other approaches in terms of computational efficiency, making it the preferred choice for executing the FLSRTM scheme. Overall, we conclude that FLSRTM with low-rank Green's functions via rSVD and cSVD represents a computationally efficient approach for generating accurate migration images.

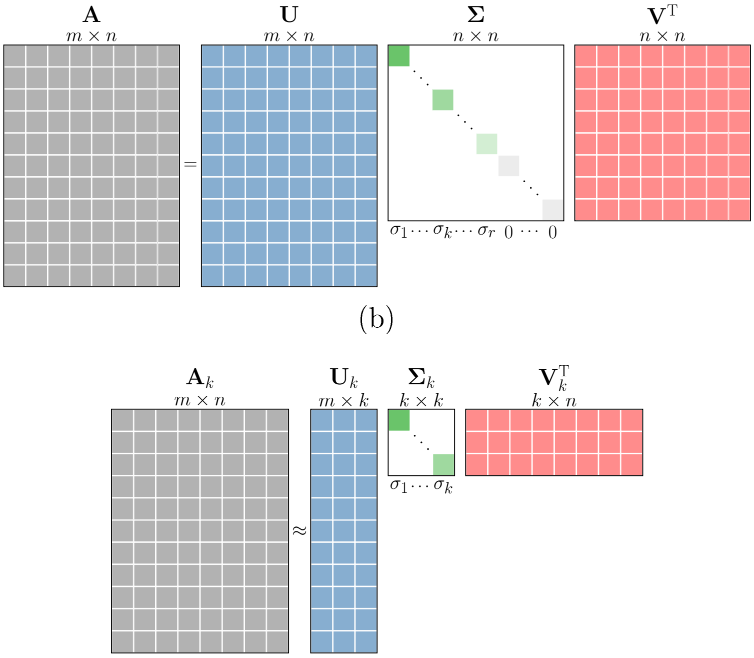

(b)

(a)

Figure 2.1: Schematic illustration of the (a) conventional and (b) low-rank SVD applied on a rank-r matrix $\mathbf{A}$. k denotes the desired target rank of the approximation.

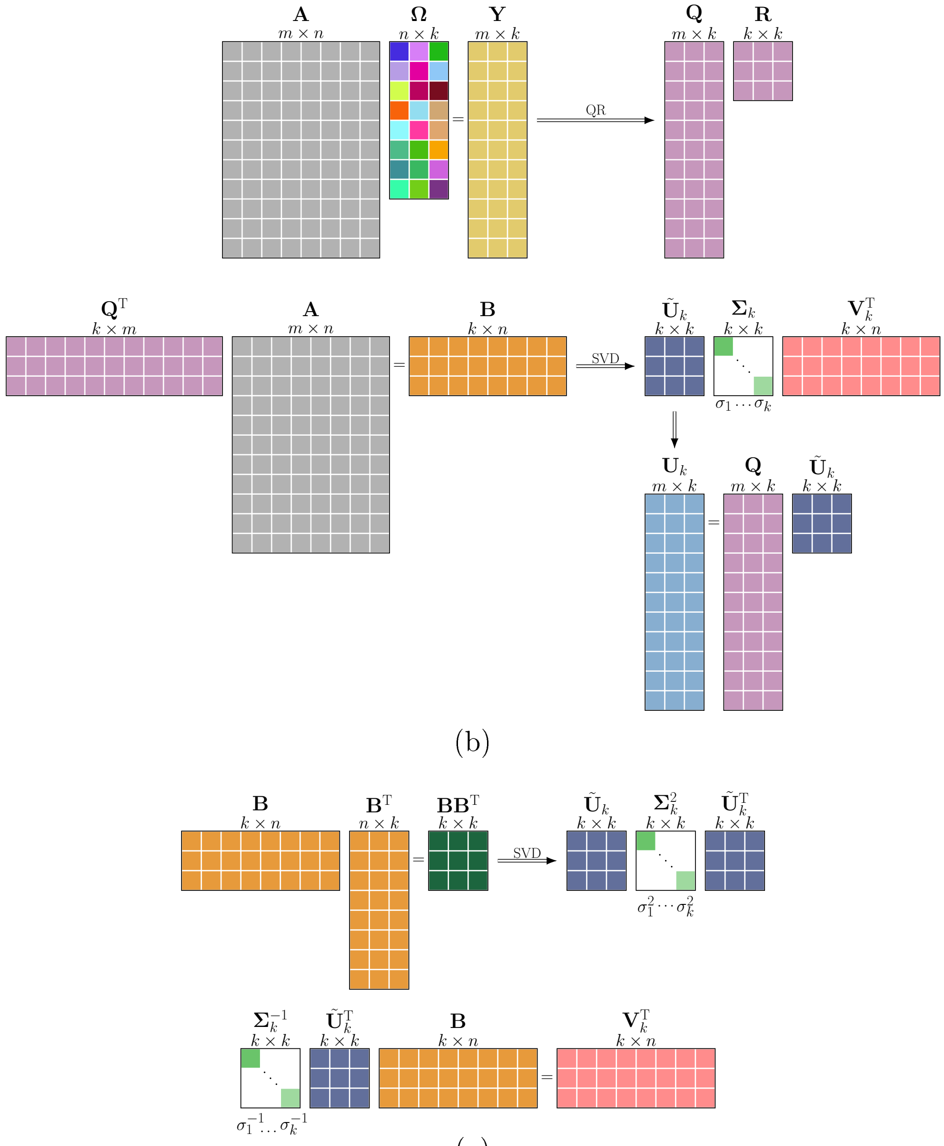

(b)

(a)

Figure 2.2: (a) The conceptual architecture of the randomized SVD involves several key steps. Initially, a natural basis $\mathbf{Q}$ is computed to derive a smaller matrix $\mathbf{B}$. Next, the SVD is efficiently performed on this reduced matrix. Finally, the left singular vectors $\mathbf{U}$ are reconstructed from the approximate singular vectors $\tilde{\mathbf{U}}$. (b) Schematic illustration of the compressed SVD. Since $\mathbf{B}\mathbf{B}^{\mathrm{T}}$ is a small square matrix whose size is independent of the size of the original matrix $\mathbf{A}$, the left singular vectors $\mathbf{U}$ can be derived much more efficiently than from $\mathbf{B}$, and the right singular vectors $\mathbf{V}^{\mathrm{T}}$ are reconstructed from the approximate singular vectors $\tilde{\mathbf{U}}$.

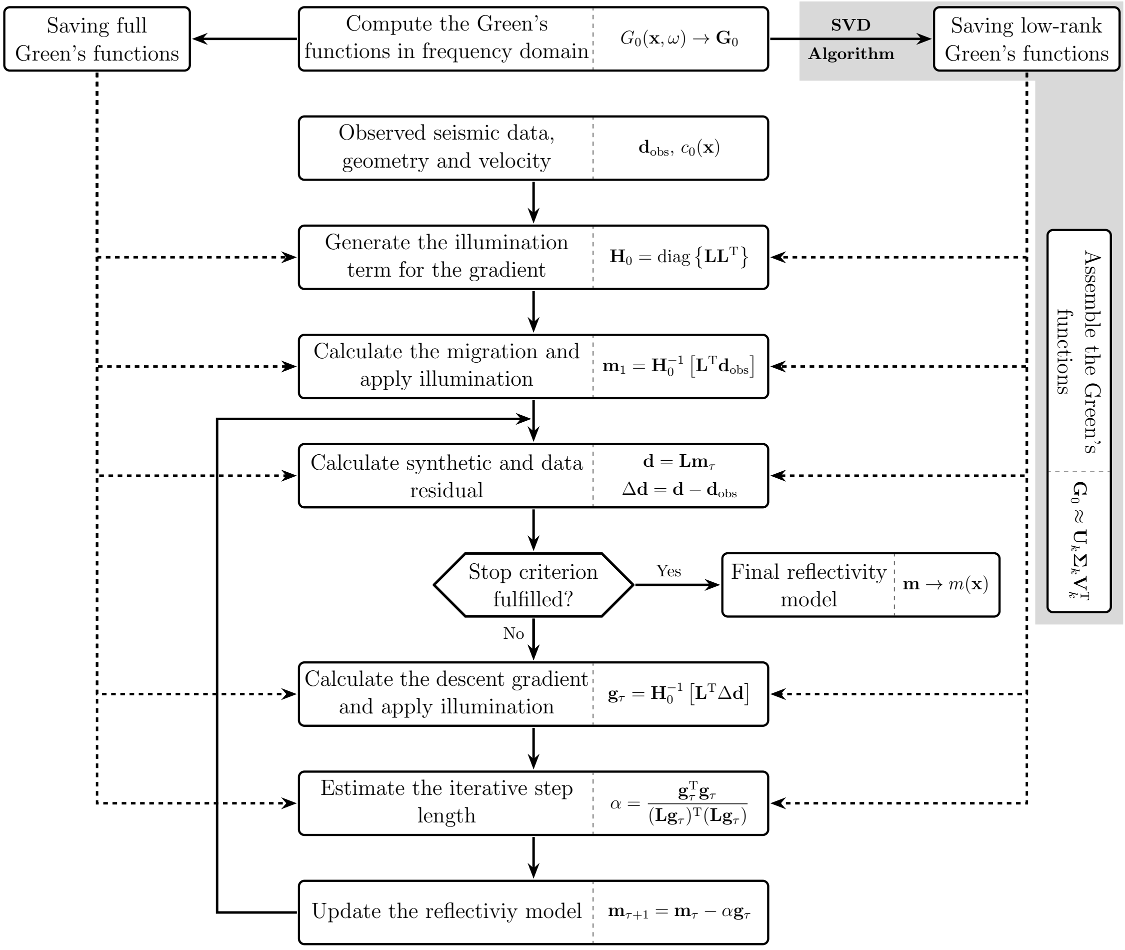

Figure 2.3: Flowchart for FLSRTM with saving full Green's function (on left) and our low-rank representation of Green's functions via conventional and stochastic SVD algorithms (on right). The dashed lines indicate the stages of the inversion scheme where Green's functions are utilized.

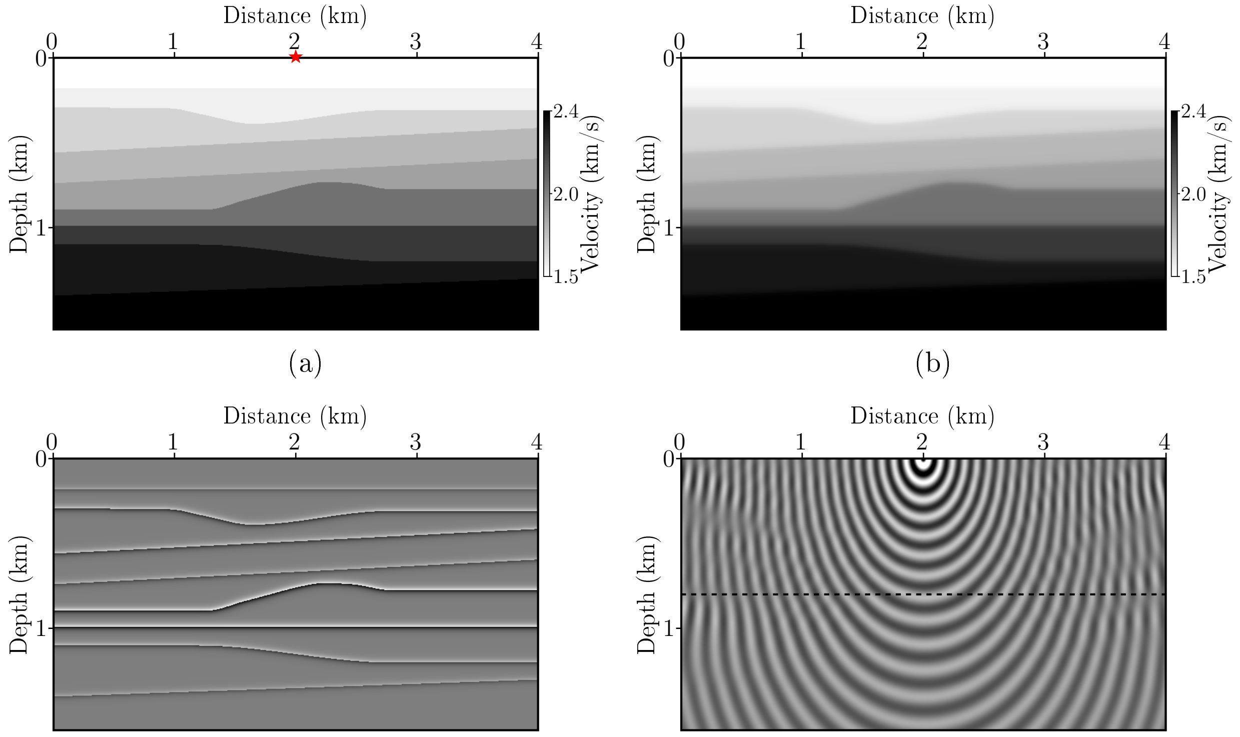

(a) (b)

(c) (d)

Figure 2.4: (a) Layered velocity model and its corresponding (b) background velocity model and (c) reflectivity model. The gray scale used in panels (a) and (b) is the same and is shown to the right of the first row. (d) Real part of the 15 Hz Green's function with source location at $\mathbf{x}_s = (2000, 0)$m (see red star in Figure 2.4a).

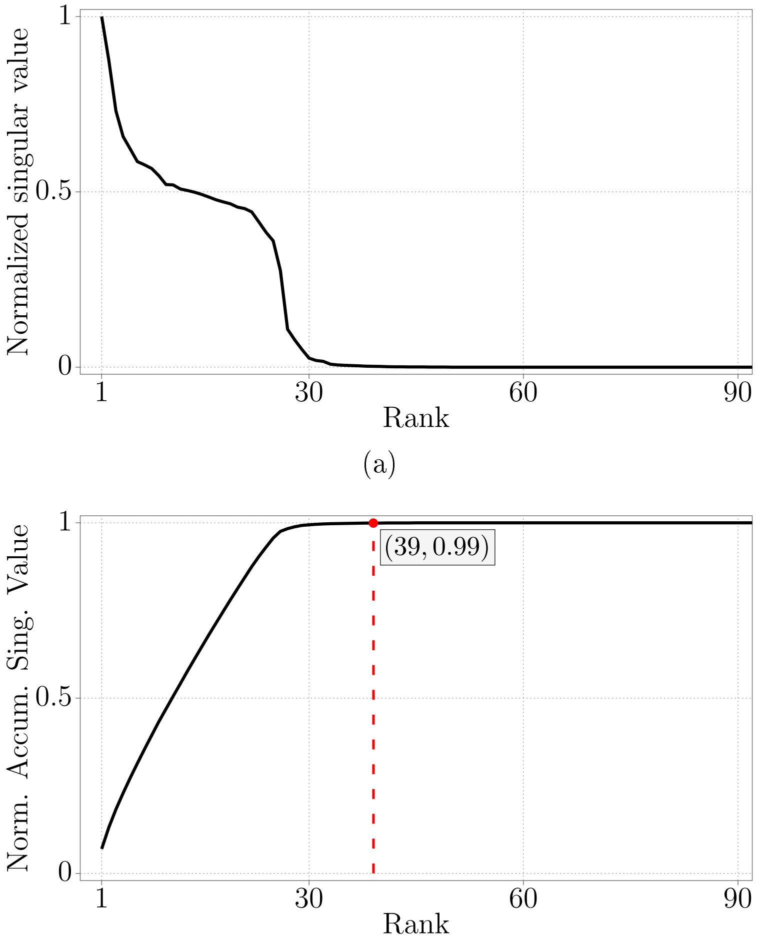

(a)

(b)

Figure 2.5: (a) Distribution of the normalized singular values and (b) normalized accumulated singular values of the 15 Hz Green's function.

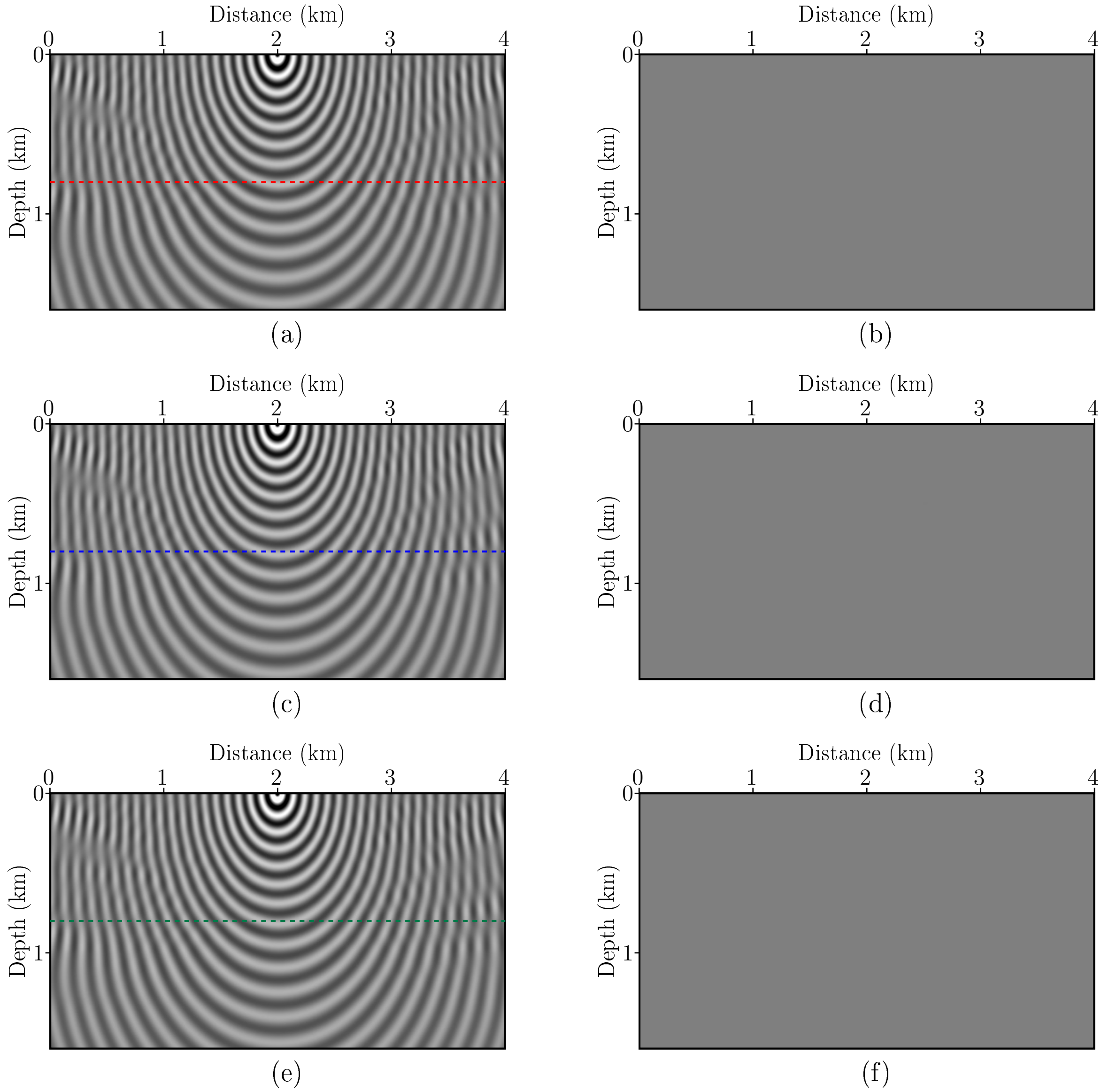

Figure 2.6: Real component of the reconstructed 15 Hz Green's function from its low-rank representation using (a) conventional, (c) rSVD, and (e) cSVD algorithms. The right column shows their corresponding differences with respect to the reference Green's function (Figure 2.4d). The clip level is the same for all panels. The colored dashed lines indicate the traces selected for the plot in Figure 2.7a.

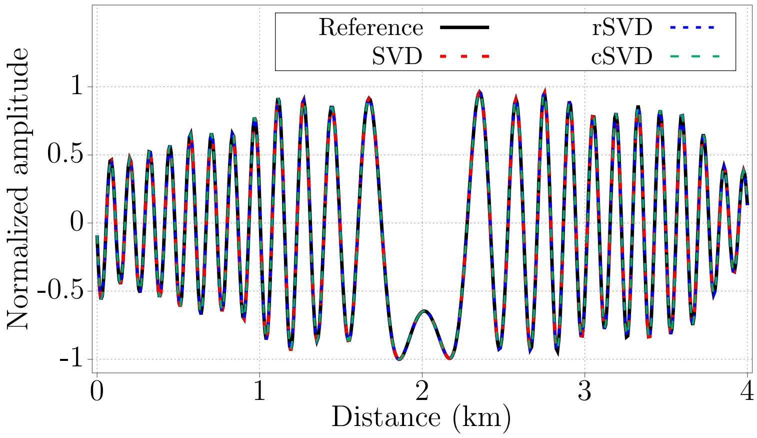

(a)

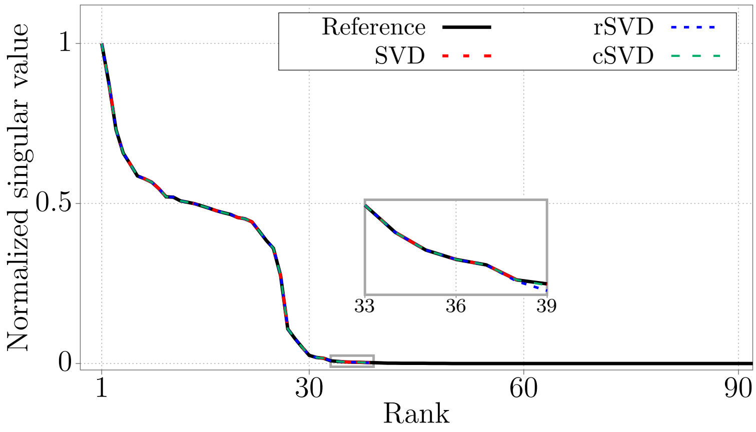

(b)

Figure 2.7: (a) Wiggle traces comparing the horizontal profiles extracted from the real part of the reference (black line in Figure 2.4d) and the reconstructed (colored dashed lines in Figure 2.6a-c) 15 Hz Green's function. (b) Distribution of singular values for the low-rank representation of the 15 Hz Green's function using conventional and stochastic SVD algorithms.

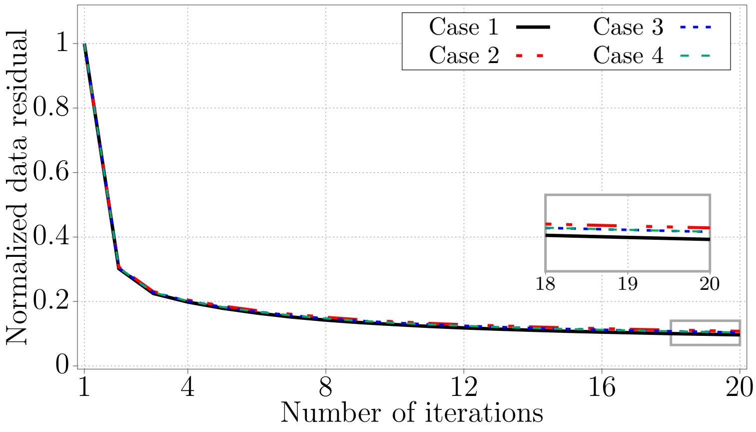

Figure 2.8: Convergence curves of the normalized data misfits of different FLSRTM algorithms for the layered model.

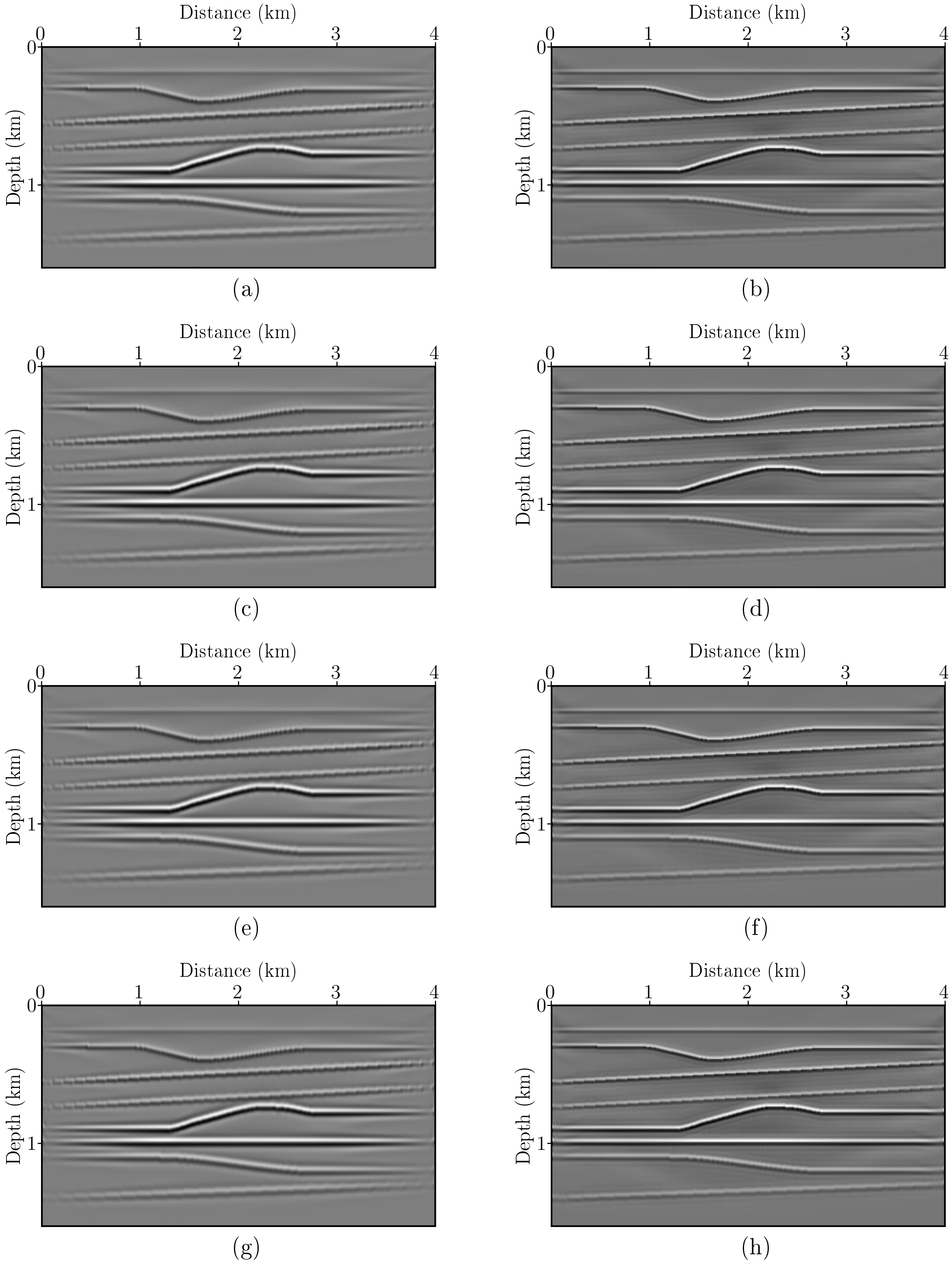

Figure 2.9: RTM and FLSRTM results for: (a)-(b) case 1, (c)-(d) case 2, (e)-(f) case 3 and (g)-(h) case 4.

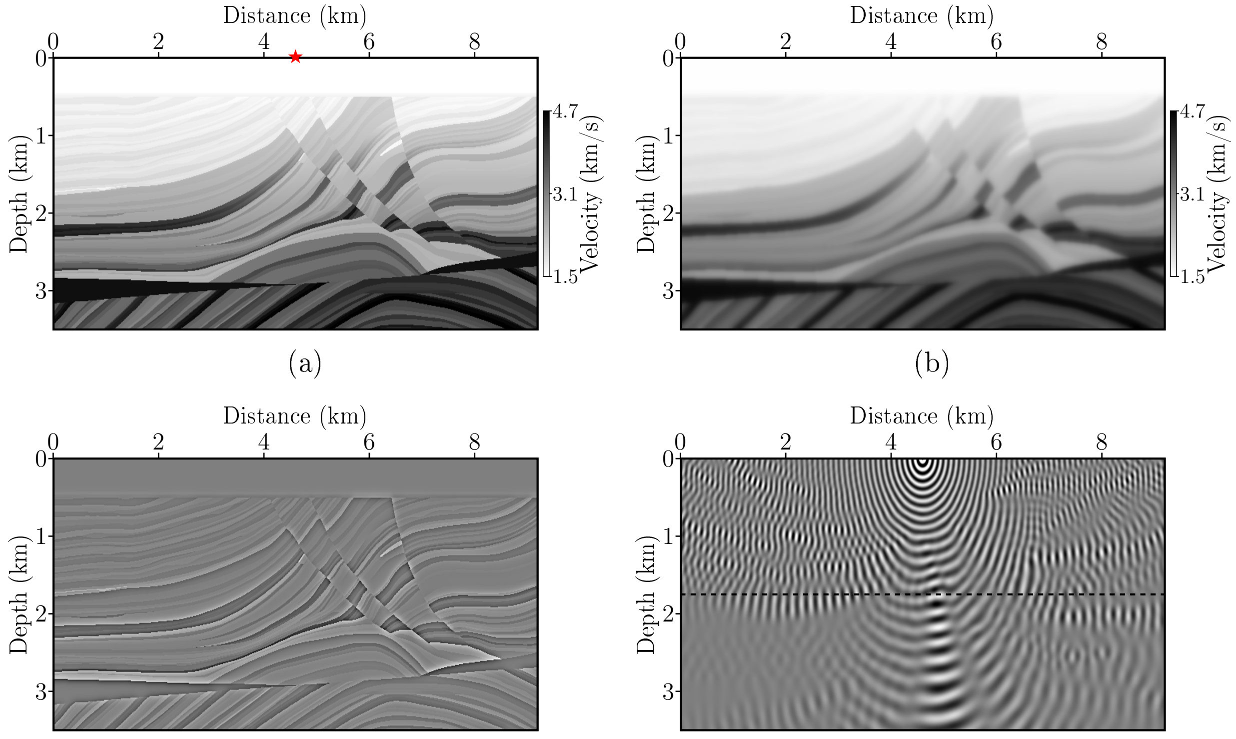

(a) (b)

(c) (d)

Figure 2.10: (a) The Marmousi-2 velocity model and its corresponding (b) background velocity model and (c) reflectivity model. The gray scale used in panels (a) and (b) is the same and is shown to the right of the first row. (d) Real part of the 15 Hz Green's function with source location at $\mathbf{x}_s = (4.6, 0)$km (see red star in Figure 2.10a).

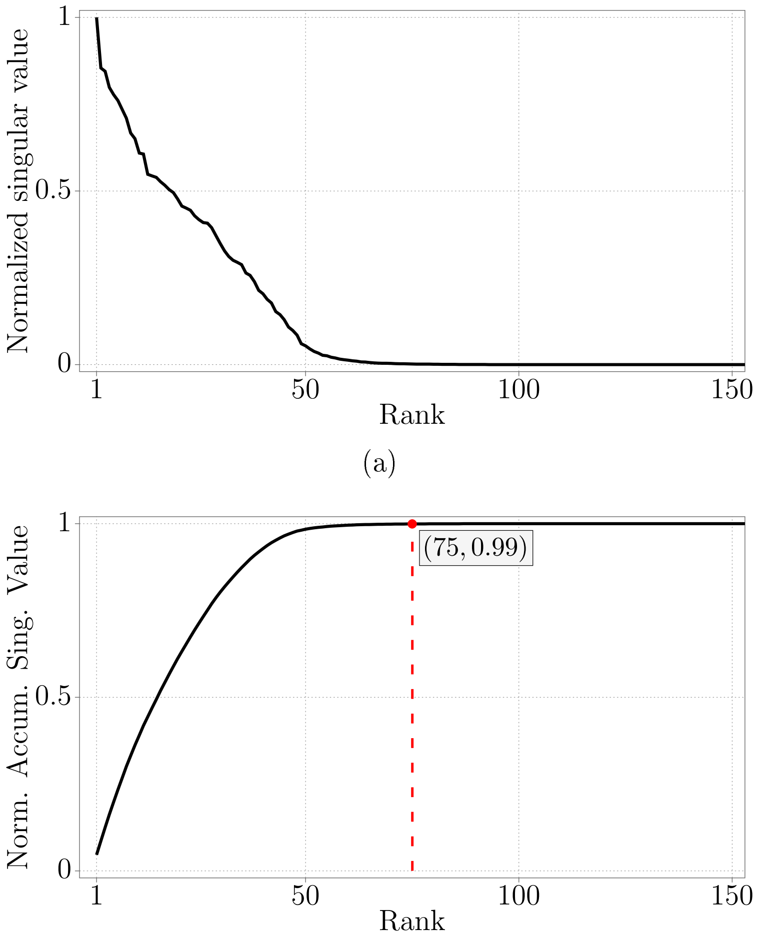

(a)

(b)

Figure 2.11: (a) Distribution of the normalized singular values and (b) normalized accumulated singular values of the 15 Hz Green's function.

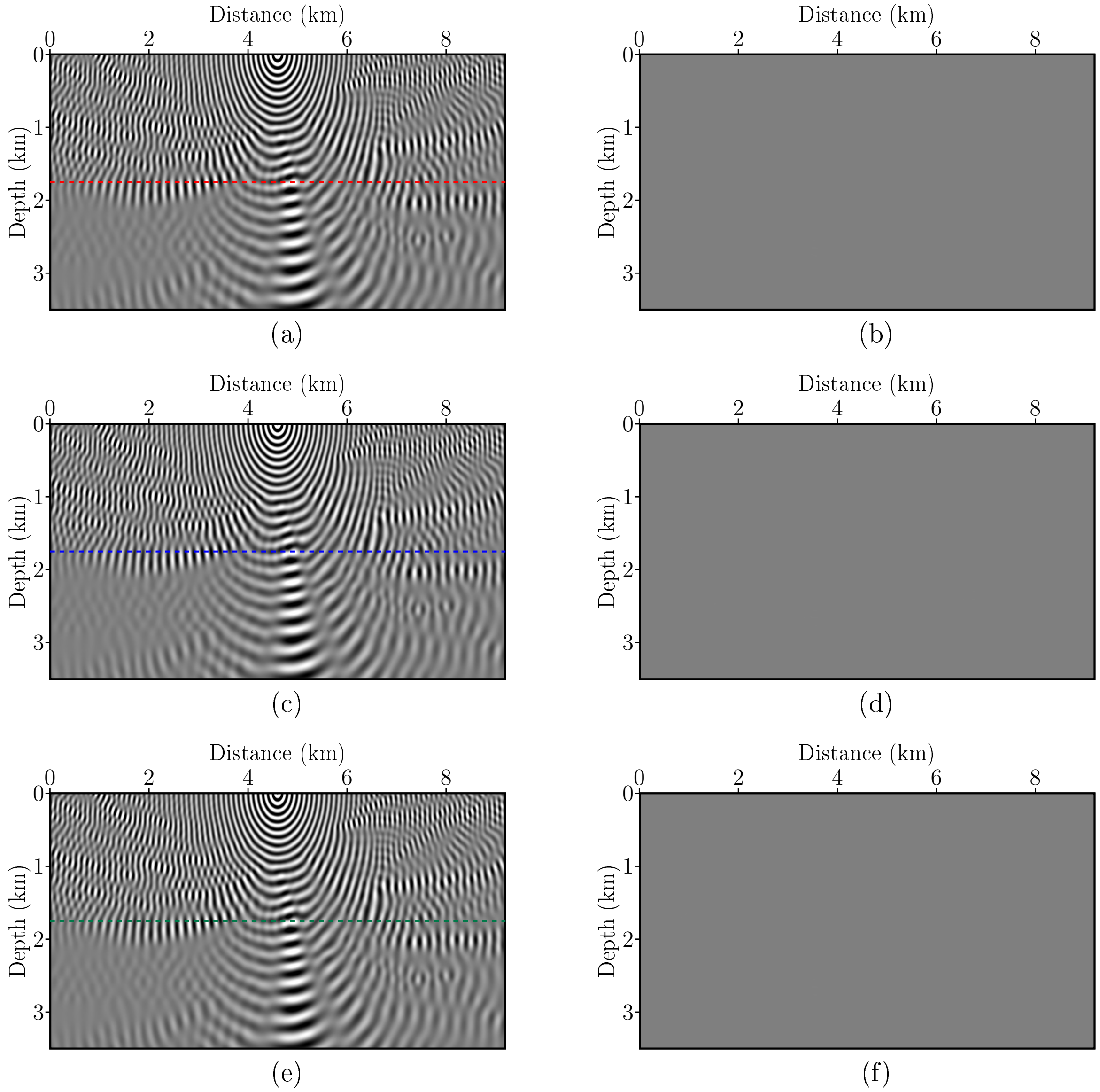

Figure 2.12: Real component of the reconstructed 15 Hz Green's function from its low-rank representation using (a) conventional, (c) rSVD, and (e) cSVD algorithms. The right column shows their corresponding differences with respect to the reference Green's function (Figure 2.10d). The clip level is the same for all panels. The colored dashed lines indicate the traces selected for the plot in Figure 2.13a.

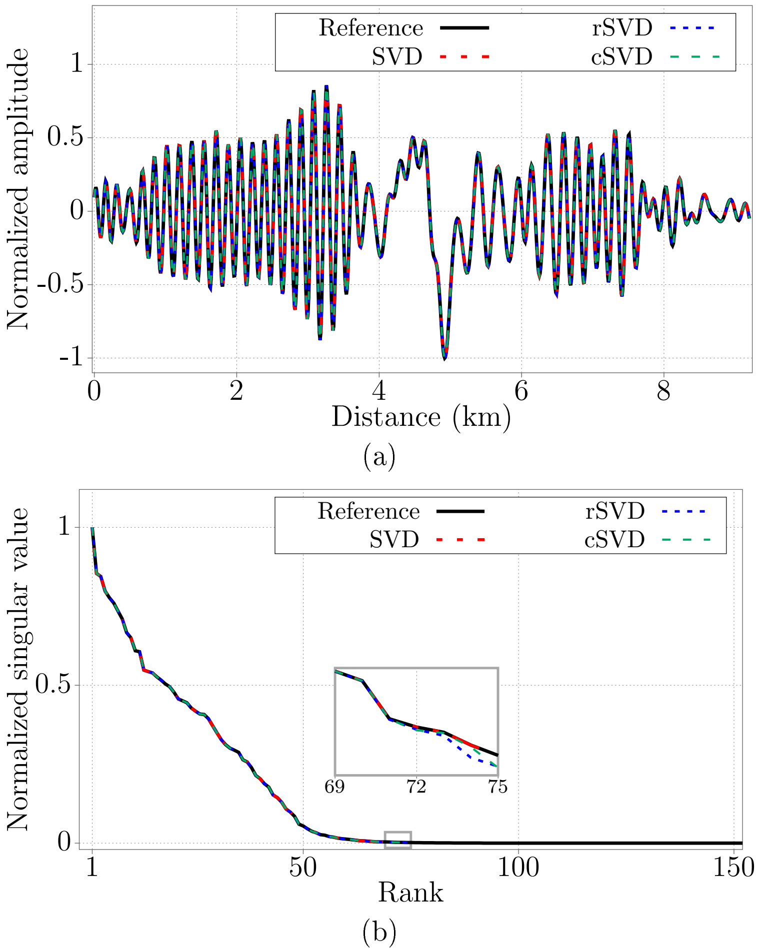

Figure 2.13: (a) Wiggle traces comparing the horizontal profiles extracted from the real part of the reference (black line in Figure 2.10d) and the reconstructed (colored dashed lines in Figure 2.12a-c) 15 Hz Green's function. (b) Distribution of singular values for the low-rank representation of the 15 Hz Green's function using conventional and stochastic SVD algorithms.

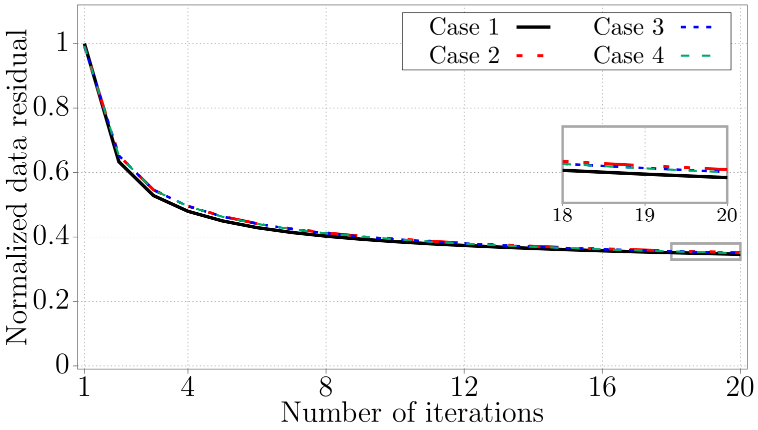

Figure 2.14: Convergence curves of the normalized data misfits of different FLSRTM algorithms for the Marmousi model.

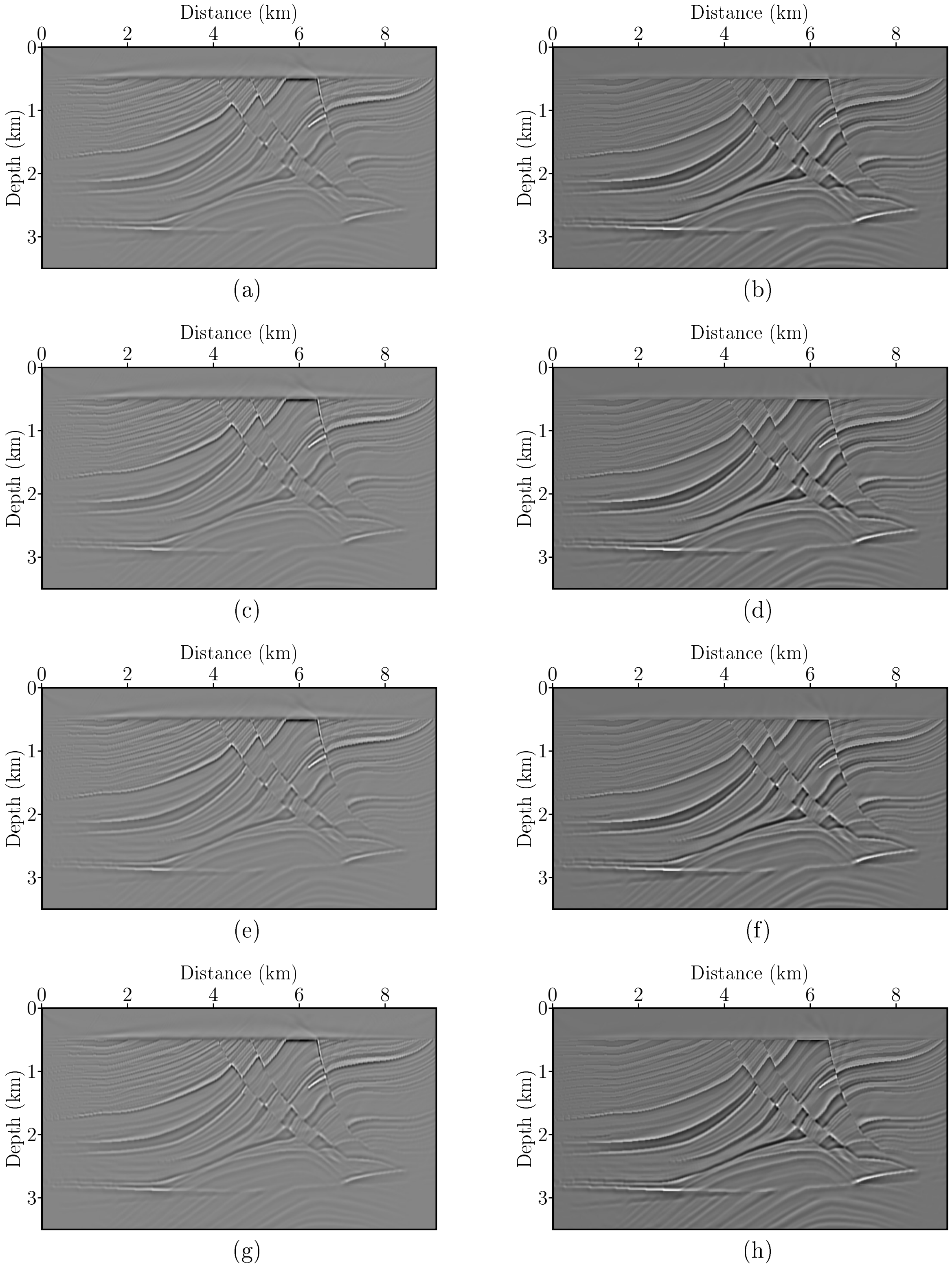

(a) (b)

(c) (d)

(e) (f)

(g) (h)

Figure 2.15: RTM and FLSRTM results for: (a)-(b) case 1, (c)-(d) case 2, (e)-(f) case 3 and (g)-(h) case 4.

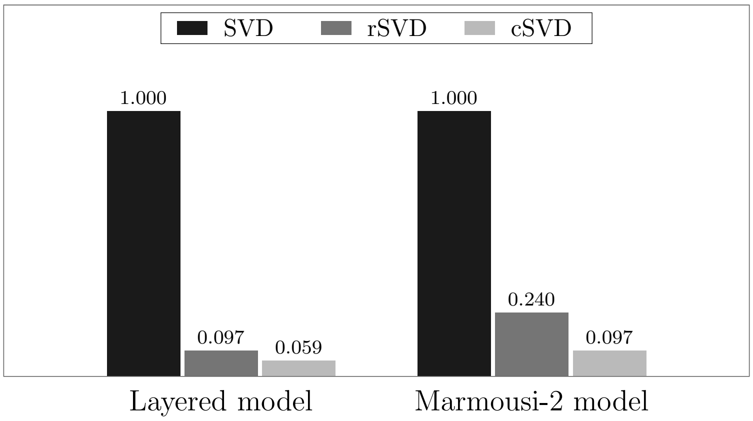

(a)

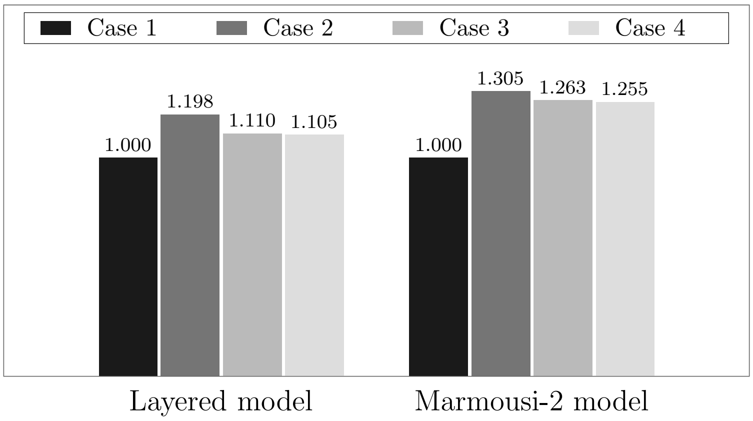

(b)

Figure 2.16: (a) Normalized time required to construct the low-rank representation of the 15 Hz Green's function using the three implemented SVD algorithms. (b) Total normalized time required to execute the FLSRTM scheme.

References

Albano, N. A.; Costa, J. C. and Schleicher, J. (2019) Migração por mínimos quadrados usando condição de imagem com amplitude verdadeira: uma abordagem no domínio da imagem, in: *15th International Congress of the Brazilian Geophysical Society & EXPOGEF*, Brazilian Geophysical Society.

Anderson, E.; Bai, Z.; Bischof, C.; Blackford, S.; Demmel, J.; Dongarra, J.; Du Croz, J.; Greenbaum, A.; Hammarling, S.; McKenney, A. and Sorensen, D. (1999) LAPACK Users' Guide, SIAM, 3rd edn..

Andrade, P.; Pestana, R. and Revelo, D. E. (2017) Reverse time migration in the frequency domain by the rapid expansion method, Brazilian Journal of Geophysics, **35**(4):287–306.

Bamberger, A.; Chavent, G.; Hemon, C. and Lailly, P. (1982) Inversion of normal incidence seismograms, Geophysics, **47**(5):757–770.

Baysal, E.; Kosloff, D. D. and Sherwood, J. W. C. (1983) Reverse time migration, Geophysics, **48**(11):1514–1524.

Born, M. and Wolf, E. (1999) Principles of Optics: Electromagnetic Theory of Propagation, Interference, and Diffraction of Light, Cambridge University Press.

Claerbout, J. (1992) Earth Soundings Analysis: Processing Versus Inversion, Blackwell Scientific Publications.

Dai, W. and Schuster, G. T. (2013) Plane-wave least-squares reverse-time migration, Geophysics, **78**(4):S165–S177.

Dai, W.; Fowler, P. and Schuster, G. T. (2012) Multi-source least-squares reverse time migration, Geophysical Prospecting, **60**(4):681–695.

Dong, S.; Cai, J.; Guo, M.; Suh, S.; Zhang, Z.; Wang, B. and Li, Z. (2012) Least-squares reverse time migration: towards true amplitude imaging and improving the resolution, in: *82nd Annual International Meeting, SEG, Expanded Abstracts*, pp. 1–5.

Dutta, G. and Schuster, G. T. (2014) Attenuation compensation for least-squares reverse time migration using the viscoacoustic-wave equation, Geophysics, **79**(6):S251–S262.

Erichson, N. B.; Brunton, S. L. and Kutz, J. N. (2017) Compressed Singular Value Decomposition for Image and Video Processing, in: *2017 IEEE International Conference on Computer Vision Workshops (ICCVW)*, pp. 1880–1888.

Erichson, N. B.; Voronin, S.; Brunton, S. L. and Kutz, J. N. (2019) Randomized Matrix Decompositions Using R, Journal of Statistical Software, **89**(11):1–48.

Etgen, J.; Gray, S. H. and Zhang, Y. (2009) An overview of depth imaging in exploration geophysics, Geophysics, **74**(6):WCA5–WCA17.

Golub, G. and Van Loan, C. (1996) Matrix Computations, Johns Hopkins University Press, 3rd edn..

Gu, M. (2015) Subspace Iteration Randomization and Singular Value Problems, SIAM Journal on Scientific Computing, **37**(3):1139–1173.

Halko, N.; Martinsson, P. G. and Tropp, J. A. (2011) Finding structure with randomness: Probabilistic algorithms for constructing approximate matrix decompositions, SIAM Review, **53**(2):217–288.

Halko, N. P. (2012) Randomized methods for computing low-rank approximations of matrices, Ph.D. thesis, USA.

Herrmann, F. J. and Li, X. (2012) Efficient least-squares imaging with sparsity promotion and compressive sensing, Geophysical Prospecting, **60**(4):696–712.

Ji, H. and Li, Y. (2014) GPU Accelerated Randomized Singular Value Decomposition and Its Application in Image Compression, in: *Modeling, Simulation, and Visualization Student Capstone Conference*.

Kim, S.; Kim, Y. S. and Chung, W. (2022) Fast and memory-efficient frequency domain least-squares reverse time migration using singular value decomposition (SVD), IEEE Transactions on Geoscience and Remote Sensing, **60**:1–11.

Kumar, A.; Rastogi, R.; Srivastava, A. and Mahajan, B. (2023) RTM Image Conditioning Using Deep Learning, in: *84th EAGE Annual Conference & Exhibition*, pp. 1–5.

Levin, S. A. (1984) Principle of reverse-time migration, Geophysics, **49**(5):581–583.

Lippmann, B. A. and Schwinger, J. (1950) Variational Principles for Scattering Processes. I, Phys. Rev., **79**(3):469–480.

Liu, Q. and Peter, D. (2018) One-step data-domain least-squares reverse time migration, Geophysics, **83**(4):R361–R368.

Liu, Q. and Peter, D. (2020) Square-Root Variable Metric-Based Nullspace Shuttle: A Characterization of the Nonuniqueness in Elastic Full-Waveform Inversion, Journal of Geophysical Research: Solid Earth, **125**(2).

Liu, Y.; Wu, Z.; Kang, H. and Yang, J. (2020) Use of prismatic waves in full-waveform inversion with the exact Hessian, Geophysics, **85**(4):R325–R337.

Liu, Y.; Liu, W.; Wu, Z. and Yang, J. (2022) Reverse time migration with an exact two-way illumination compensation, Geophysics, **87**(2):S53–S62.

Mahoney, M. W. (2011) Randomized Algorithms for Matrices and Data, Foundations and Trends in Machine Learning, **3**(2):123–224.

Martin, G. S.; Wiley, R. and Marfurt, K. J. (2006) Marmousi2: An elastic upgrade for Marmousi, The Leading Edge, **25**(2):156–166.

Martinsson, P.-G. (2019) Randomized methods for matrix computations.

Martinsson, P.-G.; Rokhlin, V. and Tygert, M. (2011) A randomized algorithm for the decomposition of matrices, Applied and Computational Harmonic Analysis, **30**(1):47–68.

McMechan, G. A. (1983) Migration by extrapolation of time-dependent boundary values, Geophysics Prospecting, **31**(3):413–420.

Morse, P. and Feshbach, H. (1953) Methods of Theoretical Physics, International series in pure and applied physics, McGraw-Hill.

Nemeth, T.; Wu, C. and Schuster, G. T. (1999) Least-squares migration of incomplete reflection data, Geophysics, **64**(1):208–221.

Pestana, R. C. and Stoffa, P. L. (2010) Time evolution of the wave equation using rapid expansion method, Geophysics, **75**(4):T121–T131.

Ren, H.; Wang, H. and Chen, S. (2013) Least-squares reverse time migration in frequency domain using the adjoint-state method, Journal of Geophysics and Engineering, **10**(3).

Rokhlin, V.; Szlam, A. and Tygert, M. (2010) A Randomized Algorithm for Principal Component Analysis, SIAM Journal on Matrix Analysis and Applications, **31**(3):1100–1124.

Sarlos, T. (2006) Improved Approximation Algorithms for Large Matrices via Random Projections, in: *47th Annual IEEE Symposium on Foundations of Computer Science*, pp. 143–152, IEEE.

Schuster, G. (2017) Seismic Inversion, Investigations in Geophysics, Society of Exploration Geophysicists.

Schuster, G. T. (1993) Least-squares cross-well migration, in: *63rd Annual International Meeting, SEG, Expanded Abstracts*, pp. 110–113.

Shin, C.; Yoon, K.; Marfurt, K. J.; Park, K.; Yang, D.; Lim, H. Y.; Chung, S. and Shin, S. (2001) Efficient calculation of a partial-derivative wavefield using reciprocity for seismic imaging and inversion, Geophysics, **66**(6):1856–1863.

Shoja, A.; van der Neut, J. and Wapenaar, K. (2022) Target-oriented least-squares reverse-time migration using Marchenko double-focusing: reducing the artefacts caused by overburden multiples, Geophysical Journal International, **233**(1):13–32.

Symes, W. W. (2009) The seismic reflection inverse problem, Inverse Problems, **25**(12):123008.

Tarantola, A. (1984) Inversion of seismic reflection data in the acoustic approximation, Geophysics, **49**:1942–2156.

Tropp, J. A. and Webber, R. J. (2023) Randomized algorithms for low-rank matrix approximation: Design, analysis, and applications.

Whitmore, N. D. (1983) Iterative depth migration by backward time propagation, in: *53rd Annual International Meeting, SEG, Expanded Abstracts*, pp. 382–385.

Wong, M.; Ronen, S. and Biondi, B. (2012) Least-squares reverse time migration/inversion for ocean bottom data: A case study, in: *81st Annual International Meeting, SEG, Expanded Abstracts*, pp. 2369–2373.

Woodward, M. J. (1992) Wave-equation tomography, Geophysics, **57**(1):15–26.

Xue, Z.; Chen, Y.; Fomel, S. and Sun, J. (2016) Seismic imaging of incomplete data and simultaneous-source data using least-squares reverse time migration with shaping regularization, Geophysics, **81**(1):S11–S20.

Yao, G. and Jakubowicz, H. (2016) Least-squares reverse-time migration in a matrix-based formulation, Geophysical Prospecting, **64**(3):611–621.

Yao, G.; Wu, B.; da Silva, N. V.; Debens, H. A.; Wu, D. and Cao, J. (2022) Least-squares reverse time migration with a multiplicative Cauchy constraint, Geophysics, **87**(3):S151–S167.

Zhang, Y.; Duan, L. and Xie, Y. (2015) A stable and practical implementation of least-squares reverse time migration, Geophysics, **80**:V23–V31.

Zhao, Z. and Sen, M. K. (2019) Frequency-domain double-plane-wave least-squares reverse time migration, Geophysical Prospecting, **67**(8):2061–2084.

Zhou, H.; Chen, S. and Ren, H. (2014) One-way wave equation least-squares migration based on illumination compensation, Chinese Journal of Geophysics, **57**(5):726–738.

3

One-Way Wave-Equation Migration Based on Jacobi-Anger Expansion in Arbitrarily Lateral Varying Media

This chapter has been submitted as Daniel E. Revelo and Reynam C. Pestana. *One-Way Wave-Equation Migration Based on Jacobi-Anger Expansion in Arbitrarily Lateral Varying Media* to IEEE Transactions on Geoscience and Remote Sensing. Minor modifications have been applied to maintain consistency within this thesis.

Abstract

Seismic depth migration by downward continuation using conventional one-way wave-equation operators has three main shortcomings: handling evanescent waves, imaging large angles, and stability of the one-way propagator. Conventional one-way wave-equation propagators have been extensively constructed using approximation theories, such as Taylor series and other expansions. Although in these, a new operator is calculated at each lateral point of the grid, difficulties persist due to the assumption that the medium is locally homogeneous. Consequently, these propagators exhibit significant weaknesses in imaging complex media. To alleviate these drawbacks, we propose a stable and affordable approach to the one-way wave-equation depth migration algorithm. First, we use a spectral projector to suppress evanescent modes in an arbitrarily laterally varying velocity model. Next, we apply a coupled Schulz iteration scheme to the Helmholtz operator to obtain the square-root operator. Finally, to address the issue of accurately constructing the extrapolation operator while ensuring stability, we introduce a novel algorithm to approximate the exponential matrix operator using the Jacobi-Anger expansion. This approximation enables the one-way wave-equation propagator to be constructed solely through matrix multiplication, a feature that facilitates efficient implementation and execution. Through an impulse response test, we demonstrate that our proposed migration algorithm is more accurate than the one using Taylor series expansion and is effective for large angles in media with pronounced lateral velocity variations. We also use models with complex subsurface structures and field data to demonstrate that our approach performs better at imaging intricate and fine-scale features compared to traditional one-way migration methods.

Introduction

The one-way wave equation is derived from an approximate solution of the two-way wave equation and is central to the recursive extrapolation approach in wave-equation migration (WEM)(Claerbout, 1971). It decomposes the full wave equation along the dominant direction of wave propagation, thereby reducing the computational dimensionality. Consequently, the WEM method holds a significant advantage in large-scale problems. Unlike reverse time migration (RTM) (Baysal et al., 1983; McMechan, 1983; Whitmore, 1983; Levin, 1984), WEM can only provide accurate phases and amplitudes within limited propagation angles, especially in media with strong velocity contrasts and steeply dipping reflectors. While RTM is studied intensively across industries and academia, it has shortcomings, e.g., high memory costs and low-frequency artifacts, that could be mitigated by WEM.

One-way wave propagators, as part of a full wave equation separation migration method, provide a reliable kinematic solution for acoustic waves. This factorization of the two-way wave equation into upgoing and downgoing operators introduces the square-root operator (or vertical wavenumber), characterized by its non-locality. Although many kinds of wide-angle one-way wave-equation methods have been developed to approximate the square-root operator with a local operator, their accuracy is still limited. Conventional WEM algorithms include the phase shift and the phase shift plus interpolation (PSPI) migration methods (Gazdag, 1978; Gazdag and Sguazzero, 1984), the split step (SS) migration method (Stoffa et al., 1990), and the Fourier finite-difference (FFD) technique (Ristow and Rühl, 1994). Another branch within conventional one-way propagators is to expand the square-root operator directly, without introducing any background, using mathematical approximations such as Taylor and Padé series, as well as Chebyshev polynomials (Gazdag, 1978; Gazdag and Sguazzero, 1984; Stoffa et al., 1990). The truncation errors produced by these approaches to approximate the square-root operator limit the imaging angle, making it very difficult to achieve 90°. This restriction on the imaging angle is a significant drawback of WEM. To fully leverage the advantages of the unidirectional wave equation, it is imperative to eschew conventional methodologies that employ approximate polynomial expressions for the computation of the matrix square root. In the literature, two notable and successfully tested approximation-free methods have been proposed: an eigenvalue decomposition method (Grimbergen et al., 1998) and the coupled Schulz iteration scheme (Higham, 1987), which is based on the relationship between the matrix sign function and its square root. Given that the eigenvalue decomposition method is time-consuming (You et al., 2018), we have opted to use Higham's scheme to compute the vertical wavenumber in our proposed WEM algorithm.

Another issue present in the implementation of the one-way imaging algorithm is the notorious instability in the depth extrapolation propagator, which arises from the presence of evanescent wave components (Grimbergen et al., 1998; Wapenaar and Grimbergen, 1998). Kosloff and Baysal (1983) propose suppressing evanescent waves in the wavenumber domain for a background with depth-only dependent velocity using the Fourier transform and a simple ideal cutoff filter. For a general variable background, they suggest employing a cutoff filter adjusted to the maximum velocity at a given depth level, also relying on the Fourier transform as a tool. As demonstrated by Thorbecke et al. (2004), the application of this cutoff filter can be extended to the one-way wave equation without any loss of generality. Numerical examples demonstrate that for full-wave-equation depth extrapolation in migration, this strategy results in the removal of some propagating waves along with the evanescent waves, leading to poor imaging of steep reflectors (Sandberg and Beylkin, 2009). As an alternative, one of the most promising methods is the spectral projector (Kenney and Laub, 1995), which can filter out evanescent waves without losing any propagating wave components. For depth-dependent backgrounds, the combination of the Fourier transform and the ideal cutoff filter, as proposed by Kosloff and Baysal (1983), constitutes such a projector. In this paper, we implemented an algorithm for computing the spectral projectors that leverages their relationship with the sign function of a matrix, which in turn uses matrix polynomial recursions (Auslander and Tsao, 1992; You et al., 2019).

In our proposed WEM algorithm, we avoid the assumption that the square-root operator corresponds to a local operator. As a result, the depth extrapolator can no longer be applied locally and must be implemented as an exponential matrix operator. While numerous researchers have focused on the computation of the square-root operator and the attenuation of evanescent waves, few have given attention to constructing this exponential matrix operator. You et al. (2019) used the Taylor series (TS) expansion to approximately compute the exponential function of a matrix. However, in this paper, we propose using the Jacobi-

Anger (JA) expansion as a more efficient alternative for this purpose. The JA expansion inherently represents oscillatory functions more naturally, making it particularly well-suited for applications involving wave propagation, such as seismic depth extrapolation. This expansion converges more rapidly due to the properties of Bessel functions, which decreases the number of terms needed for an accurate approximation (Watson, 1944). Additionally, the orthogonality of Bessel functions minimizes cross-interference between terms, further enhancing the precision and compactness of the representation (Abramowitz and Stegun, 1972). Consequently, the JA expansion not only provides a more exact approximation with fewer terms but also results in significant computational efficiency and accuracy in numerical simulations (Bowman, 1958).

The aim of this paper is to delineate the integration of the spectral projector, the coupled Schulz iteration scheme, and the JA expansion into the WEM framework to overcome the inherent limitations in conventional approaches for solving one-way wave equations. The structure of this article is as follows: Initially, a brief overview of the one-way wave equations is presented. This is followed by an introduction to the spectral projector and the coupled Schulz iteration scheme. Thereafter, the proposed JA expansion is elucidated, which serves to approximate the exponential matrix operator. To validate the efficacy of the proposed scheme within the WEM method, impulse responses were computed employing both the TS and JA expansions, as well as conventional WEM algorithms. Moreover, to procure better and more detailed imaging results, post-stack and pre-stack migrations were executed for complex subsurface models using both conventional WEM methods and the proposed one-way migration algorithm. Finally, we applied these migration methods to real seismic data for comparison.

Methodology

Acoustic one-way propagators

Assuming a 3D isotropic medium with constant density, the one-way wave equations for downgoing $\hat{p}_d$ and upgoing $\hat{p}_u$ continuation of the acoustic wavefield, in the Fourier domain, are written as (Wapenaar, 1990; Claerbout, 1985; Mulder and Plessix, 2004)

$$\begin{cases} \left(\dfrac{\partial}{\partial z} + ik_z\right)\hat{p}_d(\mathbf{x}, z, \omega) = 0, \\ \hat{p}_d(\mathbf{x}, z = 0, \omega) = F(\omega)\delta(\mathbf{x} - \mathbf{x}_s), \end{cases} \tag{3.1}$$

and

$$\begin{cases} \left(\dfrac{\partial}{\partial z} - ik_z\right)\hat{p}_u(\mathbf{x}, z, \omega) = 0, \\ \hat{p}_u(\mathbf{x}, z = 0, \omega) = \hat{d}(\mathbf{x}, \omega), \end{cases} \tag{3.2}$$

where z and $\mathbf{x} = (x, y)$ are the coordinates of depth and the two lateral dimensions, respectively, and $i = \sqrt{-1}$ is the imaginary unit. $F(\omega)$ represents the spectrum of the source term injected at the vector position $\mathbf{x}_s$, $\hat{d}(\mathbf{x}, \omega)$ is the recorded seismic data in the frequency domain and ω is the angular frequency. The generalized solution of equations 3.1 and 3.2 allows us to obtain an extrapolation scheme in depth for the acoustic wavefield

$$\hat{p}_{d,u}(\mathbf{x}, z + \Delta z, \omega) = \hat{p}_{d,u}(\mathbf{x}, z, \omega)e^{\pm ik_z\Delta z}, \tag{3.3}$$

where

$$k_z = \left[\frac{\omega^2}{v^2(\mathbf{x})} + \frac{\partial^2}{\partial x^2} + \frac{\partial^2}{\partial y^2}\right]^{1/2} \tag{3.4}$$

corresponds to the square-root operator, also known as the vertical wavenumber, $v(\mathbf{x})$ is the velocity, and Δz is the vertical grid space of the medium.

From equations 3.3 and 3.4 it is evident that the implementation of one-way propagators necessitates the construction of the square-root operator and the calculation of the exponential matrix operator. However, before detailing the adopted methodologies for these two stages of the depth extrapolation scheme, it is crucial to address an inherent issue within the Helmholtz operator $L(\equiv k_z^2)$. Next, the stability problem associated with it will be elucidated, followed by a discussion of the selected algorithm to mitigate this drawback.

Treatment of evanescent waves via spectral projectors

To simplify our discussion, we consider a 2D case, where the medium is discretized onto a $nz \times nx$ mesh. We then represent the Helmholtz operator L, for a single depth level and at a specific frequency, as a square $nx \times nx$ matrix

$$L = \frac{\omega^2}{v^2(x)} + \frac{\partial^2}{\partial x^2}, \tag{3.5}$$

with

$$\frac{\omega^2}{v^2(x)} = \begin{bmatrix} \dfrac{\omega^2}{v^2(x_1)} & 0 & \cdots & 0 \\ 0 & \dfrac{\omega^2}{v^2(x_2)} & \cdots & 0 \\ \vdots & \vdots & \ddots & \vdots \\ 0 & 0 & \cdots & \dfrac{\omega^2}{v^2(x_{nx})} \end{bmatrix} \quad \text{and} \quad \frac{\partial^2}{\partial x^2} = \frac{1}{\Delta x^2}\begin{bmatrix} -2 & 1 & 0 & \cdots & 0 \\ 1 & -2 & 1 & \cdots & 0 \\ 0 & 1 & -2 & \cdots & 0 \\ \vdots & \vdots & \vdots & \ddots & \vdots \\ 0 & 0 & \cdots & 1 & -2 \end{bmatrix},$$

where Δx is the horizontal grid space of the medium. In this discretization of operator L, a second-order finite-difference scheme is employed to compute the second-order partial derivative with respect to x. However, to enhance accuracy, it is advisable to use a higher-order finite-difference scheme instead. It is important to note that the matrical representation for L adeptly handles variations in lateral velocity along the horizontal direction due to its diagonal elements.

It is well known that when the vertical wavenumber involved in depth extrapolation propagators is a positive real number, it corresponds to a physically meaningful wave. Conversely, if k_z assumes a complex value, the magnitudes of the propagators may exhibit exponential amplification with increasing depth. In such instances, the resultant wave is classified as an evanescent wave. Given that evanescent waves induce instability in practical applications, their suppression is imperative during the depth extrapolation process. This instability originates from the indefinite character of operator L, which possesses both positive and negative eigenvalues (Sandberg and Beylkin, 2009; You et al., 2019). Positive eigenvalues correspond to propagating modes, while negative eigenvalues lead to an exponential growth of the wavefield during depth extrapolation (nonpropagating evanescent waves). Consequently, the depth stepping scheme defined in equation 3.3 becomes unstable.

To filter out the negative eigenvalues of operator L, the spectral projector involves only matrix multiplications as proposed by Kenney and Laub (1995)

$$\mathcal{P} = \frac{I + \operatorname{sign}(L)}{2} \tag{3.6}$$

is used in our implementation. The sign function is, in turn, computed with the Newton-Schulz method (Auslander and Tsao, 1992)

$$S_{k+1} = \frac{3}{2} S_k - \frac{1}{2} S_k^3, \qquad \text{for } k = 0, 1, 2, \ldots, \tag{3.7}$$

and initialized with $S_0 = L/\|L\|_2$. This method exhibits quadratic convergence rate, resulting in S_k approaching $\operatorname{sign}(L)$ (Higham, 2008). The projector performs on matrix L such that $\bar{L} = \mathcal{P}L$, preserving only the positive eigenvalues, $\lambda_k \geq 0$, where λ_k is the k-th eigenvalues of the matrix $\bar{L}$, and guaranteeing numerical stability during the depth extrapolation process. After addressing the evanescent waves, we proceed to introduce the algorithm used for constructing the square root of the filtered Helmholtz operator.

Construction of the square-root operator

The conventional one-way operators used in WEM typically employ a reference velocity for the horizontal direction, which can lead to inaccuracies in heterogeneous media. To address this, the common approach is to compute a new operator at each grid point. However, in the presence of strong lateral inhomogeneities, the structure of the propagator matrix departs from a Toeplitz form to one where each row consists of a different local convolutional operator (Li et al., 2024). This adjustment, which reduces the length of the conventional operator, aims to enhance the accuracy of handling lateral variations. Nonetheless, shorter operators can introduce numerical errors during propagation, particularly at large angles (Thorbecke et al., 2004).

To overcome this issue, and before computing the one-way extrapolator $e^{\pm ik_z\Delta z}$, the construction of the operator k_z must be performed in the space domain. In the literature, two methods are reported for directly computing the square root of the operator $\bar{L}$. You et al. (2018) and Li et al. (2024) have described constructing the square root of $\bar{L}$ via singular value decomposition (SVD). However, SVD can significantly increase computational time for large models. Alternatively, the coupled Schulz iteration scheme (Higham, 1987), which was successfully implemented by You et al. (2019) for one-way extrapolation, has been selected for our algorithm for WEM. Based on the definition of the matrix sign function and assuming the absence of negative eigenvalues, Higham (1987) proposed the following coupled iteration scheme to determine the square root of a given matrix

$$\begin{cases} Y_{k+1} = \frac{1}{2}Y_k(3I - Z_kY_k) \\ Z_{k+1} = \frac{1}{2}(3I - Z_kY_k)Y_k \end{cases} \quad \text{for } k = 0, 1, 2, \ldots, \tag{3.8}$$

with $Y_0 = \bar{L}$ and $Z_0 = I$, where I is the identity matrix. As can be seen, Higham's scheme involves only matrix multiplications, and after limited iterations, the convergence results are $Y_k \to \bar{L}^{1/2}$ and $Z_k \to \bar{L}^{-1/2}$. The convergence is typically fast, and the method is robust for a wide range of matrices (Higham, 2008). Moreover, implementing this method to calculate the square-root operator eliminates conventional approximations and prevents the generation of incorrect phase curves in media with strong lateral velocity variations (You et al., 2019). It is important to note that the elimination of negative eigenvalues from operator L is performed not only to filter out evanescent waves, but also to meet the prerequisites for applying the coupled Schulz iteration scheme. With the algorithms for attenuating evanescent waves and calculating the square-root operator defined, we now introduce the proposed method for calculating the extrapolator $e^{\pm ik_z\Delta z}$ from equation 3.3.

Calculation of the one-way propagator

As previously mentioned, when considering lateral inhomogeneities, the local application of the extrapolation operator becomes infeasible. This implies that it cannot be applied as a simple arithmetic product between the acoustic wavefield and the one-way propagator.

Consequently, the propagator $e^{\pm ik_z\Delta z}$ must be implemented as an exponential matrix operator in the space domain. In the work of You et al. (2019), it is proposed to approximate the propagator with a Taylor series (TS) expansion. However, this proposal does not consider that Δz can assume large values and, therefore, the operator approximation will lose accuracy. Morever, the TS expansion often requires numerous terms to achieve a precise approximation, which can lead to inefficiencies and computational challenges. To address these limitations, we propose to use the Jacobi-Anger (JA) expansion (Abramowitz and Stegun, 1972) to compute the exponential function of a matrix

$$e^{\pm ik_z\Delta z} \approx \sum_{n=0}^{M} \varepsilon_n J_n(R\Delta z)\mathcal{T}_n\left(\frac{\pm ik_z}{R}\right), \tag{3.9}$$

where $\varepsilon_0 = 1$ and $\varepsilon_n = 2$ if $n \neq 0$. The term J_n represents the Bessel function of order n, R corresponds to the maximum eigenvalue of L, i.e., $R = \omega_{\max}/v_{\min}$, and $\mathcal{T}$ are the Chebyshev polynomials – one notes that they satisfy the following recurrence relation

$$\mathcal{T}_{n+1}(\xi) = 2\xi\mathcal{T}_n(\xi) - \mathcal{T}_{n-1}(\xi), \tag{3.10}$$

which is initiated by

$$\mathcal{T}_0(\xi) = I \qquad \text{and} \qquad \mathcal{T}_1(\xi) = \xi. \tag{3.11}$$

Furthermore, to guarantee the convergence of the series, we must ensure that M is greater than $R\Delta z$. The JA expansion inherently captures the oscillatory nature of the exponential operator with fewer terms, providing an approximation with a very high degree of accuracy (Bowman, 1958). Theoretically, it has no limits on the value of Δz, since the number of terms directly depends on this value. This results in improved performance and reduced computational cost, making it a more suitable and robust choice for calculating the one-way propagators.

To verify the accuracy of the one-way extrapolator using the proposed expansion, we computed the approximation using TS and JA expansions in a 1500 m/s homogeneous velocity model. The grid step in the vertical direction is 10 m and the frequency component is 80 Hz. The phase $\phi(\equiv k_z\Delta z)$ is discretized over $[0,\, R\Delta z]$ with an interval of 3.35×10^{-2}. Figure 3.1 presents a comparison between the TS and JA expansions. In Figure 3.1a, $f(\phi)$ and $g(\phi)$ represent the seventh-order and ninth-order TS expansions, respectively, while $h(\phi)$ corresponds to the seventh-order JA expansion. Notably, the seventh-order TS expansion (dashed red line) exhibits significant discrepancies near the right edge of the phase values, indicating a poor fit in this region. As the order increases to the ninth-order TS expansion (dashed blue line), the fit improves, yet some misalignment remains evident. Conversely, the seventh-order JA expansion (dashed green line) demonstrates a remarkable agreement with the exact values (black line) across the entire range of phase values. This superior robustness and accuracy is highlighted in Figure 3.1b, where the absolute error for each approximation is plotted. To validate the accuracy of the approximation for the one-way extrapolator, we employed the normalized root-mean-square (NRMS) error metric. The NRMS error between the approximated operator and the reference values for the seventh-order TS, ninth-order TS, and seventh-order JA expansions was 2.10×10^{-1}, 6.73×10^{-2}, and 3.88×10^{-2}, respectively. For this example, the results indicate that the JA expansion provides a more reliable and precise approximation of the exponential operator, even with a lower-order expansion, compared to the TS expansion.

In summary, the implementation of our extrapolation algorithm for each depth is performed as follows: *i*) the Helmholtz operator L is constructed for each frequency component, *ii*) the spectral projector (equations 3.6-3.7) is applied to L to filter the negative eigenvalues, *iii*) the square-root operator k_z is obtained by applying the coupled Schulz iteration scheme (equation 3.8) and *iv*) the acoustic wavefield is extrapolated stably and free of evanescent energy by applying the one-way propagator computed using equation 3.9. To integrate our proposed algorithm into WEM, we adopted the cross-correlation imaging condition to update the image. A step-by-step summary of the presented shot-record migration imaging algorithm is shown below:

```
1. Initialize the migrated image $I = 0$
2. Loop for all depth steps $z_i$
3. Loop for all frequency components $\omega_j$
  (a) Compute the Helmholtz operator $L$
  (b) Remove the negative eigenvalues of $L$
  (c) Compute the square root operator $k_z$
      i. For all sources:
          i. Compute one-way propagator $e^{-ik_z\Delta z}$
          ii. Compute $\hat{p}_d(\mathbf{x}, z_i + \Delta z, \omega_j) = \hat{p}_d(\mathbf{x}, z_i, \omega_j)e^{-ik_z\Delta z}$
      ii. For all receivers:
          i. Compute one-way propagator $e^{ik_z\Delta z}$
          ii. Compute $\hat{p}_u(\mathbf{x}, z_i + \Delta z, \omega_j) = \hat{p}_u(\mathbf{x}, z_i, \omega_j)e^{ik_z\Delta z}$
      iii. Apply the cross-correlation imaging condition:
          $I(\mathbf{x}, z_i + \Delta z, \omega_j) = I(\mathbf{x}, z_i + \Delta z, \omega_j) + \hat{p}_d^*(\mathbf{x}, z_i + \Delta z, \omega_j)\hat{p}_u(\mathbf{x}, z_i + \Delta z, \omega_j)$
```

Numerical tests

In this section, we conduct several numerical experiments to demonstrate the performance of our proposed WEM scheme, which uses the JA expansion to calculate the one-way propagator for generating migrated sections. Additionally, we compare the results from our WEM algorithm with those from the conventional PSPI and SS one-way migration methods, as implemented in the Seismic Unix software package (Stockwell, 1999). For all tests, we used a tenth-order finite-difference scheme to approximate the spatial derivative along the horizontal axis, and a horizontal taper (Cerjan et al., 1985) was applied to the wavefield at the left and right boundaries to suppress wavefield wraparound caused by periodic boundary conditions during depth extrapolation. Based on our multiple experiments with models of varying complexity, constructing the spectral projector typically requires about 25-30 iterations, whereas computing the square-root operator generally takes around 15-20 iterations. Moreover, as suggested by Miao et al. (2014), although the result of the depth-stepping migration is essentially clean with no significant artifacts, we applied a first-order finite-difference filtering in the vertical direction to enhance migrated images.

Impulse response test

To validate the proposed JA expansion in the construction of the one-way propagator, we start by studying its impulse response in a medium with a strong lateral velocity variation, given by $v(x,z) = (1500 + 2x + z)\,\mathrm{m/s}$ and shown in Figure 3.2a. The model consists of 301×301 grid nodes with a $5\,\mathrm{m}$ grid spacing. A Ricker pulse with a peak frequency of $25\,\mathrm{Hz}$ and a time sampling of $4\,\mathrm{ms}$ is injected at $\mathbf{x}_s = (750, 0)\mathrm{m}$. First, we corroborate the implementation of the projector spectral and the coupled Schulz scheme given by equations 3.6 and 3.8, respectively. For this, we select the velocity values of the layer at $z = 750\,\mathrm{m}$ (dashed black line in Figure 3.2a) and set the angular frequency to $\omega = 190\,\mathrm{rad/s}$. Next, the Helmholtz operator is constructed (Figure 3.2b), with dimension $nx \times nx$. In each line of the L operator, the 1D locations from the finite-difference stencils are mapped to the 1D index k using $k = 1, \ldots, nx$. Figures 3.3a-b show the results of the filtered Helmholtz operator and the square-root operator, respectively. Figure 3.4a demonstrates the Newton-Schulz method convergence trend. Lines with different colors are new eigenvalue spectra corresponding to the increasing number of iterations. As the number of iterations increases, the positive portion of the spectrum remains unaltered, while the non-positive portion converges entirely to zero. The values at the 151-st row of Figure 3.3a are extracted and compared to the result when the SVD algorithm is used to filter the negative eigenvalues. We observed that the values after applying the spectral projector fit perfectly with the results produced by the SVD method (see Figure 3.4b). Finally, to quantify the computing errors, we calculate the relative error between the filtered Helmholtz operator and the iterative square-root operator, defined as $(||L - k_z \times k_z||_2)/(||L||_2)$. From Figure 3.4c, we can see that 15-20 iterations converge to a stable value, maintaining a balance between efficiency and accuracy, which is consistent with the observations made by You et al. (2019). These results demonstrate that the selected algorithms can accurately attenuate the evanescent waves and compute the k_z operator, providing a robust foundation for the study of one-way propagators.

Figure 3.5 presents the results obtained from the post-stack depth migration methods applied to the impulse response test. As a reference, we have picked the wavefront from the wavefield simulation performed using the rapid expansion method (REM) (Pestana and Stoffa, 2010), indicated by the red dashed line. The conventional one-way propagators (Figures 3.5a-b) exhibit phase errors beyond a certain angle, with their phase curves increasingly bending inward as the angle grows. Figure 3.5c displays the impulse response calculated using a ninth-order TS expansion, comparable to the migrated section obtained through our proposed algorithm using a seventh-order JA approach (see Figure 3.5d). The impulse response results demonstrate that the one-way wave-equation migration method based on matrix multiplication performs exceptionally well in simulating propagating waves at large angles, maintaining an accurate phase curve even in the presence of significant lateral velocity variations. However, the one-way algorithm proposed herein outperforms the method employing the TS approach for computing the one-way extrapolator, as it requires fewer expansion terms to achieve precise results. This test, along with the subsequent examples, consistently showed that the TS and JA expansions required orders differing by two terms. Specifically, a ninth-order expansion was necessary for TS, whereas a seventh-order expansion sufficed for JA to achieve similar quality in the migrated sections. Consequently, the following analysis will exclusively compare the image quality produced by conventional migration methods with that of our proposed migration scheme.

Post-stack migration for the SEG/EAGE salt model

For the post-stack migration example, we employed the SEG/EAGE salt model (Aminzadeh et al., 1996), a classical benchmark for evaluating imaging quality. The primary obstacle presented by this model pertains to obtaining high-quality images of the structures situated beneath the salt dome. This difficulty is due to the significant velocity contrast introduced by the salt body, as well as the need to accurately image its steeply dipping boundaries. The model consists of 1290 × 300 grid nodes, with a grid spacing of 12.192 m. Considering the difficulty of obtaining an exact real velocity model, a smoothed version of the original velocity model is utilized to evaluate the performance of the migration algorithms. The velocity model and its smoothed counterpart used in this experiment are depicted in Figures 3.6a and 3.6b, respectively. The zero-offset section comprises 1290 traces, with a time interval of 8 ms and a record length of 5.0 s per trace (see Figure 3.6c).

The conventional PSPI, SS, and our proposed migration algorithm were applied to migrate the zero-offset data, with the resulting imaging sections displayed in Figure 3.7. Upon examining the overall images produced by these migration methods, it is evident that the structures beneath the salt body are clearly imaged by both the PSPI and our proposed algorithm, with the latter providing a better image, particularly in the steeply dipping boundaries on some flanks of the salt model (see red arrows in Figure 3.7c). In the case of the SS method, our approach provides a more continuous delineation of the plane located in the deeper region of the model, as indicated by the red arrow in Figure 3.7c. Moreover, for the images generated by the two conventional methods, we observed the presence of artifacts within the salt body, which are absent in the section migrated using our proposed method. The superior imaging quality of the proposed method is attributed to its ability to manage wave propagation at large angles with precision, as showcased by the impulse response test (Figure 3.5).

Pre-stack migration for the 2D Marmousi model

To further test whether our proposed method can migrate a complex model with multiple shot gathers, the benchmark Marmousi model is employed (Figure 3.8a). This model represents a complex area that involves multiple anticlines, three large-angle dipping faults, and the contact relationship between strata is sophisticated (Martin et al., 2006). The size of the Marmousi model is 9200 m × 2992 m, which is discretized on a 369 × 375 mesh, and the spatial sampling is 25 m in the x direction and 8 m in the z direction. For this numerical experiment, we constructed a fixed-spread geometry with 185 sources, with shot positions ranging from 0 m to 9200 m at 50 m intervals. Each shot has 184 receivers, starting from 25 m to 9175 m at 50 m intervals. We apply absorbing boundaries on all sides, i.e., we assume that surface-related multiples and ghost wave effects are removed from the recorded data set. The direct wave in the recorded data was removed by modeling it separately in a homogeneous medium (values of the first layer) and then subtracting it from the recorded data. The duration of each shot record is 2.9 s sampled at 4 ms. In this test, a Ricker wavelet with an upper cutoff frequency of 25 Hz was used as a source function. Using the exact velocity model as input and employing the REM, we conducted forward modeling to compute the seismic data set for the specified geometry. Figure 3.8b illustrates the migration velocity model, derived from applying a filter to the true velocity model.

Figures 3.9a-c show the migration sections of the PSPI, SS and our proposed pre-stack depth migration for this model, respectively. Overall, all three methods successfully imaged the main structures. However, the conventional methods produce a distorted image of a steeply-dipping fault when it intersects with different layers. On the other hand, although there are some artifacts in the lateral parts of the migrated section, the reflections imaged by our proposed migration method are relatively clearer and exhibit better continuity, as highlighted by the red arrows in Figure 3.9c. This observation highlights the advantage of our proposed migration method, namely its capacity to effectively manage waves at large angles.

Pre-stack migration on a field data set

As a final example, we apply the proposed one-way migration scheme to a 2D streamer data set provided by Equinor. This data, originally acquired in a deep-water environment in the Norwegian North Sea by SAGA Petroleum A.S., now part of Equinor (Brackenhoff et al., 2019), consists of P-wave recordings. For this field data set, as illustrated in Davydenko and Verschuur (2018), the following pre-processing steps were carried out: the source wavelet was removed, near offsets were recovered, free-surface multiples were eliminated, the direct wave was muted, and a $\sqrt{t}$ scaling was applied to approximate 2D geometric spreading. To create a split-spread geometry, we selected 200 shots and 199 receivers from the pre-processed data set, positioned on the surface at intervals such that there is a source at 0 m, a receiver at 25 m, a source at 50 m, a receiver at 75 m and so on. The data were recorded with a sampling interval of 4 ms for a total recording time of 5.588 s. Figure 3.10 shows the migration velocity model, which corresponds to a resampled version of the released model. It covers a depth of 5000 m and a length of 9950 m, with grid dimensions of 401 × 399 and grid intervals of 12.5 m and 25 m in the vertical and horizontal directions, respectively.

The imaging sections produced by the one-way migration methods are shown in Figure 3.11. The results demonstrate that our proposed migration algorithm produces more continuous events compared to the PSPI and SS methods, particularly for the image events highlighted by the red arrows and enclosed within the red rectangles in Figure 3.11c. Additionally, because our method accounts for lateral variations in the velocity model, it is reasonable to believe that the positioning of the reflectors using our method is more accurate than that obtained with conventional one-way methods. This enhanced clarity is advantageous for seismic interpretation of the target stratum. The improved imaging results can be attributed to the broader angle correction offered by our proposed method, despite the presence of some low amplitude artifacts.

Discussion

The initial design of one-way propagators was aimed at achieving an efficient migration process using specific approximation theories. In contrast, the objective of our proposed method is to accurately image complex models. Our approach does not rely on assumptions about lateral velocity variations, facilitating the recovery of steep reflectors and improving the continuity of certain layers, as demonstrated in our examples. The proposed one-way scheme allows for the complete construction of the depth propagator solely through matrix multiplication, a key feature that simplifies implementation. Each one-way method has its limitations and associated costs. Conventional one-way wave equation migration methods are highly efficient but struggle with complex models. Conversely, our proposed method excels at imaging intricate media and structures, although it is less computationally efficient. Therefore, research will need to focus on developing more efficient algorithms and implementations for our one-way migration in three-dimensional cases.

From a computational implementation perspective, computation performance can be significantly enhanced by leveraging techniques such as GPU acceleration (You et al., 2019) and linear algebra libraries optimized for these architectures. It is important to note that in the construction of the one-way propagator, only real matrices are required, which is evident for both L and its negative eigenvalue filtering. However, during the extrapolator construction step, only a component (real or imaginary) of the complex operator is updated at each iteration. Thus, the computation can be performed using only real matrices, with the complex operator being assembled only at the final stage. Based on our experience, this approach reduces the computation time for constructing the propagator described in equation 3.9 by half compared to the time required when using complex matrices.

On the other hand, to enhance the efficiency of the proposed one-way migration scheme, advanced mathematical tools, including the proposed JA expansion for computing the exponential operator, can be employed. Our numerical tests have shown that the JA expansion is particularly effective in calculating the exponential operator with high precision and using fewer terms compared to the TS approximation. Additionally, techniques such as the hierarchically semi-separable randomized (HSS) method (Miao et al., 2014) can be utilized to improve the computational performance of the spectral projector calculation. These performance optimizations remain open research topics and will be further explored in future studies.

Conclusion

Conventional one-way migration methods face challenges in maintaining stability during wavefield propagation and accurately imaging at large angles. These drawbacks are associated with the methodologies used in constructing the wavenumber operator and the approximations used to compute the exponential extrapolator. In this study, we employed the Newton-Schulz algorithm along with a stable iterative scheme to compute the square root of the Helmholtz operator, thereby excluding evanescent energy. By attenuating the non-positive spectrum components of the Helmholtz operator and accurately determining its square root within a gradient velocity model with significant variation, we demonstrated that the matrix multiplication method yields a correct matrix square root. This provides a robust foundation for the study of one-way propagators.

Furthermore, we introduced a novel migration scheme where the exponential operator is computed using the Jacobi-Anger expansion. The application of our proposed algorithm across various scenarios, including an application on a field data set, demonstrates that our one-way migration scheme maintains stability even within complex velocity models. The results indicate that the proposed method yields images with superior accuracy and quality compared to conventional one-way migration methods. Additionally, our scheme can simulate wavefields at larger angles using fewer terms than the Taylor series expansion approach, enhancing computational efficiency.

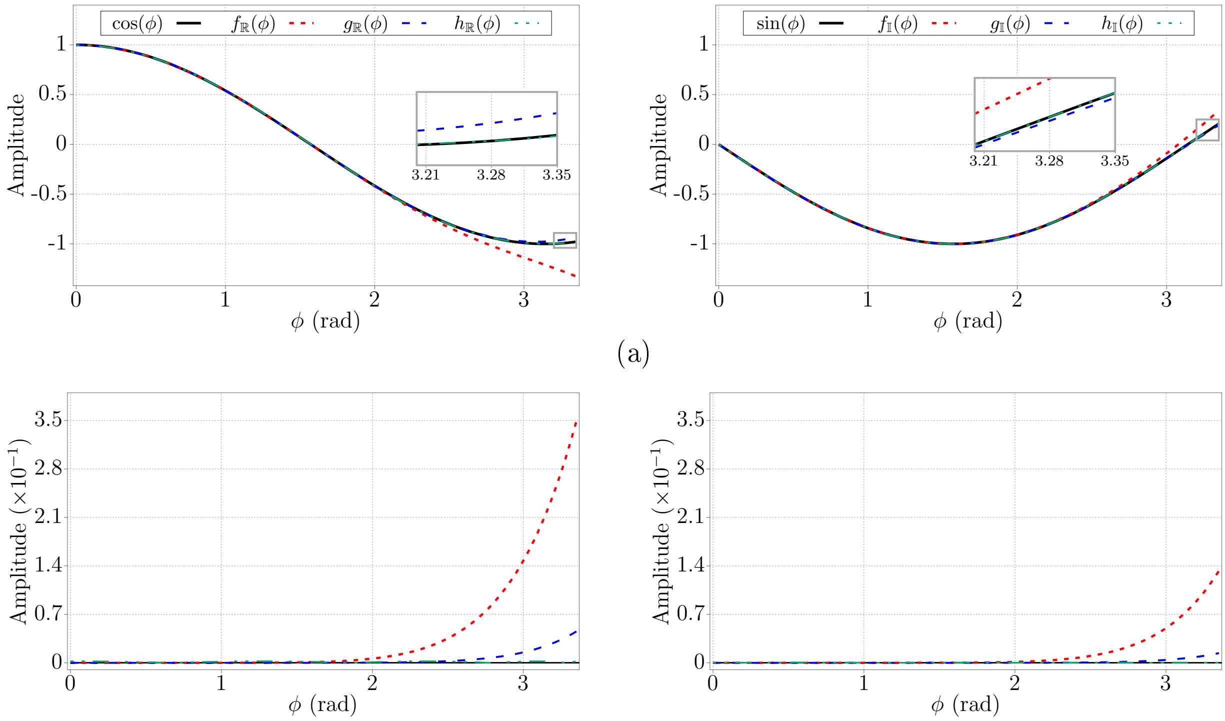

(a)

(b)

Figure 3.1: (a) Approximations for the one-way extrapolator using Taylor series (TS) and Jacobi-Anger (JA) expansion, where $\phi\,(\equiv k_z \Delta z)$ corresponds to the phase. The functions $f(\phi)$ and $g(\phi)$ correspond to the approximation using the seventh-order and ninth-order TS expansion, respectively, while $h(\phi)$ represents the extrapolator calculated using the seventh-order JA expansion. The black line is the exact value. The subscripts $\mathbb{R}$ and $\mathbb{I}$ denote the real and imaginary parts of the approximations, respectively. (b) The absolute error between each approximation and the exact value. Note that the color convention for each approximation is consistent across both panels.

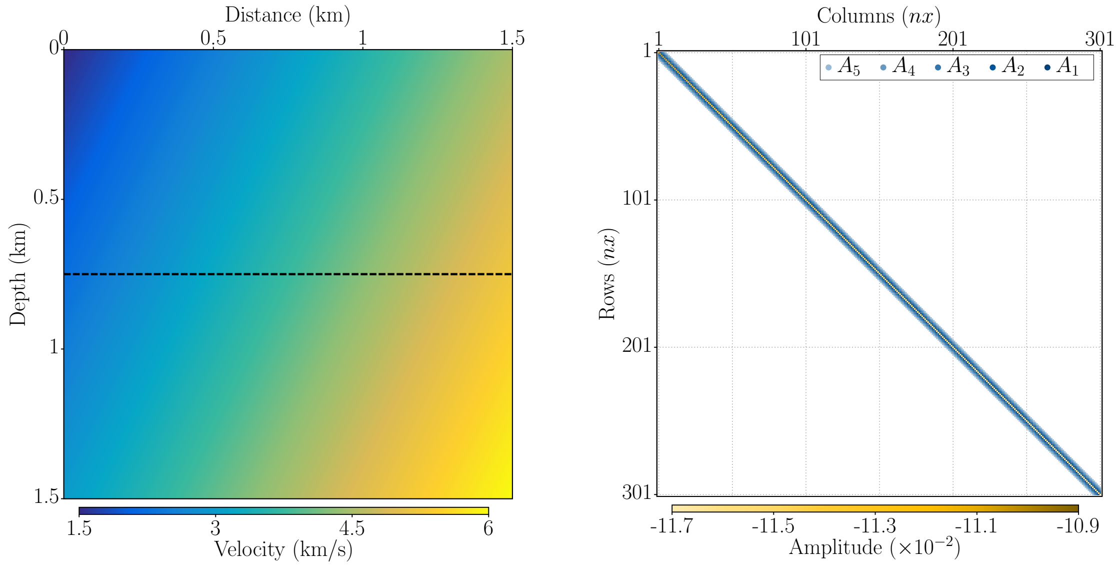

(a) (b)

Figure 3.2: (a) The gradient velocity model and (b) the sparse matrix for the Helmholtz operator L, where $A_1 = 6.67 \times 10^{-2}$, $A_2 = -9.52 \times 10^{-3}$, $A_3 = 1.59 \times 10^{-3}$, $A_4 = -1.98 \times 10^{-4}$ and $A_5 = 1.27 \times 10^{-5}$. A tenth-order finite-difference scheme was used to approximate the spatial derivative along the horizontal axis. The dashed black line represents the layer at $z = 750\,\mathrm{m}$, which was selected to validate the algorithms for filtering out the negative eigenvalues and computing the square-root operator (see Figure 3.3).

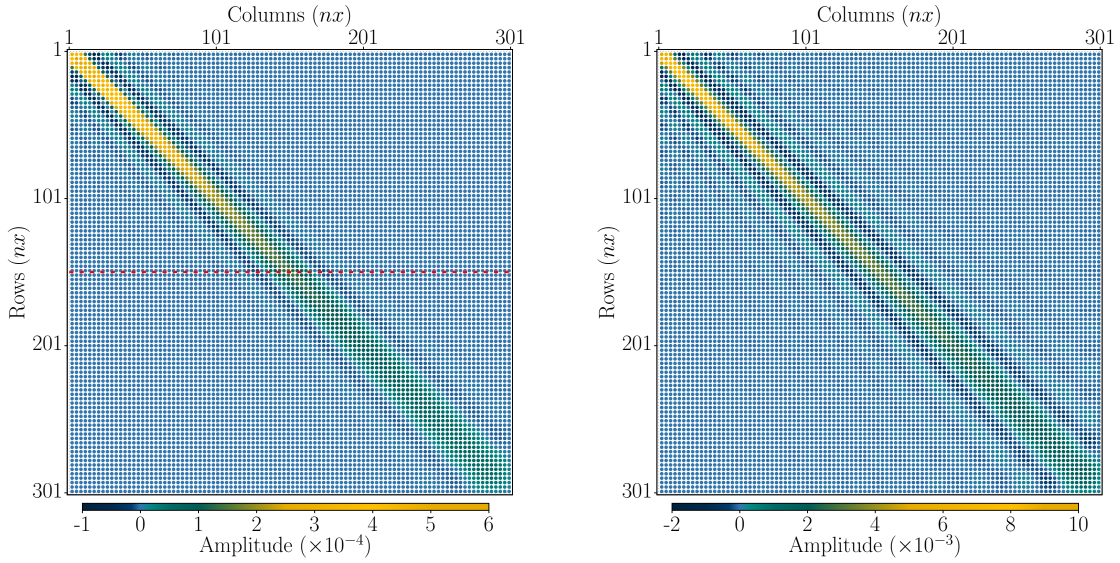

(a) (b)

Figure 3.3: Matrix structure of (a) the filtered Helmholtz operator $\bar{L}$ using the spectral projector scheme with 30 iterations, and (b) the square-root operator k_z computed using the coupled Schulz iteration scheme with 20 iterations. For visualization purposes, the matrices are displayed at a lower resolution than the originals, with each row and column resampled to 101 elements.

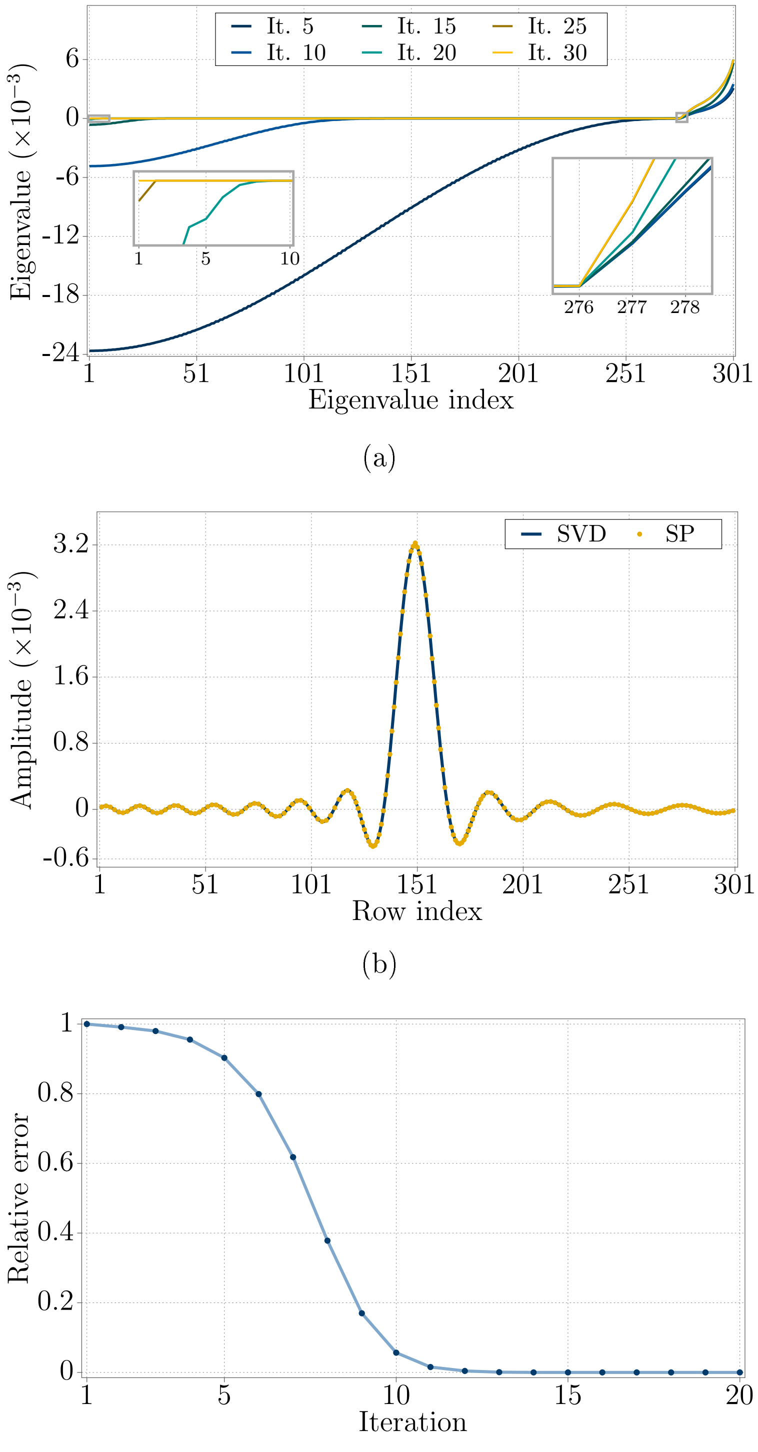

(a)

(b)

(c)

Figure 3.4: (a) Convergence trend for the Newton-Schulz method. As the number of iterations grows, the positive part of the spectrum remains untouched, while the non-positive part converges to zero. (b) Comparison between the values in the middle column of Figure 3.3a, i.e., L after being filtered by the spectral projector (SP), and the corresponding values obtained using SVD to filter the negative spectrum. (c) Relative errors as a function of the number of iterations for the coupled Schulz iteration scheme.

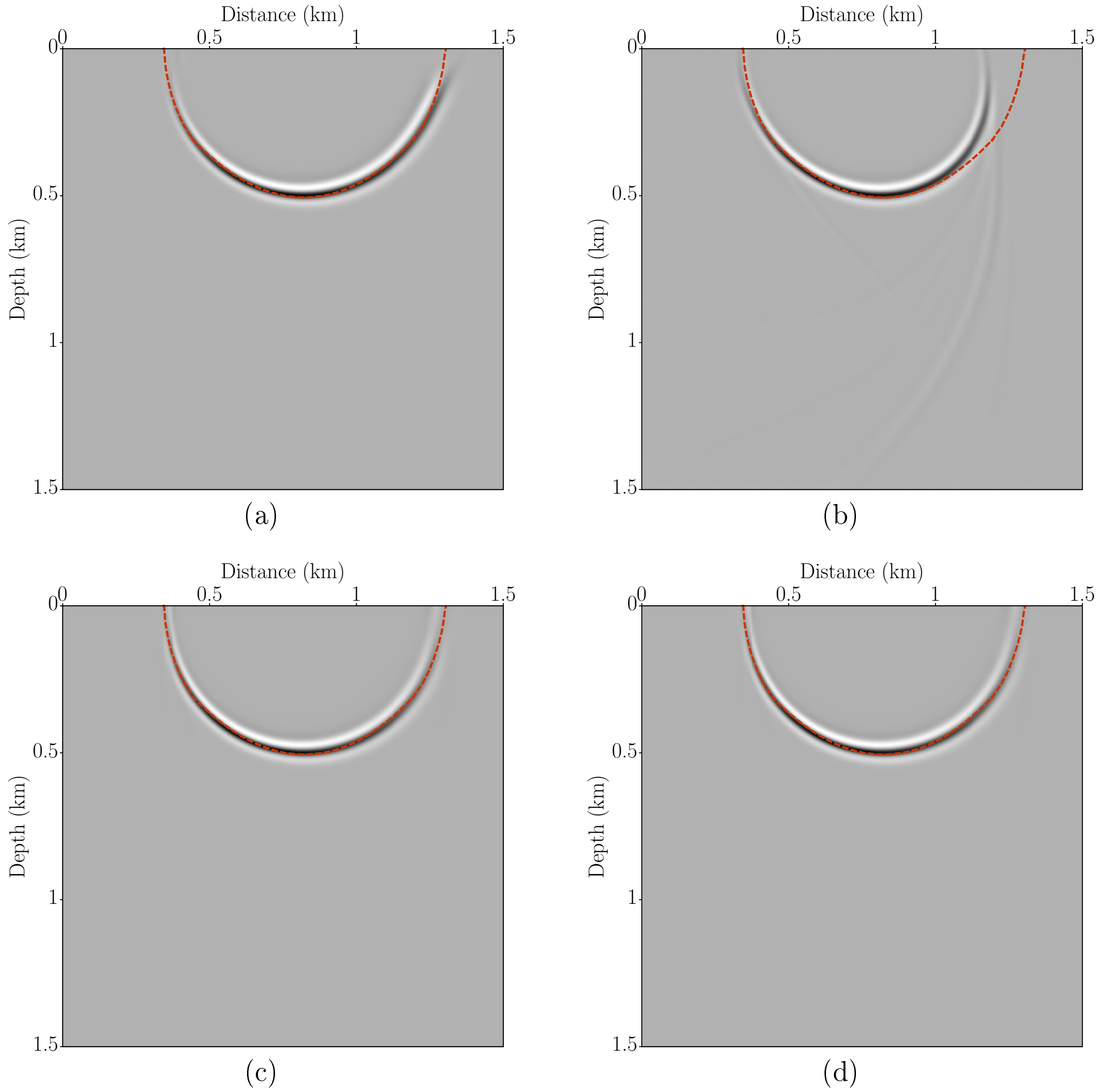

(a) (b)

(c) (d)

Figure 3.5: The response is generated by the conventional one-way (a) PSPI and (b) SS methods. (c) Impulse response using a one-way propagator based on matrix multiplication with (c) a ninth-order TS approximation and (d) a seventh-order JA expansion for our proposed algorithm. The dotted red line represents the reference response curve.

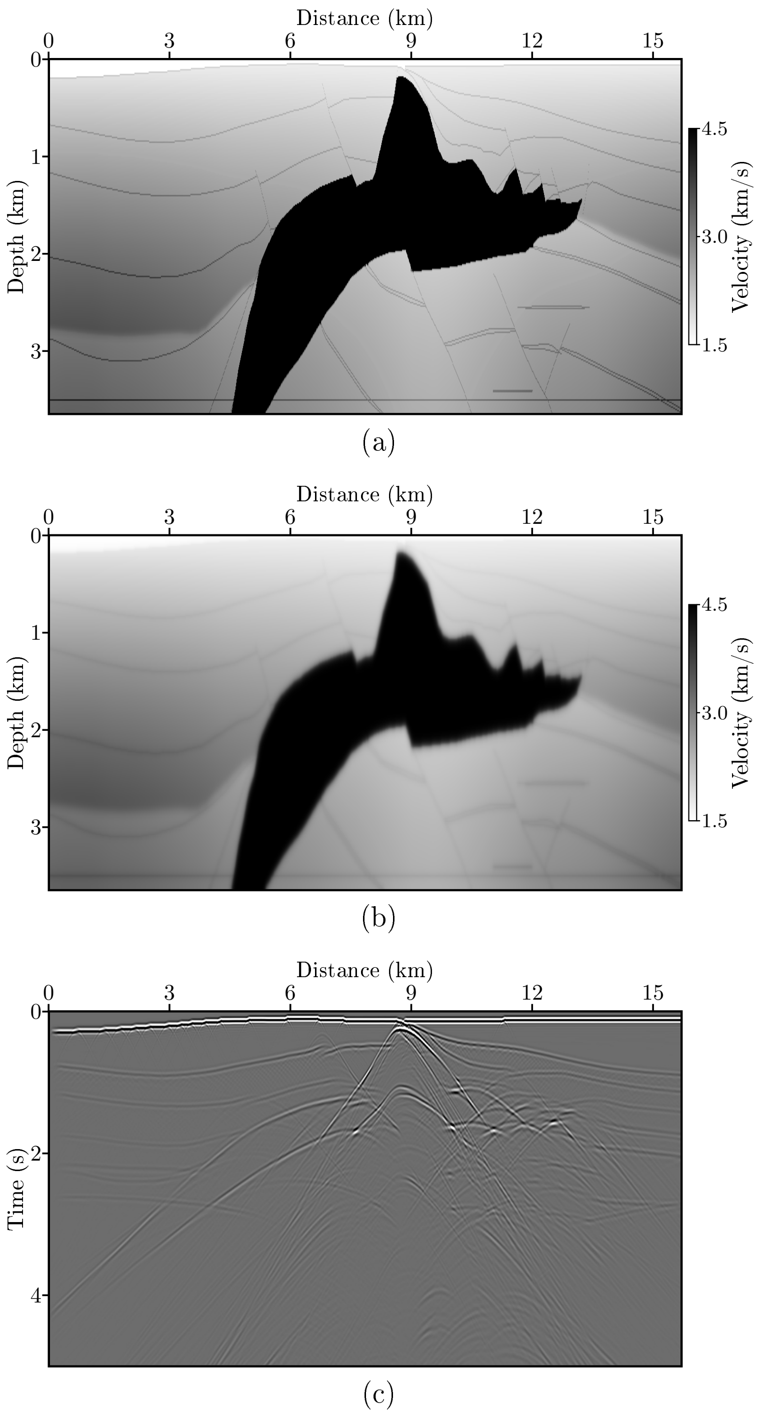

Figure 3.6: (a) The SEG/EAGE velocity model and its corresponding (b) migration velocity model. (c) The zero-offset section is used as input for the one-way migration methods.

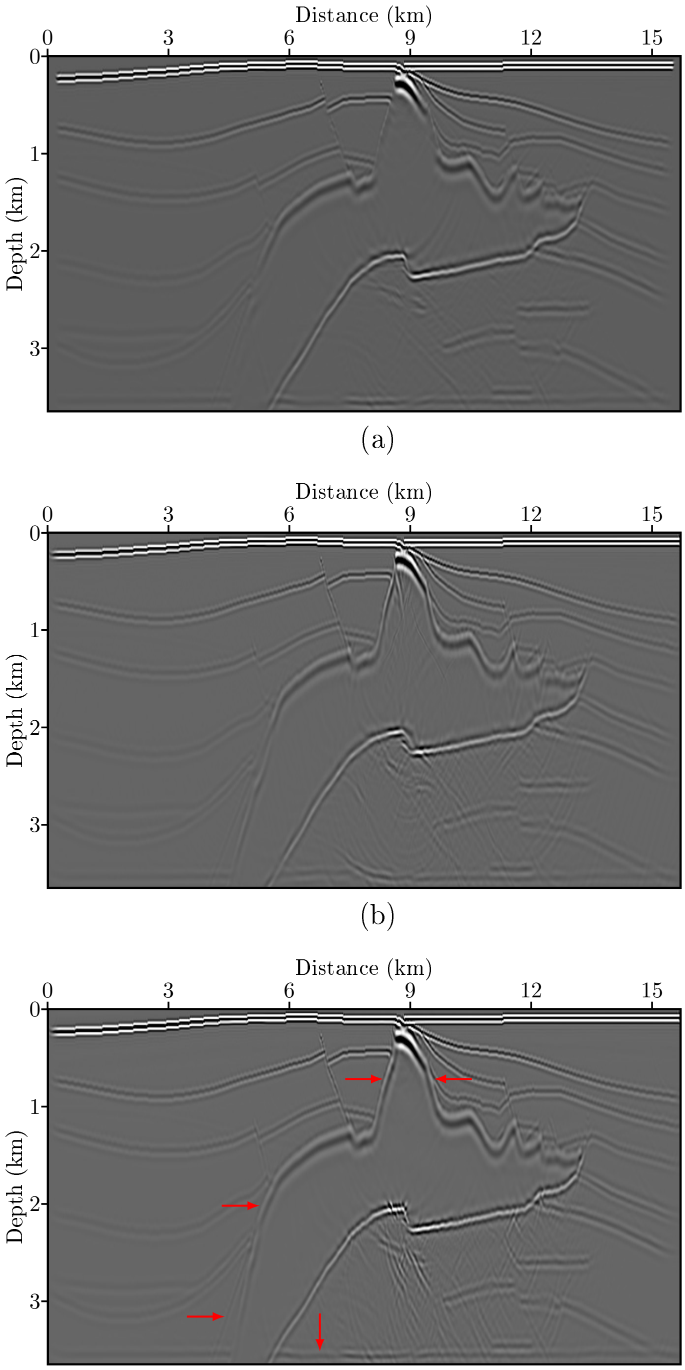

(a)

(b)

(c)

Figure 3.7: Post-stack migration sections for the SEG/EAGE salt model generated using the conventional one-way (a) PSPI, (b) SS, and (c) our proposed algorithm.

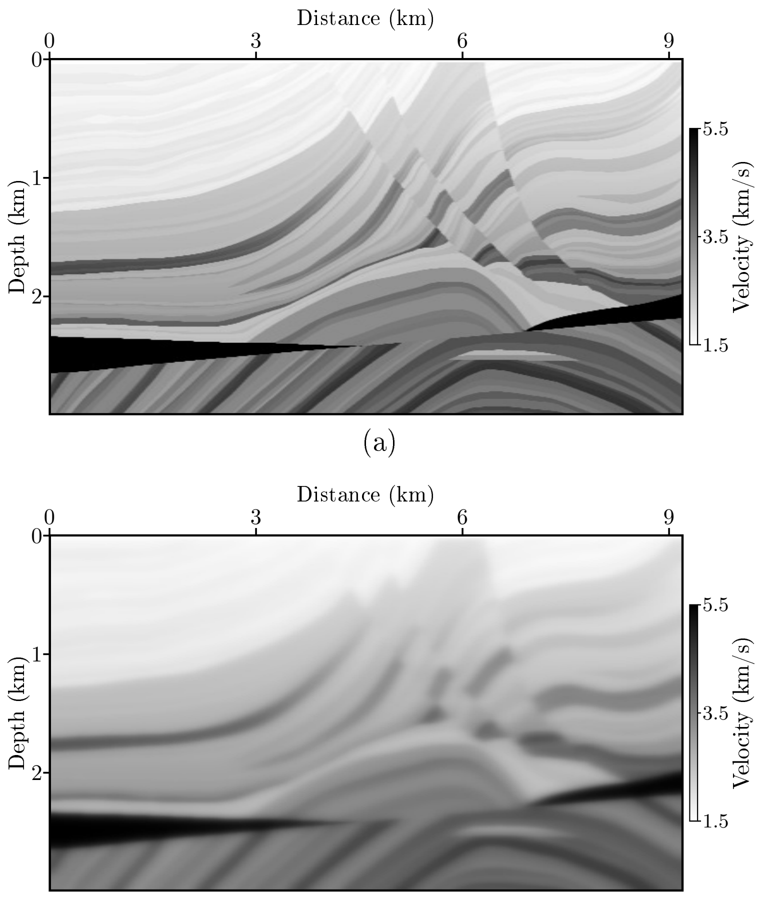

(a)

(b)

Figure 3.8: (a) The Marmousi velocity model and its corresponding (b) migration velocity model.

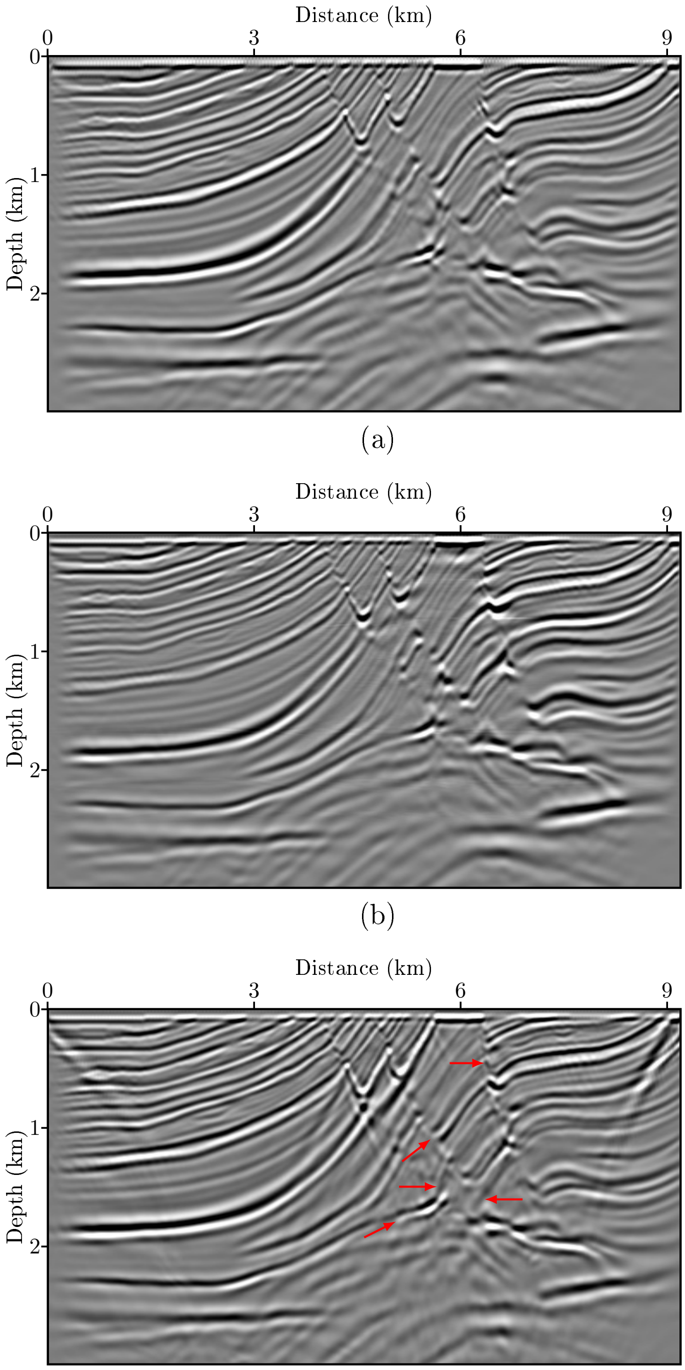

Figure 3.9: Migration sections for the Marmousi model generated using different one-way methods: (a) PSPI, (b) SS, and (c) our proposed algorithm.

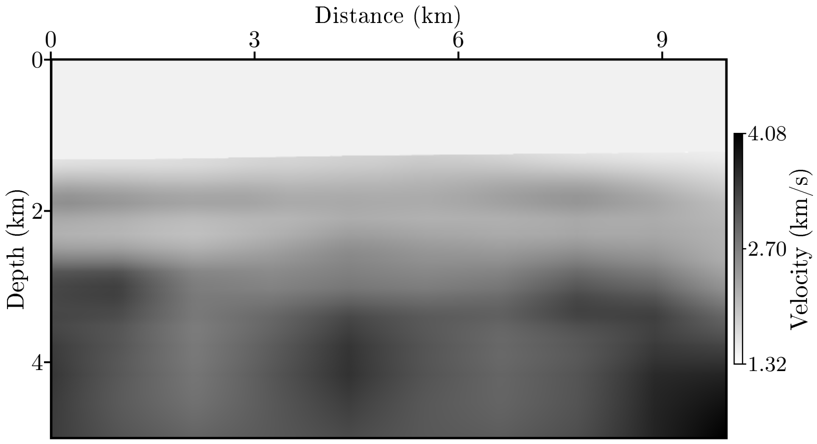

Figure 3.10: The velocity model provided by Equinor for migration.

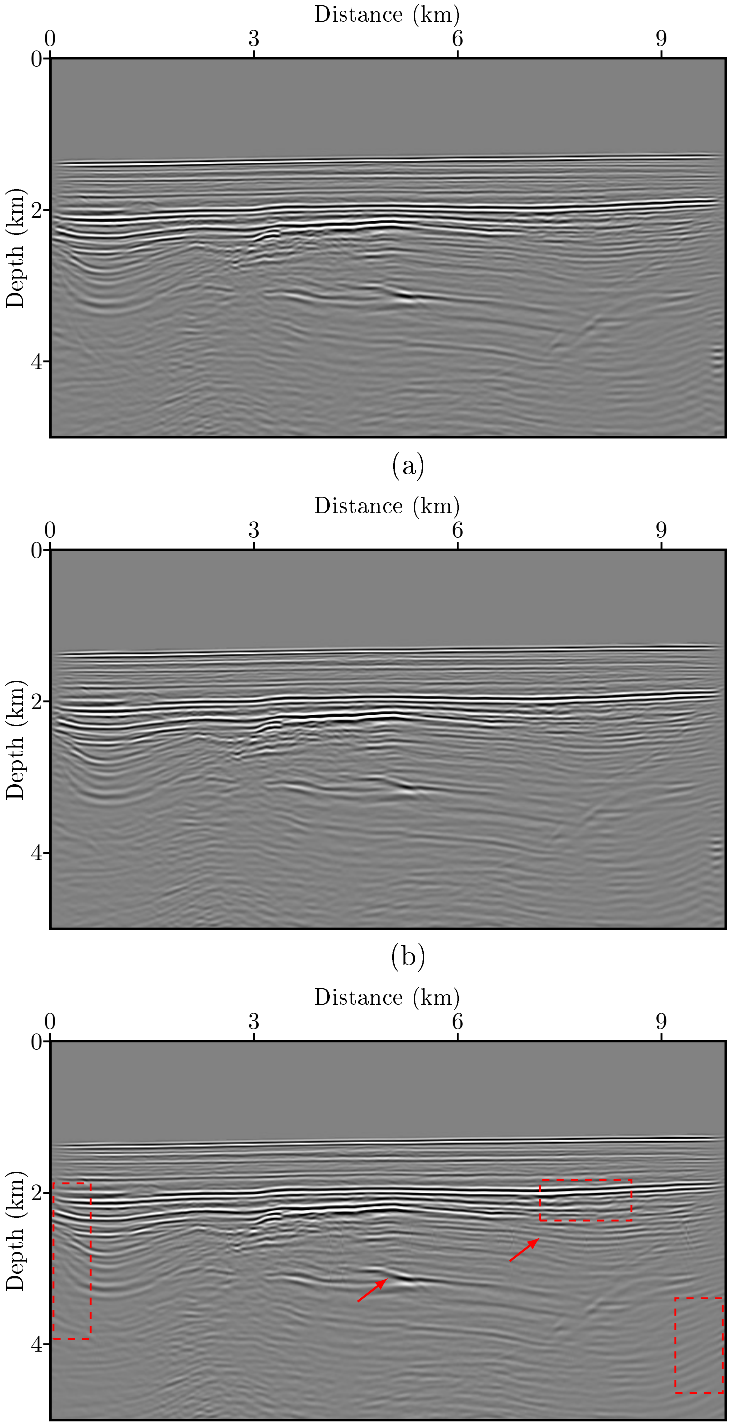

(a)

(b)

(c)

Figure 3.11: Migration sections for the real seismic data using different one-way methods: (a) PSPI, (b) SS, and (c) our proposed algorithm.

References

Abramowitz, M. and Stegun, I. A. (1972) Handbook of Mathematical Functions with Formulas, Graphs, and Mathematical Tables, National Bureau of Standards.

Aminzadeh, F.; Burkhard, N.; Long, J.; Kunz, T. and Duclos, P. (1996) Three dimensional SEG/EAEG models - An update, The Leading Edge, **15**:131–134.

Auslander, L. and Tsao, A. (1992) On parallelizable eigensolvers, Advances in Applied Mathematics, **13**:253–261.

Baysal, E.; Kosloff, D. D. and Sherwood, J. W. C. (1983) Reverse time migration, Geophysics, **48**(11):1514–1524.

Bowman, F. (1958) Introduction to Bessel Functions, Dover Publications.

Brackenhoff, J.; Thorbecke, J. and Wapenaar, K. (2019) Monitoring of induced distributed double-couple sources using Marchenko-based virtual receivers, Solid Earth, **10**(4):1301–1319.

Cerjan, C.; Kosloff, D.; Kosloff, R. and Reshef, M. (1985) A nonreflecting boundary condition for discrete acoustic and elastic wave equations, Geophysics, **50**(4):705–708.

Claerbout, J. F. (1971) Toward a unified theory of reflector mapping, Geophysics, **36**(3):467–481.

Claerbout, J. F. (1985) Imaging the earth's interior, Blackwell Scientific Publications, Ltd.

Davydenko, M. and Verschuur, D. J. (2018) Including and using internal multiples in closed-loop imaging - Field data examples, GEOPHYSICS, **83**(4):R297–R305.

Gazdag, J. (1978) Wave equation migration with phase-shift method, Geophysics, **43**:1342–1351.

Gazdag, J. and Sguazzero, P. (1984) Migration of seismic data by phase shift plus interpolation, Geophysics, **49**:124–131.

Grimbergen, J. L. T.; Dessing, F. J. and Wapenaar, K. (1998) Modal expansion of one-way operators in laterally varying media, Geophysics, **63**:995–1005.

Higham, N. J. (1987) Computing real square roots of a real matrix, Linear Algebra Appl., **88/89**:405–430.

Higham, N. J. (2008) Functions of Matrices, Society for Industrial and Applied Mathematics.

Kenney, C. S. and Laub, A. J. (1995) The matrix sign function, IEEE Transactions on Automatic Control, **40**:1330–1348.

Kosloff, D. D. and Baysal, E. (1983) Migration with the full acoustic wave equation, Geophysics, **48**(6):677–687.

Levin, S. A. (1984) Principle of reverse-time migration, Geophysics, **49**(5):581–583.

Li, A.; Verschuur, D. J.; Liu, X. and Abolhassani, S. (2024) An Accurate Propagator for Heterogeneous Media in Full Wavefield Migration, IEEE Transactions on Geoscience and Remote Sensing, **62**:1–10.

Martin, G. S.; Wiley, R. and Marfurt, K. J. (2006) Marmousi2: an elastic upgrade for marmousi, Lead. Edge, **25**:156–166.

McMechan, G. A. (1983) Migration by extrapolation of time-dependent boundary values, Geophysics Prospecting, **31**(3):413–420.

Miao, L.; Zheglova, P. and Herrmann, F. J. (2014) Randomized HSS acceleration for full-wave-equation depth stepping migration, in: *SEG Technical Program Expanded Abstracts 2014*, pp. 3752–3756.

Mulder, W. A. and Plessix, R. E. (2004) A comparison between one-way and two-way wave-equation migration, Geophysics, **69**:1491–1504.

Pestana, R. C. and Stoffa, P. L. (2010) Time evolution of wave equation using rapid expansion method, Geophysics, **75**:T121–T131.

Ristow, D. and Rühl, T. (1994) Fourier finite-difference migration, Geophysics, **59**(12):1882–1893.

Sandberg, K. and Beylkin, G. (2009) Full-wave-equation depth extrapolation for migration, Geophysics, **74**(6):WCA121–WCA128.

Stockwell, J. W. (1999) The CWP/SU: Seismic Unix package, Computers & Geosciences, **25**(4):415–419.

Stoffa, P.; Fokkema, J.; de Luna Freire, R. and Kessinger, W. (1990) Split-step fourier migration, Geophysics, **55**:410–421.

Thorbecke, J. W.; Wapenaar, K. and Swinnen, G. (2004) Design of one-way wavefield extrapolation operators, using smooth functions in WLSQ optimization, Geophysics, **69**(4):1037–1045.

Wapenaar, C. P. A. (1990) Representation of seismic sources in the one-way wave equations, Geophysics, **55**(6):786–790.

Wapenaar, K. and Grimbergen, J. L. T. (1998) A discussion on stability analysis of wave field depth extrapolation, 68th Annual International Meeting, SEG, Expanded Abstracts, pp. 1716–1719.

Watson, G. N. (1944) A Treatise on the Theory of Bessel Functions, Cambridge University Press.

Whitmore, N. D. (1983) Iterative depth migration by backward time propagation, in: *SEG Technical Program Expanded Abstracts 1983*, pp. 382–385.

You, J.; Wu, R.-S. and Liu, X. (2018) One-way true-amplitude migration using matrix decomposition, Geophysics, **83**(5):S387–S398.

You, J.; Liu, Z.; Liu, J. and Li, C. (2019) One-way propagators based on matrix multiplication in arbitrarily lateral varying media with GPU implementation, Computers and Geosciences, **130**:32–42.

4

Conclusões

A RTM é capaz de imagear refletores com mergulhos acentuados e modelos de velocidade complexos. No entanto, isso também faz com que a condição de imagem convencional baseada na correlação cruzada produza ruídos de baixa frequência e alta amplitude que contaminam a imagem migrada. A decomposição dos campos de ondas extrapolados e a aplicação da condição de imagem causal removem com sucesso esses artefatos das imagens. Esse tipo de condição de imagem requer um algoritmo de separação do campo de ondas nas suas componentes ascendente e descendente, que pode ser alcançado usando a extrapolação do campo de ondas analítica, é muito mais econômico do que métodos de separação via transformadas de Fourier no tempo, uma vez que estes últimos requerem o armazenamento do campo de ondas em todos os passos de tempo. No capítulo 1 desta tese apresentamos uma abordagem eficiente de modelagem direta para calcular o campo de ondas analítico com base no método de expansão rápida de maneira estável e sem a presença de dispersão numérica. No método proposto, o campo de ondas da fonte é extrapolado no tempo e, para cada passo de tempo, podemos calcular a derivada temporal de primeira ordem e, em seguida, a transformada de Hilbert do campo de ondas. Com base no campo de ondas analítico, geramos os componentes ascendentes e descendentes em simulações acústicas 2D e 3D. Testamos o esquema proposto em modelos com diferentes complexidades e demonstramos que podemos calcular o campo de ondas analítico usando apenas uma única propagação, com a mesma qualidade do procedimento comum que requer duas propagações. Esses testes numéricos também mostram que o método é eficiente, evitando o requisito de armazenamento do campo de pressão, e aumentando o custo da modelagem direta em apenas 20.2 %. Usando nosso método para calcular o campo de ondas analítico e separar explicitamente o campo de ondas em suas componentes unidirecionais, foi possível empregar a condição de imagem causal na RTM a um custo computacional apenas um pouco superior ao da condição de imagem convencional por correlação cruzada. Aplicamos a condição de imagem causal em diferentes modelos de velocidade e verificamos que o imageamento RTM com a condição de imagem causal pode remover efetivamente o ruído de baixa frequência indesejado produzido pela condição de imagem convencional. O esquema numérico proposto para a decomposição do campo de ondas melhora significativamente a eficiência da aplicação da condição de imagem causal e aumenta o custo computacional em aproximadamente 27 % quando comparado com a RTM usando a correlação cruzada como princípio de imageamento.

No segundo capítulo desta tese, propomos um esquema eficiente para implementar a técnica FLSRTM utilizando funções de Green de baixo posto. Enquanto o FLSRTM com funções de Green armazenadas integralmente enfrenta limitações de memória para conjuntos de dados ou modelos em larga escala, nossa abordagem reduz esse desafio. Especificamente, decompomos a função de Green associada à frequência dominante da fonte sísmica em matrizes retangulares e unitárias utilizando algoritmos SVD convencionais e estocásticos. O posto ótimo, determinado por um critério baseado na distribuição acumulada de valores singulares normalizados, garante um armazenamento eficiente de memória. Além disso, expandimos nossa investigação incorporando algoritmos SVD aleatório e comprimido. Esses avanços reduzem significativamente o tempo computacional para a construção de funções de Green de baixo posto. Ao utilizar os algoritmos rSVD e cSVD, conseguimos reduções substanciais nos requisitos de memória sem comprometer a eficiência computacional. Nossos experimentos numéricos, realizados em um modelo estratificado e em um modelo modificado Marmousi-2, demonstram que as funções de Green reconstruídas exibem alta precisão usando matrizes de posto reduzido. Estudos comparativos com FLSRTM utilizando funções de Green armazenadas integralmente validam a precisão do nosso esquema FLSRTM proposto. Notavelmente, o método cSVD apresentou consistentemente um desempenho superior em termos de eficiência computacional, tornando-se a escolha preferencial para a execução do esquema FLSRTM. Em geral, o esquema FLSRTM com funções de Green de baixo posto via rSVD e cSVD representa uma abordagem computacionalmente eficiente para gerar imagens de migração precisas.

No último capítulo desta tese, abordamos os desafios enfrentados pelos métodos convencionais de migração WEM em manter a estabilidade durante a propagação do campo de ondas e em realizar um imageamento preciso em meios com fortes contrastes de velocidade e refletores com mergulhos acentuados. Esses problemas estão associados às metodologias usadas na construção do operador de número de onda e às aproximações empregadas para calcular o extrapolador exponencial. No esquema de migração WEM proposto, utilizamos o algoritmo Newton-Schulz juntamente com um esquema iterativo estável para calcular a raiz quadrada do operador de Helmholtz, excluindo, assim, a energia evanescente. Ao atenuar os componentes do espectro negativo do operador de Helmholtz e determinar com precisão sua raiz quadrada em um modelo de velocidade em gradiente com variações significativas, demonstramos que os métodos selecionados computam de forma correta a raiz quadrada do operado de Helmholtz filtrado, o qual fornece uma base robusta para o estudo dos propagadores unidirecionais. Além disso, introduzimos uma nova aproximação para o operador exponencial, a qual esta baseada na expansão de Jacobi-Anger. A aplicação do nosso algoritmo proposto em diversos cenários, incluindo um conjunto de dados de campo, demonstra que nosso esquema de migração WEM mantém a estabilidade mesmo em modelos de velocidade complexos. Os resultados indicam que o método proposto gera imagens com precisão e qualidade superiores em comparação com métodos convencionais de migração WEM. Adicionalmente, nosso esquema pode simular campos de ondas utilizando menos termos do que a abordagem da expansão em série de Taylor, aprimorando a eficiência computacional.

Por fim, sugerimos as seguintes extensões a este trabalho: aplicar a construção eficiente do campo de ondas analítico a equações de ondas mais complexas; estender a abordagem FLSRTM proposta para o caso 3D, onde a redução de memória e tempo de cômputo pode ser ainda mais pronunciada; implementar esquemas de inversão mais robustos para permitir uma convergência mais rápida da função objetivo definida no esquema FLSRTM; e explorar o uso de diferentes arquiteturas computacionais, como GPU e FPGA, para acelerar a aplicação dos algoritmos empregados no esquema de migração WEM proposto.

Agradecimentos

Agradeço imensamente à UFBA, universidade da qual tenho um imenso orgulho, e ao SENAI CIMATEC, instituição em que trabalho e onde posso me realizar como geofísico. Ambas me forneceram grandes oportunidades de aprendizado.

Ao meu orientador, Dr. Reynam Pestana, pelo acompanhamento durante todo o desenvolvimento do meu curso de Doutorado, pelos ensinamentos, incentivo e confiança.

Aos membros da banca examinadora, pelas perguntas, sugestões e correções.

Aos meus pais, Gladys Apraez e David Revelo, pela sabedoria, força e apoio. Sem eles, nada disso seria possível. Agradeço também aos meus irmãos que me incentivaram, Ana, Cesar e Ivan, muito obrigado por tudo.

A Ashlee e Martin, que são o meu orgulho e a razão do amor que carrego no coração.

A Camila, pelo amor diário, incentivo, suporte e companheirismo.

A todos os familiares e amigos, especialmente aqueles que acompanham minha caminhada de perto.

Aos colegas da UFBA e CIMATEC pelo companheirismo, em especial: Leonardo, Cristian, Quezia, Laila, Fernanda, Jairo, Rodrigo, Peterson, Diego, Oscar e Victor.

Ao povo brasileiro, por sua música e simpatia.

E finalmente, a todos que diretamente ou indiretamente me incentivaram e ajudaram á cumprir este trabalho.